地理科学学院博士研究生美丽2024年博士学位论文答辩及科研成果公示

2024年5月地理科学学院理学专业博士研究生美丽完成博士学位论文答辩，答辩委员会一致同意该研究生通过博士学位论文答辩，建议授予理学博士学位。该生在读期间发表论文及佐证材料公示如下：

学号	姓名	专业	论文名称	刊物名称	发表情况	期刊类别	发表时间	是否达到学术论文发表要求
20196019003	美丽	地理学	Elevation-dependent response of spring phenology to climate and its legacy effect on vegetation growth in the mountains of northwest Mongolia	Ecological Indicators	见刊	SCI	2021	是
20196019003	美丽	地理学	Variation characteristics of ecosystem water use efficiency and its response to human activity and climate change in Inner Mongolia	Remote Sensing	见刊	SCI	2022	是
20196019003	美丽	地理学	Spatiotemporal variations of water use efficiency and its driving factors in Inner Mongolia from 2001 to 2020	Journal of Geographical Sciences	见刊	SCI	2023	是

地理科学学院

2024年5月31日

Ecological Indicators 126 (2021) 107640

Contents lists available at ScienceDirect

Ecological Indicators

journal homepage: www.elsevier.com/locate/ecolind

Elevation-dependent response of spring phenology to climate and its legacy effect on vegetation growth in the mountains of northwest Mongolia

Li Mei [a], Gang Bao [a,c], Siqin Tong [a,b,c,*], Shan Yin [a,c], Yuhai Bao [a,c], Kang Jiang [d], Yu Hong [e], Alateng Tuya [a], XiaoJun Huang [a]

[a] College of Geographical Science, Inner Mongolia Normal University, Hohhot 010022, China
[b] Inner Mongolia Key Laboratory of Disaster and Ecological Security on the Mongolian Plateau, Inner Mongolia Normal University, Hohhot 010022, China
[c] Inner Mongolia Key Laboratory of Remote Sensing and Geographic Information Systems, Inner Mongolia Normal University, Hohhot 010022, China
[d] College of Resources and Environmental Sciences, China Agricultural University, Beijing 100193, China
[e] College of Life Science and Technology, Inner Mongolia Normal University, Hohhot 010022, China

ARTICLE INFO

Keywords:
Elevation dependence
Spring phenology
Climate change
Legacy effects
Vegetation growth
Mountains of northwest Mongolia

ABSTRACT

Vegetation spring phenology in mountains has undergone profound changes due to climate change. In this paper, which made use of the Harmonic Analysis of Time Series (HANTS) smoothing algorithm and logistic models, the start of the vegetation growing season (SOS) inferred from MODIS datasets with different spatial resolutions from 2001 to 2018 was extracted. The MODIS data closest to the ground-truth observation data were then selected to reflect spring phenology. Combined with temperature and precipitation data, the spatio-temporal patterns and elevation-dependent change mechanisms of the SOS and its legacy effect on vegetation growth in the mountains of northwest Mongolia was examined and the following results were obtained: (1) Compared with the MOD13A1 and MOD13A2 datasets, the high spatial resolution MOD13Q1 dataset provided stronger correlations and the lowest errors with ground-truth observation data. (2) In this study, the SOS usually occurred between 120 and 152 day-of-year (DOY) with the earlier SOS detected in the low-elevation areas. Later SOS occurred mostly in the higher elevation areas. (3) The spatio-temporal variations in the SOS are mainly influenced by both spring temperature and winter precipitation, with increasing precipitation in winter tending to delay the SOS, while increasing spring temperature tended to advance the SOS. (4) At elevation gradient, the spring temperature showed a significant negative effect on SOS at all elevations, except between 1037 m and 1137 m and 3337 m to 3437 m above sea level (ASL), with a significant positive correlation between SOS and winter precipitation between 1337 m and 2937 m ASL. It is expected that spring temperature is closely linked to the heat accumulation of plants, while winter precipitation indirectly affects the temperature in spring. (5) In lower elevation areas (below 1437 m ASL), the SOS was found to be negatively correlated with spring and summer growth, with advancing SOS leading to increased vegetation growth during spring and summer. In higher elevation areas (above 1437 m ASL), the SOS was significantly negatively correlated with spring growth and positively correlated with summer growth. Hence, delayed SOS leads to decreased spring growth and increased summer growth. Also, we found the effect of SOS on vegetation growth gradually weakened from spring to summer. These findings can help to determine the mechanisms and functional consequences of spring phenological changes in mountain regions.

1. Introduction

Vegetation phenology is the annual timing of seasonal growth phases in vegetation (He et al., 2015; Wang et al., 2017a). Over the past half-century (IPCC, 2013), climate change has significantly altered vegetation phenology (Jin et al., 2012; Wang et al., 2017b), directly affecting carbon exchange, the dynamic balance of nutrients, biodiversity patterns, as well as the accompanying feedback to the climate system (Wang et al., 2017a). Since phenological processes are highly sensitive to climate change, monitoring them is an important requirement for studying the impact of climate change on terrestrial ecosystems (Chen et al., 2018). In particular, the start of the vegetation growing season

* Corresponding author at: College of Geographical Science, Inner Mongolia Normal University, Hohhot 010022, China.
E-mail address: tongsq223@imnu.edu.cn (S. Tong).

https://doi.org/10.1016/j.ecolind.2021.107640
Received 14 August 2020; Received in revised form 3 March 2021; Accepted 18 March 2021
Available online 2 April 2021

(SOS) is considered to be one of the most simple and effective indicators of climate change, because of its strong impacts on terrestrial ecosystem balances, and it's an independent measure of ecosystems responses to climate variability (Richardson et al., 2009; Piao et al., 2011a; Cong et al., 2013; Shen et al., 2015; Peng et al., 2017; Yun et al., 2018; Wang et al., 2020).

Mountains are considered prime indicators of global change (Deng et al., 2018). On the one hand, higher elevations are ideal regions to study responses to global climate change because they reflect drastic changes in many environmental factors (temperature, humidity, light, etc.) (Yang et al., 2018). On the other hand, global climate change is rapidly and significantly changing habitats in higher-elevation areas, which will inevitably lead to the migration of species and the movement of vegetation boundaries (Parmesan, 2006). Mountain ecosystems as sensitive regions of biological responses to climate change can reveal the dynamics of vegetation growth processes and reflect the response and adaptation of mountain ecosystems to global change (Deng et al., 2018; Zhu et al., 2019a).

The mountain areas of northwest Mongolia are one of the highest regions in the country and are famous for their large physical elevation gradient and fragile ecosystems. Elevation, aspect, and slope are the three main topographic factors that indirectly affect the patterns of vegetation in mountainous areas (Huang, 2002). Among these three factors, elevation is important because it serves as a proxy for precipitation and temperature (Jin et al., 2009). In most high-latitude and high-altitude ecosystems, temperature has been regarded as a driving factor for SOS change (Piao et al., 2011a). For example, Zhu et al. (2019a) reported that the delay of SOS in the Funiu Mountains, China, was mainly attributed to decreased temperatures in March. However, numerous studies have also shown that precipitation strongly affects spring phenology (Cong et al., 2013; Shen et al., 2015). Also, Du et al. (2020) identified a strong dependence of spring phenology on minimum temperature and precipitation in the arid-mountain ecosystems of China.

Previous studies have reported increased vegetation growth associated with advancing SOS (Keenan et al., 2014; Zhu et al., 2019a). However, an earlier SOS may also increase drought stress, thus reducing vegetation growth (Borchert et al., 2002; Ma et al., 2015). Recently, Zhou et al. (2020) reported increased vegetation growth in temperate China correlated with advancing spring phenology. During the period from 1982 to 2015, the spring phenology changed by -1.16 ± 0.25 days per decade, and spring and summer vegetation growth significantly increased by 2.6×10^{-3} and 4.8×10^{-3}, confirming how spring phenology plays a key role in vegetation growth. Nevertheless, to our knowledge, the elevation-dependent legacy effects of spring phenology on vegetation growth remain unclear. Furthermore, the underlying mechanisms of spring phenology responses to climate change in the mountains of northwest Mongolia are still not understood.

Therefore, in this study, we utilized logistic models to extract the SOS from Moderate Resolution Imaging Spectrometer (MODIS) datasets with different spatial resolutions from the period 2001 to 2018. The MODIS dataset that was found to be closest to the ground-truth observations was then used to analyze the spring phenological characteristics. Specifically, we consider the following questions:

(1) What are the spatio-temporal distribution patterns of the SOS and its correlation with climate change during the period 2001 to 2018 in the mountains of northwest Mongolia?
(2) How do the SOS, climate factors, and their relationships change with elevation?
(3) How does the legacy effect of SOS on vegetation growth vary with elevation?

2. Data and methods

2.1. Study area

The study area is located in the northwest of Mongolia and consists of the Sajan Mountains in the north and the Hangayn Mountains in the south, covering from approximately 44° to 52°N and 93° to 105°E, with an area of around 0.35 million km^2 (Fig. 1a). The region is characterized by river valleys and high mountains, where its highest peak (Tengri) is more than 3900 m above sea level (ASL). The area pitches up in the south and pitches down in the north and is one of the highest mountainous regions in Mongolia (Fig. 1b). The region is dominated by a typical temperate continental climate with extremely cold winters and warm summers. The mean temperature in January is below −30℃, and the mean temperature in July is below 18℃ (Fig. 1c). Shaped by local geographical conditions, water vapor sources originate from the Arctic Ocean. The wetter eastern and northern parts have annual mean precipitation of more than 300 mm, while the annual precipitation in the south and west is<100 mm (Fig. 1d). The dominant land cover types in the study area are natural grasslands (56.62%), shrubs (8.34%), and forests (11.36%, including broad-leaved forest and mixed forest) (Fig. 1a).

2.2. Datasets

2.2.1. Remote sensing data

This work employed the Normalized Difference Vegetation Index (NDVI, Tucker and Sellers, 1986), defined as the ratio of the difference between near-infrared reflectance and red visible reflectance to their sum, which is among the most commonly used vegetation indices for studying vegetation phenology (Peng et al., 2017; Testa et al., 2018; Zhu et al., 2019b). The SOS in this study was extracted from a series of datasets, namely the MOD13Q1_NDVI, MOD13A1_NDVI, and MOD13A2_NDVI datasets. The used data were obtained from the NASA Earth Observation System for the period 2001 to 2018 (https://ladsweb.modaps.eosdis.nasa.gov/search/). Specifically, all three MODIS datasets have the same temporal resolution (16 days), but different spatial resolutions: (1) MOD13Q1 at 250 m; (2) MOD13A1 at 500 m; (3) MOD13A2 at 1 km.

2.2.2. Climate data and auxiliary data

A climate dataset of monthly mean temperature and monthly precipitation values comes from 17 meteorological stations (black triangles in Fig. 1b) distributed across northwest Mongolia, provided by the Institute of Geography and Geoecology, Mongolian Academy of Science, for the period 2001 to 2018. To match the start of the vegetation growing season, we selected temperature and precipitation (including the spring and winter) as climate variables. These monthly climate data were then interpolated and resampled to a spatial resolution of 250 m in an ArcGIS environment using the kriging interpolation method. The elevation information of the study area was derived from a elevation with a 90-m resolution produced by the United States Geological Survey (USGS, Fig. 1b). To avoid anomalous fluctuations in topography caused by insufficient numbers of pixels, we excluded elevations with pixel counts<300, which resulted in an elevation range from 937 to 3437 m ASL being considered in this study. We took the annual average SOS, temperature, and precipitation at each 100 m elevation interval during the period 2001 to 2018 to analyze the climate and SOS variations, and their relationships.

The Global ESA CCI land cover classification map originates from the European Space Agency (http://maps.elie.ucl.ac.be/CCI/viewer/index.html). It has a spatial resolution of 300 m, and the time coverage is from 1992 to 2015. This paper used the Global ESA CCI land cover classification data for 2015. To minimize the effect of land cover type and snow cover, we first excluded barren land, water bodies, and evergreen coniferous forests (Hmimina et al., 2013). Second, pixels with

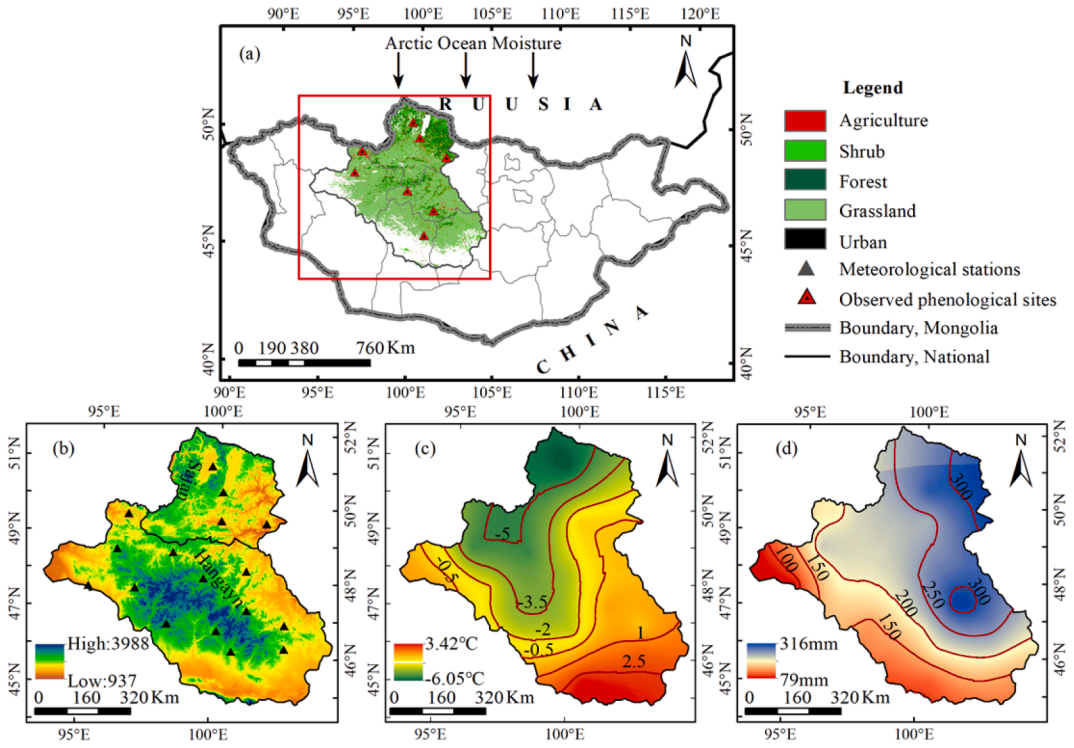

Fig. 1. (a) Geographic location, land cover types (2015), and observed phenological stations. (b) Elevation and meteorological stations. (c) Annual mean temperature, and (d) Annual mean precipitation in mountain of northwest Mongolia during 2001–2018.

18 years of mean NDVI values of < 0.1 were also excluded from the analysis (Zhou et al., 2001; Jeong et al., 2011) (Fig. 1a).

2.2.3. Observed phenological data

The observed phenological data consisted of ground-truth observational data (henceforth termed observations) from 8 meteorological stations in Mongolia between 2009 and 2016 (Table S1 and Fig. 1a). Each station is in a natural pasture which includes three to four herb species. In this study, we took the average value of the start of the growing season for multiple herb species as the observed phenological station data. However, the remote sensing dates for each station were defined as the mean value within a 1 km buffer zone.

2.3. Methods

2.3.1. Determination of remote sensing-inferred SOS

Previous studies have reported that the cumulative NDVI-based logistic model had greater potential than other methods for tracking vegetation phenology in the Mongolian plateau (e.g., Bao et al., 2017). In our study, the SOS was determined by the cumulative NDVI-based logistic model (Hou et al., 2014; Wu et al., 2016). This model is an improvement on the logistic model proposed by Zhang et al. (2003). First, we applied the Harmonic Analysis of Time Series (HANTS) smoothing algorithm smoothing to each year's 23 NDVI datasets (i.e., 16-day temporal resolution) and calculated the cumulative NDVI for each pixel of each year. The HANTS algorithm is a harmonic analysis based-series reconstruction method, which has been widely used to process time-series NDVI images and discards the noise caused by clouds or poor atmospheric conditions (Liu et al., 2016). Second, we fitted the cumulative NDVI using a four-parameter logistic model given by:

$$y(t) = \frac{c}{1 + e^{a+bt}} + d \tag{1}$$

where t is the day-of-year (DOY), y (t) is the NDVI value at time t, a and b are fitting parameters, c + d is the maximum NDVI value, and d is the background NDVI value. We then calculate the rate of change in the curvature, RCC, as described in the following:

$$RCC = b^3 zc\left\{\frac{3z(1-z)(1+z)^3\left[2(1+z)^3 + b^2c^2z\right]}{\left[(1+z)^4 + (bcz)^2\right]^{2.5}} - \frac{(1+z)^2(1+2z-5z^2)}{\left[(1+z)^4 + (bcz)^2\right]^{1.5}}\right\} \tag{2}$$

$$Z = e^{a+bt} \tag{3}$$

Finally, we determined the SOS when the RCC reaches its first local maximum values (Bao et al., 2019) (Fig. 2).

2.3.2. Validation of the remote sensing-derived SOS

To compare the SOS results from the MODIS datasets and the observations, we make use of the mean absolute error (MAE, Eq. (4)), root mean square error (RMSE, Eq. (5)), and the Pearson correlation coefficient (R, Eq. (6)), which are calculated as follows:

$$MAE = \frac{1}{n}\sum_{i=1}^{n}|x_i - y_i| \tag{4}$$

$$RMSE = \sqrt{\frac{\sum_{i=1}^{n}(x_i - y_i)^2}{n}} \tag{5}$$

$$R_{xy} = \frac{\sum_{i=1}^{n}(x_i - \bar{x})(y_i - \bar{y})}{\sqrt{\sum_{i=1}^{n}(x_i - \bar{x})^2}\sqrt{\sum_{i=1}^{n}(y_i - \bar{y})^2}} \tag{6}$$

where i is the serial number of the year, n is the number of samples, x_i is the average SOS of multiple species from the observations in the i-th year, y_i is the average remote-sensed SOS within a 1 km buffer zone in the i-th year, $\bar{x}$ is the multi-year average SOS of multiple species from the observations, and $\bar{y}$is the multi-year average remote-sensed SOS within a 1 km buffer zone.

MAE and RMSE are used to measure the difference between the

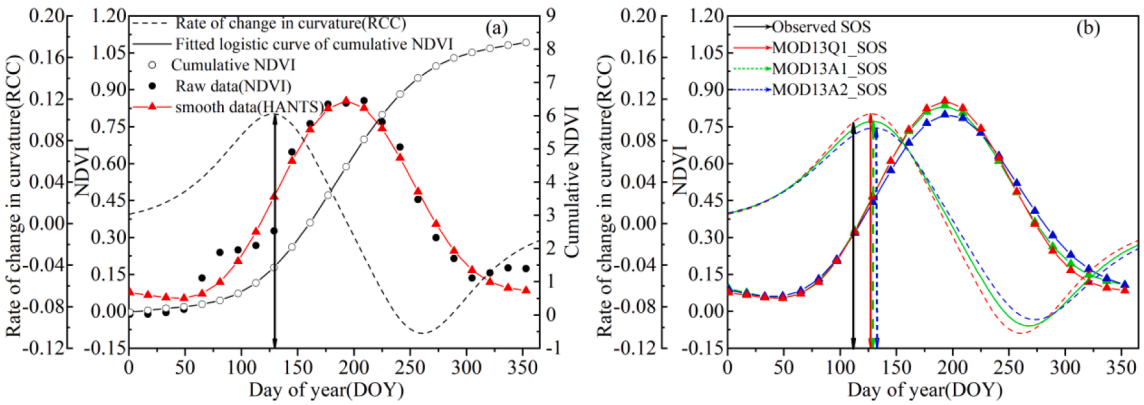

Fig. 2. (a) Example showing the determination of the SOS using the cumulative NDVI-based logistic models for the Tsetserleg (Site ID: 282) station in 2013. The arrows denote the calculated SOS from the fitted curves, and the corresponding horizontal axis coordinate is the day-of-year. (b) Using the same method at the same station and year to compare the observed SOS and remote sensing SOS with different spatial resolutions.

observed and remote sensing-derived dates (Zhang et al., 2013; Bórnez et al., 2020), while the correlation coefficient reflects the variation between the observed and remote sensing dates (An et al., 2020). To select the remote sensing data with the most effective spatial resolution, we identified the one that best reflects the observed phenology.

3. Results

3.1. Comparison of different spatial resolution MODIS datasets

We calculated the RMSE, MAE, and correlations between the observations and the MODIS datasets with different spatial resolutions (Fig. 3). The different MODIS datasets provided similar performances in terms of the acquired SOS dates, but were slightly overestimated when compared to the observed data, in agreement with Zhu et al. (2019b). The best agreement with the observations was found for the MOD13Q1 dataset, with an R of 0.58 ($p < 0.001$), RMSEs of 21 days, and MAEs of 19 days (Fig. 3a). Results for the SOS from datasets MOD13A1 and MOD13A2 showed a lower accuracy than MOD13Q1, with R values of 0.53 ($p < 0.001$, RMSE = 22 days, MAE = 20 days) and 0.50 ($p < 0.001$, RMSE = 23 days, MAE = 21 days), respectively. In general, we found the strongest correlations and smallest errors from the comparisons between the observations and MOD13Q1, indicating that the SOS estimates from this higher spatial resolution dataset agreed best with the observations. Accordingly, we used the MOD13Q1 data to extract the spring phenological characteristics and from these estimates established linear regression models based on the climatic factors for the study area.

3.2. Spatio-temporal patterns of spring phenology

Fig. 4a highlights the spatial distribution of the SOS estimates from 2001 to 2018 over the study area. The SOS generally occurred between DOY 120 to 152 (82.46%, Fig. 4a), corresponding to early May to early June in leap years. The earliest SOS were detected in the eastern and southern lower elevation areas (Fig. 4a), with later SOS found mostly in the western and northern parts over high-elevation areas. This finding is consistent with the change trends of SOS with elevation (Fig. 4c). The trend of the SOS advancement was −0.41 days/100 m in lower elevation areas below 1537 m ASL, and the delay was 1.85 days/100 m in higher elevation areas above 1537 m. However, the SOS overall exhibited a delaying trend with increasing elevation of 1.52 days/100 m (Fig. 4c).

We also calculated the interannual variation of SOS over the study area (Fig. 4d). Our results show no statistically significant trends for SOS throughout the entire study period from 2001 to 2018 (slope = 0.02, R^2 = 0.00, p = 0.46, Fig. 4d). However, two distinct trends between 2001 and 2009 and 2009 and 2018 can be identified. The SOS significantly advanced by 1.63 days/yr from 2001 to 2009, while after 2009, this weakened to 1.34 days/yr. From the spatial distributions of the trends in SOS between 2001 and 2018 across the study area (Fig. 4b), the delay in SOS (i.e., positive trends) was observed over 49.79% of the study area, and were mostly distributed in the southern part of the region. In comparison, the trend for advancing (i.e., negative) SOS trends accounted for 50.21% of the total area, which is more pronounced in the northern part of the study area.

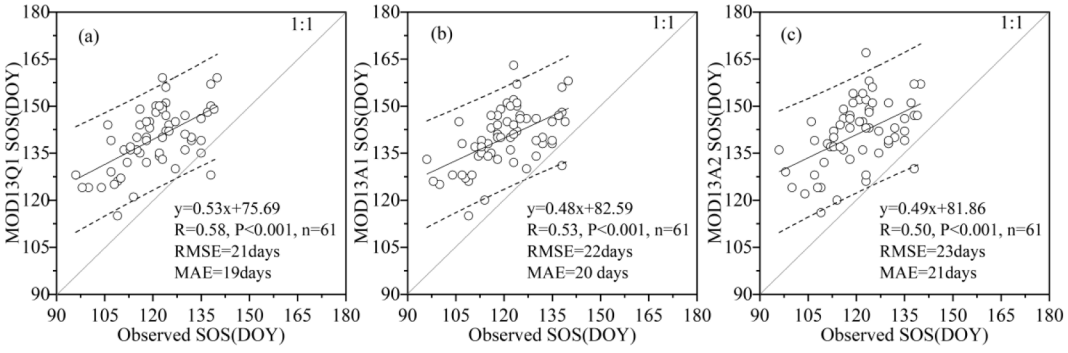

Fig. 3. Correlation coefficients between the different MODIS datasets and observations: (a) MOD13Q1, (b) MOD13A1, and (c) MOD13A2. The dotted lines indicate the 95% confidence intervals.

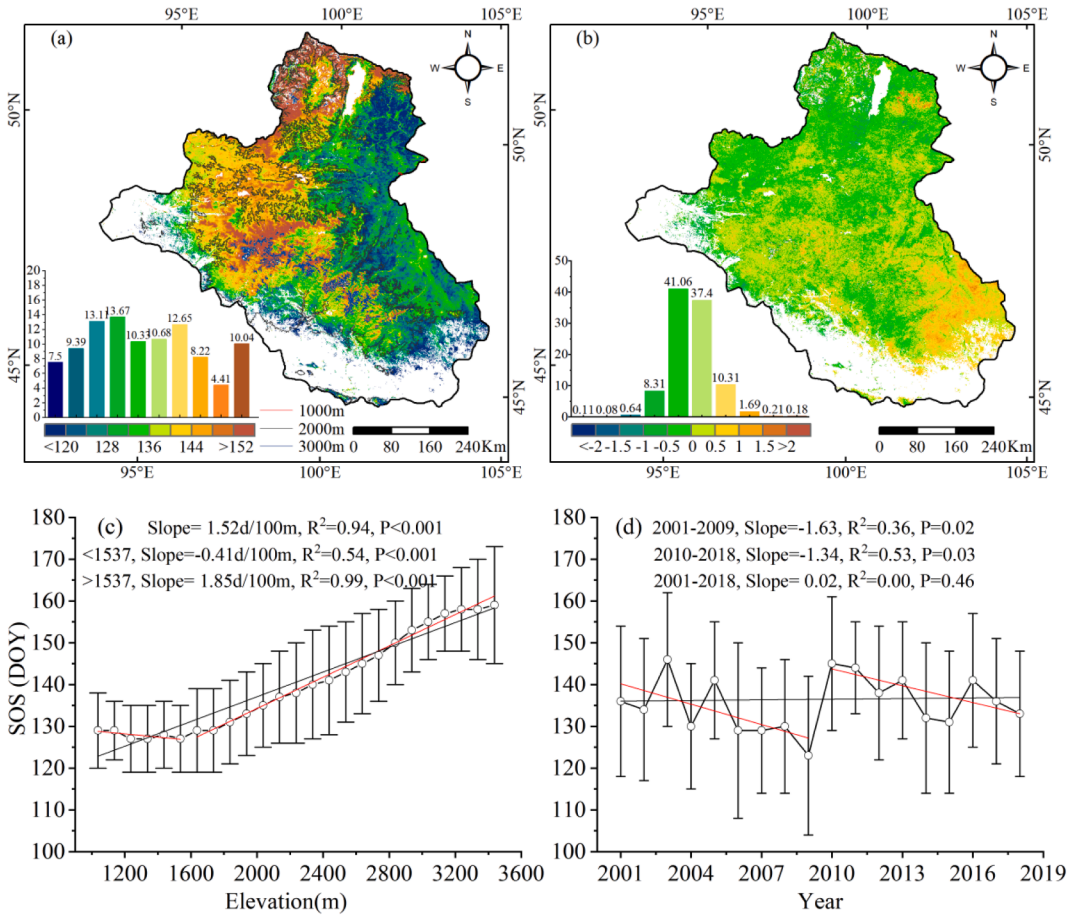

Fig. 4. Spatial distribution of (a) the SOS and (b) trends in the SOS over the study area from 2001 to 2018. (c) Change trends in SOS with elevation. (d) Interannual variations in SOS in the study area from 2001 to 2018. The error bars show standard deviations (SD) from the pixels within each elevation range.

3.3. Relationships between spring phenology and climate factors from 2001 to 2018

The correlation coefficients between the inferred SOS and climate factors between 2001 and 2018 are presented in Table 1. The SOS is significantly negatively correlated with both spring temperature and winter temperature, where for the winter temperature ($R = -0.472$, $p = 0.048$, Table 1), it indicates that the warming in winter advances the SOS. Advancing SOS dates were found over more than 92% of the study area, with around 20% of the pixels showing statistically significant advancement, which were distributed over most areas, except for the high elevation parts (Fig. 5b). The correlation coefficient between the SOS and spring temperature ($R = -0.606$, $p = 0.008$, Table 1) indicates that the increased spring temperatures advanced the SOS, which was observed across 97% of the study area, and about 36% of these correlations were statistically significant (Fig. 5a). We, therefore, note that the SOS was more strongly affected by spring temperature than by winter temperature, suggesting that spring temperature had a prominent influence on SOS in this study area.

By contrast to temperature, the SOS was positively correlated with both spring precipitation and winter precipitation between 2001 and 2018 (Table 1). The SOS shows a statistically significant positive correlation with winter precipitation, with $R = 0.628$ ($p = 0.005$, Table 1), which demonstrated that increased precipitation tends to delay the SOS. The winter precipitation was positively associated with the SOS for about 93% of the study area, distributed over most parts of the study area, with those correlations being significant covering about 27% of these areas (Fig. 5d). Meanwhile, the spring precipitation showed no overall significant positive correlation with SOS ($R = 0.332$, $p = 0.178$, Table 1), while spatially, a positive correlation between SOS and spring precipitation was observed at more than 73% of the pixels, with around 9% of these being statistically significant, mainly distributed in the western parts of the study area (Fig. 5c). On the other hand, the correlations between SOS and winter precipitation were generally positive (more than 93% of the study area) and more strongly so than the spring precipitation, suggesting winter precipitation was a driving factor for SOS in the study area.

Table 1
Correlation coefficient between SOS and climate variables between 2001 and 2018 (* and ** indicate $P < 0.05$ and $P < 0.01$, respectively).

Climate factors	Variable	Correlation coefficient (R)	P_value
Spring precipitation (Ps)	March-May	0.332	0.178
Winter precipitation (Pw)	December(last year)–February	0.628	0.005**
Spring temperature (Ts)	March-May	−0.606	0.008**
Winter temperature (Tw)	December(last year)–February	−0.472	0.048*

3.4. Elevation-dependent correlations between spring phenology and climate factors

Fig. 6 shows the linear trends of the climate factors during the period 2001 to 2018 for every 100 m elevation spacing, where all show statistical significance ($p < 0.01$). Between 937 and 2037 m ASL, the

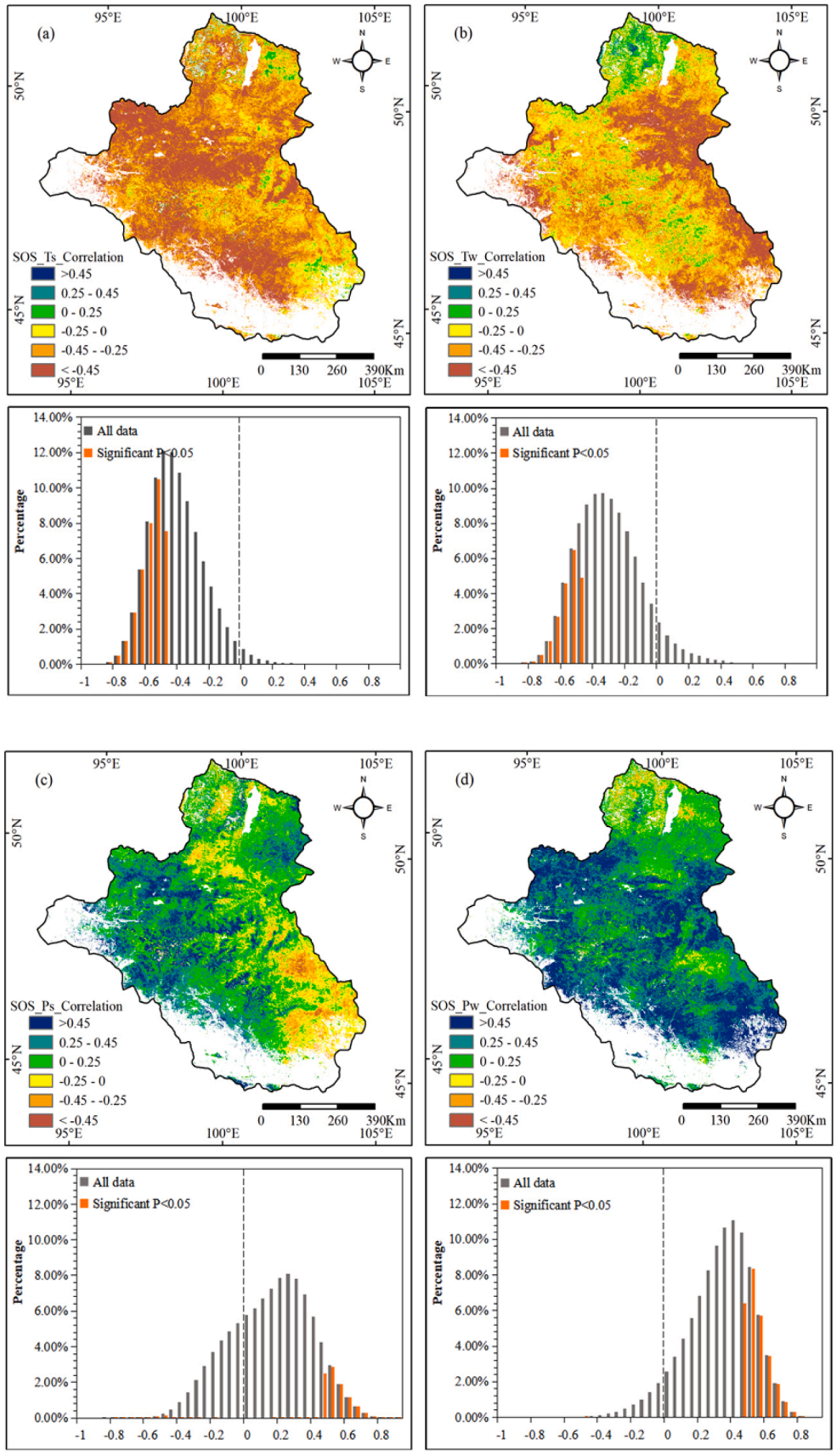

Fig. 5. Spatial patterns of the correlations between the SOS and (a) spring temperature, (b) winter temperature, (c) spring precipitation, and (d) winter precipitation and their subsequent significance (i.e., when $p < 0.05$).

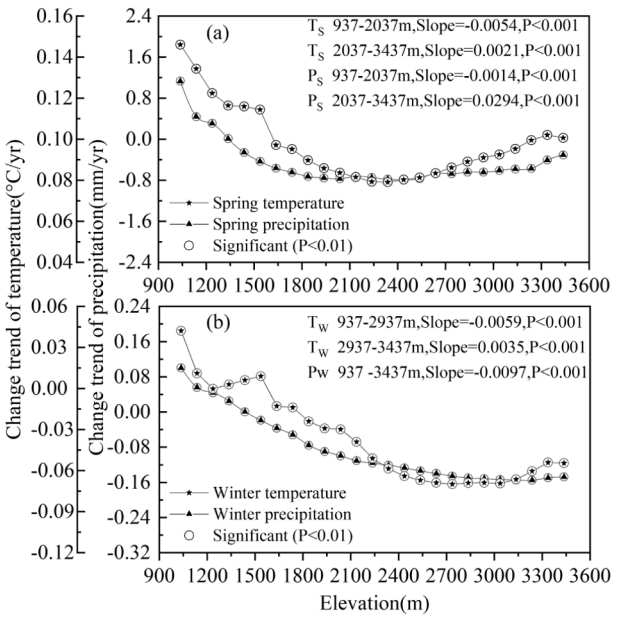

Fig. 6. Change trends of temperature and precipitation for spring (a) and winter (b) for each elevation interval in the study area. The circle indicates that the change trend has reached a statistically significant level of $p < 0.01$.

temperature and precipitation trends in spring show a decrease with increasing elevation, by −0.54℃/yr and −0.14 mm/yr per 100 m, respectively. However, these trends reverse with higher elevations between 2037 m and 3437 m ASL, with values of around 0.21℃/yr and 2.94 mm/yr per 100 m, respectively. Meanwhile, the winter precipitation showed a trend of decreasing values between 937 m and 3437 m ASL, with a value of 0.97 mm/yr per 100 m elevation, and the winter temperature trend with increasing elevations reversed from decreasing by −0.59℃/yr per 100 m (937 to 2937 m ASL) to increasing by 0.35℃/yr per 100 m (2937 to 3437 m ASL).

The relationships between SOS and climate factors exhibited different patterns with elevation (Fig. 7). The SOS showed a negative

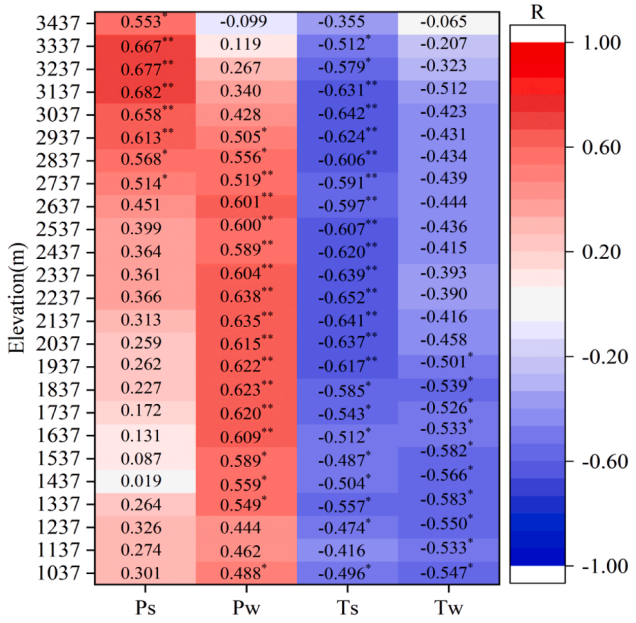

Fig. 7. The correlation coefficients of the SOS with temperature and precipitation with elevation in the study area. * indicates significance with $p < 0.05$, ** indicates significance with $p < 0.01$.

correlation with the temperature at all elevations, suggesting that decreasing temperatures lead to delayed SOS dates. Specifically, the correlations between SOS and spring temperature were strongly negative and statistically significant, except for the elevation ranges from 1037 to 1137 m and 3337 to 3437 m ASL. The winter temperature was negatively correlated with the SOS, with the correlation coefficients decreasing with increasing elevation, being statistically significant between 937 m and 1937 m ASL. Meanwhile, the SOS was positively correlated with precipitation at all elevations, indicating that increasing precipitation delayed the SOS. Among them, the relationships between SOS and winter precipitation showed a stronger positive significance between 1337 m and 2937 m ASL (Fig. 7), with the correlation coefficients decreasing with increasing elevation. Meanwhile, the SOS is significantly positively correlated with spring precipitation at higher elevations above 2737 m ASL. We have therefore observed that there is a strong dependence of SOS on spring temperature and winter precipitation with elevation.

3.5. *Elevation-dependent relationships between spring phenology and growth in spring and summer*

Based on the MOD13Q1_NDVI dataset, we used monthly average NDVI values to delegate spring (March to May) and summer growth (June to August). Fig. 8 highlights the relationship between spring and summer growth with SOS with respect to elevation. The results show that the SOS was strongly negatively correlated with spring growth at all elevations, with all being at a statistically significant level of at least $p < 0.05$ (Fig. 8). The correlation coefficients increase with elevation between 1537 m and 2937 m ASL, but then decreased over higher elevations from 2937 m to 3437 m ASL. From the correlation coefficients between SOS and summer growth (Fig. 8), no statistically significant coefficients between SOS and summer growth were negative below 1437 m ASL, but above this elevation the coefficients between SOS and summer growth were positive. Between 1437 m and 2937 m ASL, the coefficients between SOS and summer growth increased with elevation and reached statistically significant levels between 2337 m and 2937 m ASL. However, these correlations again decreased between 2937 m and 3437 m ASL. In addition, we observed that the absolute values of the coefficients between the SOS and spring growth were greater than those between SOS and summer growth at all elevations, indicating the effect of the SOS on spring growth was substantially greater than on summer growth.

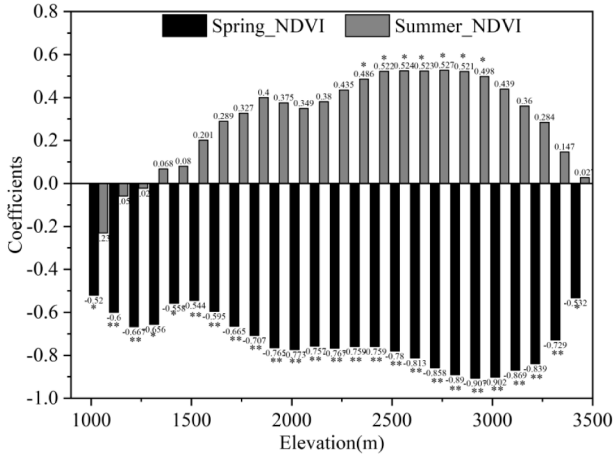

Fig. 8. Correlation between the SOS and spring and summer growth as a function of elevation. * indicates significance at $p < 0.05$, ** indicates significance at $p < 0.01$.

4. Discussion

4.1. The response of spring phenology on climate change in the mountains of northwest Mongolia

Our results indicate that between 2001 and 2018, the SOS remained relatively stable, with no clear trends for ecosystems in the mountains of northwest Mongolia, which generally agrees with the findings of previous studies (Cong et al., 2013; Wang et al., 2014; Zhou et al., 2016; Du et al., 2020). However, the SOS interannual change displays two distinct stages over this period: First, the SOS significantly advanced by 1.63 days/yr before 2009, after which this trend weakened where it showed an advance of 1.34 days/yr. This is consistent with the findings of Zhou et al. (2016), which may be related to in winter precipitation over the study area during this period (Fig. S3).

Our results show that the SOS occurs earlier at lower elevations, and later at higher elevations, in agreement with Shen et al. (2014) and Piao et al. (2011a). Additionally, we also found the changes in SOS dates are closely related to changes in both winter precipitation and spring temperature (Fig. 5 and Fig. 7). In our study area, variations in spring temperature played a significant role between 2001 and 2018 (Table 1 and Fig. 7). Warmer spring temperatures tended to advance the SOS, as reflected in the significant negative correlation between these parameters in most parts of the study area (Fig. 5a). Meanwhile, the relationships between SOS and spring temperature were also strongly significantly negative within all elevation ranges considered, except for from 1037 m to 1137 m, and 3337 m to 3437 m ASL. Because warmer temperatures during spring enhanced the accumulation of heat needed for budburst and leaf expansion, this resulted in the advancement of the resumption of active growth (He et al., 2018; Wang et al., 2017b; Yu et al., 2010). Furthermore, our results indicate that decreasing winter temperatures played a negative role in the advancement of SOS, especially at lower elevations (937 to 1937 m ASL). Plants in high-elevation regions have adapted to these areas' cold climates as a result of their long-term exposure to lower temperatures (Du et al., 2019), whereas plants often have a low resistance to frost in low-elevation areas, hence, to minimize the danger of freezing injury at lower temperatures, they may slow or postpone phenological processes, and thus delay the SOS (Richardson et al., 2013; Du et al., 2019).

We also found that winter precipitation explained a substantial portion of the variability in SOS, with our analysis showing significant positive responses of the SOS to winter precipitation over most of the study area, consistent with previous findings (Yun et al., 2018). Likewise, the increasing winter precipitation delayed the SOS in the following spring at elevation (Fig. 7). Because winter precipitation is frequently in the form of snow, an anomalously widespread snow cover will reduce the absorption of solar radiation and requires more heat to melt the snow and to warm the soil, thus potentially delaying the SOS (Wang et al., 2017a; Xie et al., 2017; Yun et al., 2018). Furthermore, scattered portions of the study area at elevations above 2737 m ASL saw the SOS being significantly positively correlated with spring precipitation, indicating that wet springs can delay the SOS. A possible reason for this is that snow and glacier ice distributed at high elevations can slow down climate warming by reflecting solar radiation and consuming energy due to snow or ice melting (Tao et al., 2015), thus possibly delaying the SOS. Another possible explanation is that increasing spring precipitation (2.94 mm/yr per 100 m, Fig. 6) leads to a decrease in temperature, resulting again in a delay in the SOS. In general, our results consequently support the notion that the phenological events of most mountainous regions are not solely driven by spring temperature, but also by winter precipitation.

4.2. The legacy effects of spring phenology on vegetation growth with variation in elevation

Previous studies have reported legacy effects of SOS that have been found to both increasing and decreasing vegetation growth (Piao et al., 2011b; Wang et al., 2011). Our results showed that the SOS affects vegetation growth during spring and summer with respect to elevation, consistent with the results of Zhou et al (2020) for temperate China. The SOS was significantly negatively correlated with spring growth at all elevations, but for the summer growth, the SOS was negatively correlated with summer growth below 1437 m ASL and positively correlated with summer growth above 1437 m ASL. In low-elevation areas (below 1437 m), we observed SOS to be negatively correlated with spring and summer growth, and reached a statistically significant level with spring growth. This is likely because temperatures in lower-elevation areas are greater than those at higher elevations. This sees the relatively high temperatures advancing the SOS (−0.41 days/100 m), which extends the growing season's length, thus promoting vegetation growth. From 1437 m to 2937 m ASL, the SOS is negatively correlated with spring growth and the resulting correlation coefficients increase with elevation (Fig. 8). Because temperature and precipitation delay SOS (1.85 days/100 m) with increasing elevation, a delayed SOS may result in the delayed maturation of leaves, leading to lower rates of photosynthesis and vegetation growth in spring (Zhang et al., 2004; Zhou et al., 2020). Regarding summer growth, the SOS is positively correlated with summer growth between 1437 m and 2937 m ASL, with the correlation coefficients increasing with elevation. Other studies have found that the length of the growing season was markedly shortened with increasing elevation (Deng et al., 2018; Zhu et al., 2019a). Meanwhile, the SOS was delayed with increasing elevation, which may lead to increasing vegetation growth in summer, while in this work, the correlation coefficients of the SOS with spring and summer growth were weaker at higher elevations (above 2937 m ASL). Aerts et al. (2006) and He et al. (2015) have demonstrated that the start of the vegetation growth of cold biomes seems to be particularly sensitive to climate warming at higher elevations. This may be an effect of SOS which has been weakened by drastically increased temperatures and increased precipitation (Fig. 6 and Fig. 4c). In addition, our results showed that the correlation coefficients between SOS and spring growth were greater than those between SOS and summer growth (Fig. 8). Considering elevation, the effect of SOS is reduced during the growing season from spring to summer.

5. Conclusions

In this study, we compared three MODIS datasets with different spatial resolutions and selected the MODIS data closest to the observations to represent the spring phenological characteristics. Combined with climate factors, we analyzed the spatio-temporal patterns and elevation change mechanisms of the SOS and its legacy effect on vegetation growth in the mountains of northwest Mongolia. The MOD13Q1 data (250 m) compared to the MOD13A1 (500 m) and MOD13A2 (1 km) datasets, confirming that the high-spatial-resolution data had the better potential for tracking and predicting phenology. Considering the regional and elevation gradient, the variation of SOS is mainly influenced by spring temperature and winter precipitation where increasing spring temperatures tend to advance the SOS, while increasing precipitation in winter tends to delay the SOS. For the vegetation growth, in lower elevation areas (below 1437 m ASL), the advancing SOS increases vegetation growth during spring and summer. However, a delay in SOS decreases spring growth and increases summer growth in high-elevation areas. The effect of the SOS weakens as the growing season progresses from spring to summer.

The results of this study will assist in gaining a better understanding of the spatio-temporal patterns and elevation dependencies of the change mechanisms of SOS in the mountains of northwest Mongolia, as well as showing the importance of winter precipitation for spring phenological development in mountainous areas. Also, this study allows a description of the functional consequences of SOS variations on vegetation growth. Although temperature and precipitation play important roles in vegetation spring phenology, the mechanisms of

vegetation phenological response to climate change are very complex and are likely to be affected by other environmental factors, such as snow cover, sunshine duration, and soil moisture. Therefore, in future studies, it will be necessary to examine how these environmental factors impact upon the spring phenological stages. Additionally, the phenology of mountain vegetation, which is a significant indicator of climate change (Zhu et al., 2019). Thus, it is equally important to understanding the dynamics of the change in both the end of the growing season (EOS) and length of the growing season (LOS) in mountains, which will be focus of our future research.

CRediT authorship contribution statement

Li Mei: Conceptualization, Methodology, Software, Validation, Formal analysis, Writing - original draft. **Gang Bao:** Conceptualization, Methodology, Software, Writing - review & editing. **Siqin Tong:** Resources, Data curation, Writing - review & editing. **Shan Yin:** Investigation, Validation, Writing - review & editing. **Yuhai Bao:** Supervision, Investigation, Project administration, Funding acquisition. **Kang Jiang:** Data curation, Software. **Yu Hong:** Visualization. **Alateng Tuya:** Data curation, Writing - review & editing. **XiaoJun Huang:** Investigation, Writing - review & editing.

Declaration of Competing Interest

The authors declare that they have no known competing financial interests or personal relationships that could have appeared to influence the work reported in this paper.

Acknowledgments

This study was supported by the National Natural Science Foundation of China [grant numbers 61631011, 41961144019]. The authors would like to thank all the reviewers who participated in the review and MJEditor (www.mjeditor.com) for their linguistic assistance during the preparation of this manuscript.

Appendix A. Supplementary data

Supplementary data to this article can be found online at https://doi.org/10.1016/j.ecolind.2021.107640.

References

An, S., Chen, X., Zhang, X., Lang, W., Ren, S., Xu, L., 2020. Precipitation and Minimum Temperature are Primary Climatic Controls of Alpine Grassland Autumn Phenology on the Qinghai-Tibet Plateau. Remote Sensing 12 (3), 431. https://doi.org/10.3390/rs12030431.

Aerts, R., Cornelissen, J.H.C., Dorrepaal, E., 2006. Plant performance in a warmer world: general responses of plants from cold, northern biomes and the importance of winter and spring events. Plant Ecol. 182, 65–77. https://doi.org/10.1007/s11258-005-9031-1.

Bórnez, K., Descals, A., Verger, A., Peñuelas, J., 2020. Land surface phenology from VEGETATION and PROBA-V data. Assessment over deciduous forests. Int. J. Appl. Earth Obs. Geoinf. 84, 101974. https://doi.org/10.1016/j.jag.2019.101974.

Bao, G., Bao, Y., Bao, Y.A.L., 2017. Spatio-temporal dynamics of vegetation phenology in the Mongolian plateau during 1982–2011. Rem. Sens. Technol. Appl. 32 (5), 866–874. https://doi.org/10.11873/j.issn.1004-0323.2017.5.0866 (Chinese).

Bao, G., Chen, J., Chopping, M., Bao, Y., Bayarsaikhan, S., Dorjsuren, A., Tuya, A., Jirigala, B., Qin, Z., 2019. Dynamics of net primary productivity on the Mongolian Plateau: Joint regulations of phenology and drought. Int. J. Appl. Earth Obs. Geoinf. 81, 85–97. https://doi.org/10.1016/j.jag.2019.05.009.

Borchert, R., Rivera, G., Hagnauer, W., 2002. Modification of vegetative phenology in a tropical semi-deciduous forest by abnormal drought and rain 1. Biotropica 34 (1), 27–39. https://doi.org/10.1646/0006-3606(2002)034[0027:movpia]2.0.co;2.

Cong, N., Wang, T., Nan, H., Ma, Y., Wang, X., Myneni, R.B., Piao, S., 2013. Changes in satellite-derived spring vegetation green-up date and its linkage to climate in China from 1982 to 2010: a multimethod analysis. Glob. Change Biol. 19 (3), 881–891. https://doi.org/10.1111/gcb.2013.19.issue-310.1111/gcb.12077.

Chen, L., Huang, J., Ma, Q., Hänninen, H., Rossi, S., Piao, S., Bergeron, Y., 2018. Spring phenology at different altitudes is becoming more uniform under global warming in Europe. Glob Chang. Biol. 24 (9), 3969–3975. https://doi.org/10.1111/gcb.2018.24.issue-910.1111/gcb.14288.

Deng, C., Bai, H., Gao, S., Zhao, T., Ma, X., 2018. Differences and variations in the elevation-dependent climatic growing season of the northern and southern slopes of the Qinling Mountains of China from 1985 to 2015. Theor. Appl. Climatol. 137 (1–2), 1159–1169. https://doi.org/10.1007/s00704-018-2654-7.

Du, J., He, Z., Piatek, K.B., Chen, L., Lin, P., Zhu, X., 2019. Interacting effects of temperature and precipitation on climatic sensitivity of spring vegetation green-up in arid mountains of China. Agric. For. Meteorol. 269–270, 71–77. https://doi.org/10.1016/j.agrformet.2019.02.008.

Du, J., Li, K., He, Z., Chen, L., Lin, P., Zhu, X., 2020. Daily minimum temperature and precipitation control on spring phenology in arid-mountain ecosystems in China. Int. J. Climatol. 40 (5), 2568–2579. https://doi.org/10.1002/joc.v40.510.1002/joc.6351.

He, Z., Du, J., Zhao, W., Yang, J., Chen, L., Zhu, X., Chang, X., Liu, H., 2015. Assessing temperature sensitivity of subalpine shrub phenology in semi-arid mountain regions of China. Agric. For. Meteorol. 213, 42–52. https://doi.org/10.1016/j.agrformet.2015.06.013.

He, Z., Du, J., Chen, L., Zhu, X., Lin, P., Zhao, M., Fang, S., 2018. Impacts of recent climate extremes on spring phenology in arid-mountain ecosystems in China. Agric. For. Meteorol. 260–261, 31–40. https://doi.org/10.1016/j.agrformet.2018.05.022.

Huang, K.-Y., 2002. Evaluation of the topographic sheltering effects on the spatial pattern of Taiwan fir using aerial photography and GIS. Int. J. Remote Sens. 23 (10), 2051–2069. https://doi.org/10.1080/01431160110076207.

Hmimina, G., Dufrêne, E., Pontailler, J.-Y., Delpierre, N., Aubinet, M., Caquet, B., de Grandcourt, A., Burban, B., Flechard, C., Granier, A., Gross, P., Heinesch, B., Longdoz, B., Moureaux, C., Ourcival, J.-M., Rambal, S., Saint André, L., Soudani, K., 2013. Evaluation of the potential of MODIS satellite data to predict vegetation phenology in different biomes: An investigation using ground-based NDVI measurements. Remote Sens. Environ. 132, 145–158. https://doi.org/10.1016/j.rse.2013.01.010.

Hou, X., Gao, S., Niu, Z., Xu, Z., 2014. Extracting grassland vegetation phenology in North China based on cumulative SPOT-VEGETATION NDVI data. Int. J. Remote Sens. 35 (9), 3316–3330. https://doi.org/10.1080/01431161.2014.903437.

IPCC, 2013. Climate Change 2013: The Physical Science Basis. Contribution of Working Group I to the Fifth Assessment Report of the Intergovernmental Panel on Climate Change. Cambridge University Press, Cambridge, United Kingdom and New York, NY, USA.

Jeong, S.J., Ho, C.H., GIM, H.J., Brown, M.E., 2011. Phenology shifts at start vs. end of growing season in temperate vegetation over the Northern Hemisphere for the period 1982–2008. Glob. Change Biol. 17 (7), 2385–2399. https://doi.org/10.1111/j.1365-2486.2011.02397.x.

Jin, X., Wan, L., Zhang, Y.-K., Hu, G., Schaepman, M.E., Clevers, J.G.P.W., Su, Z.B., 2009. Quantification of spatial distribution of vegetation in the Qilian Mountain area with MODIS NDVI. Int. J. Remote Sens. 30 (21), 5751–5766. https://doi.org/10.1080/01431160902736635.

Jin, J., Jiang, H., Zhang, X., Wang, Y., 2012. Characterizing spatial-temporal variations in vegetation phenology over the north-south transect of northeast Asia based upon the meris terrestrial chlorophyll index. Terr. Atmos. Ocean. Sci. 23 (4), 413. https://doi.org/10.3319/TAO.2012.03.12.01(A).

Keenan, Trevor F., Gray, Josh, Friedl, Mark A., Toomey, Michael, Bohrer, Gil, Hollinger, David Y., Munger, J. William, O'Keefe, John, Schmid, Hans Peter, Wing, Ian Sue, Yang, Bai, Richardson, Andrew D., 2014. Net carbon uptake has increased through warming-induced changes in temperate forest phenology. Nat. Clim. Change 4 (7), 598–604. https://doi.org/10.1038/nclimate2253.

Liu, Q., Fu, Y.S., Zeng, Z.Z., Huang, M.T., Li, X.R., Piao, S.L., 2016. Temperature, precipitation, and insolation effects on autumn vegetation phenology in temperate China. Global Change Biology 2016 (22), 644–655. https://doi.org/10.1111/gcb.13081.

Ma, X., Huete, A., Moran, S., Ponce-Campos, G., Eamus, D., 2015. Abrupt shifts in phenology and vegetation productivity under climate extremes. J. Geophys. Res. 120 (10), 2036–2052. https://doi.org/10.1002/2015JG003144.

Parmesan, Camille, 2006. Ecological and evolutionary responses to recent climate change. Annu. Rev. Ecol. Evol. Syst. 37 (1), 637–669. https://doi.org/10.1146/annurev.ecolsys.37.091305.110100.

Piao, S., Cui, M., Chen, A., Wang, X., Ciais, P., Liu, J., Tang, Y., 2011a. Altitude and temperature dependence of change in the spring vegetation green-up date from 1982 to 2006 in the Qinghai-Xizang Plateau. Agric. For. Meteorol. 151 (12), 1599–1608. https://doi.org/10.1016/j.agrformet.2011.06.016.

Piao, S., Wang, X., Ciais, P., Zhu, B., Liu, J. 2011b. Changes in satellite-derived vegetation growth trend in temperate and boreal Eurasia from 1982 to 2006. Glob. Change Biol. 17 (10), 3228–3239. doi:10.1111/j.1365-2486.2011.02419.x.

Peng, D., Wu, C., Li, C., Zhang, X., Liu, Z., Ye, H., Luo, S., Liu, X., Hu, Y., Fang, B., 2017. Spring green-up phenology products derived from MODIS NDVI and EVI: Intercomparison, interpretation and validation using National Phenology Network and AmeriFlux observations. Ecol. Ind. 77, 323–336. https://doi.org/10.1016/j.ecolind.2017.02.024.

Richardson, A.D., Hollinger, D.Y., Dail, D.B., Lee, J.T., Munger, J.W., O'Keefe, J., 2009. Influence of spring phenology on seasonal and annual carbon balance in two contrasting New England forests. Tree Physiol 29 (3), 321–331. https://doi.org/10.1093/treephys/tpn040.

Richardson, A.D., Keenan, T.F., Migliavacca, M., Ryu, Y., Sonnentag, O., Toomey, M., 2013. Climate change, phenology, and phenological control of vegetation feedbacks to the climate system. Agric. For. Meteorol. 169, 156–173. https://doi.org/10.1016/j.agrformet.2012.09.012.

Shen, M., Zhang, G., Cong, N., Wang, S., Kong, W., Piao, S., 2014. Increasing altitudinal gradient of spring vegetation phenology during the last decade on the Qinghai-Tibetan Plateau. Agric. For. Meteorol. 189-190, 71–80. https://doi.org/10.1016/j.agrformet.2014.01.003.

Shen, M., Piao, S., Cong, N., Zhang, G., Jassens, I.A., 2015. Precipitation impacts on vegetation spring phenology on the Tibetan plateau. Glob. Change Biol. 21 (10), 3647–3656. https://doi.org/10.1111/gcb.12961.

TUCKER, C.J., SELLERS, P.J., 1986. Satellite remote sensing of primary production. Int. J. Remote Sens. 7 (11), 1395–1416.

Tao, J., Zhang, Y., Dong, J., Fu, Y., Zhu, J., Zhang, G., Jiang, Y., Tian, L., Zhang, X., Zhang, T., Xi, Y., 2015. Elevation-dependent relationships between climate change and grassland vegetation variation across the Qinghai-Xizang Plateau. Int. J. Climatol. 35 (7), 1638–1647. https://doi.org/10.1002/joc.2015.35.issue-710.1002/joc.4082.

Testa, S., Soudani, K., Boschetti, L., Borgogno Mondino, E., 2018. MODIS-derived EVI, NDVI and WDRVI time series to estimate phenological metrics in French deciduous forests. Int. J. Appl. Earth Obs. Geoinf. 64, 132–144. https://doi.org/10.1016/j.jag.2017.08.006.

Wang, X., Piao, S., Ciais, P., Li, J., Friedlingstein, P., Koven, C., Chen, A., 2011. Spring temperature change and its implication in the change of vegetation growth in North America from 1982 to 2006. Proc. Natl. Acad. Sci. 108 (4), 1240–1245. https://doi.org/10.2307/41001845.

Wang, Y., Shen, Y., Sun, F., Chen, Y., 2014. Evaluating the vegetation growing season changes in the arid region of northwestern China. Theor. Appl. Climatol. 118 (3), 569–579. https://doi.org/10.1007/s00704-013-1078-7.

Wang, X., Zhou, Y., Wen, R., Zhou, C., Xu, L., Xi, X., 2020. Mapping spatiotemporal changes in vegetation growth peak and the response to climate and spring phenology over Northeast China. Remote Sens. 12 (23) https://doi.org/10.3390/rs12233977.

Wu, C., Hou, X., Peng, D., Gonsamo, A., Xu, S., 2016. Land surface phenology of China's temperate ecosystems over 1999–2013: spatial–temporal patterns, interaction effects, covariation with climate and implications for productivity. Agric. For. Meteorol. 216, 177–187. https://doi.org/10.1016/j.agrformet.2015.10.015.

Wang, Xufeng, Xiao, Jingfeng, Li, Xin, Cheng, Guodong, Ma, Mingguo, Che, Tao, Dai, Liyun, Wang, Shaoying, Wu, Jinkui, 2017a. No Consistent Evidence for Advancing or Delaying Trends in Spring Phenology on the Tibetan Plateau. J. Geophys. Res. Biogeosci. 122 (12), 3288–3305. https://doi.org/10.1002/jgrg.v122.1210.1002/2017JG003949.

Wang, X., Gao, Q., Wang, C., Yu, M., 2017b. Spatiotemporal patterns of vegetation phenology change and relationships with climate in the two transects of East China. Global Ecol. Conserv. 10, 206–219. https://doi.org/10.1016/j.gecco.2017.01.010.

Yu, H., Luedeling, E., Xu, J., 2010. Winter and spring warming result in delayed spring phenology on the Tibetan Plateau. Proc. Natl. Acad. Sci. U.S.A. 107 (51), 22151–22156. https://doi.org/10.1073/pnas.1012490107.

Yun, J., Jeong, S., Ho, C., Park, C., Park, H., Kim, J., 2018. Influence of winter precipitation on spring phenology in boreal forests. Glob Change Biol. 24 (11), 5176–5187. https://doi.org/10.1111/gcb.2018.24.issue-1110.1111/gcb.14414.

Xie, J., Kneubühler, M., Garonna, I., Notarnicola, C., Gregorio, L.D., Jong, R.D., Chimani, B., Schaepman, M.E., 2017. Altitude-dependent influence of snow cover on alpine land surface phenology. J. Geophys. Res.: Biogeosci. 122 (5), 1107–1120. https://doi.org/10.1002/2016jg003728.

Yang, Y., Zhang, L., Li, H., He, H., Wei, Y., Luo, J., Zhang, G., Huang, Y., Li, Y., Zhou, H., 2018. Soil physicochemical properties and vegetation structure along an elevation gradient and implications for the response of alpine plant development to climate change on the northern slopes of the Qilian Mountains. J. Mountain Sci. 15 (5), 1006–1019. https://doi.org/10.1007/s11629-017-4637-z.

Zhou, L., Tucker, C.J., Kaufmann, R.K., Slayback, D., Shabanov, N.V., Myneni, R.B., 2001. Variations in northern vegetation activity inferred from satellite data of vegetation index during 1981 to 1999. J. Geophys. Res. Atmosph. 106 (D17), 20069–20083. https://doi.org/10.1029/2000jd000115.

Zhang, X., Friedl, M., Schaaf, C., Strahler, A., Hodges, J., Gao, F., Reed, B., Huete, A., 2003. Monitoring vegetation phenology using MODIS. Remote Sens. Environ. 84 (3), 471–475. https://doi.org/10.1016/S0034-4257(02)00135-9.

Zhang, X., Friedl, M.A., Schaaf, C.B., Strahler, A.H., 2004. Climate controls on vegetation phenological patterns in northern mid-and high latitudes inferred from MODIS data. Glob. Change Biol. 10 (7), 1133–1145. https://doi.org/10.1111/j.1529-8817.2003.00784.x.

Zhang, G., Zhang, Y., Dong, J. & Xiao, X. 2013.Green-up dates in the Tibetan Plateau have continuously advanced from 1982 to 2011. Proceed. Natl. Acad. Sci. U.S.A., 110: 4309–4314. doi: 10.1073/pnas.1210423110.

Zhou, J.H., Cai, W.T., Qin, Y., Lai, L.M., Guan, T.Y., Zhang, X.L., Jiang, L.H., Du, H., Yang, D.W., Cong, Z.T., Zheng, Y.R., 2016. Alpine vegetation phenology dynamic over 16 years and its covariation with climate in a semi-arid region of China. Sci. Total Environ. 572, 119–128. https://doi.org/10.1016/j.scitotenv.2016.07.206.

Zhu, W., Zhang, X., Zhang, J., Zhu, L., 2019a. A comprehensive analysis of phenological changes in forest vegetation of the Funiu Mountains, China. J. Geograph. Sci. 29 (1), 131–145. https://doi.org/10.1007/s11442-019-1588-z.

Zhu, Y., Zhang, Y., Zu, J., Wang, Z., Huang, K., Cong, N., Tang, Z., 2019b. Effects of data temporal resolution on phenology extractions from the alpine grasslands of the Tibetan Plateau. Ecol. Ind. 104, 365–377. https://doi.org/10.1016/j.ecolind.2019.05.004.

Zhou, X., Geng, X., Yin, G., Hänninen, H., Hao, F., Zhang, X.H., Fu, Y., 2020. Legacy effect of spring phenology on vegetation growth in temperate China. Agric. For. Meteorol. 281 https://doi.org/10.1016/j.agrformet.2019.107845.

remote sensing

MDPI

Article

Variation Characteristics of Ecosystem Water Use Efficiency and Its Response to Human Activity and Climate Change in Inner Mongolia

Li Mei [1], Siqin Tong [1,2,*], Shan Yin [1,3], Yuhai Bao [1,3], Xiaojun Huang [1,3] and Tuya Alateng [1]

[1] College of Geographical Science, Inner Mongolia Normal University, Hohhot 010022, China
[2] Inner Mongolia Key Laboratory of Disaster and Ecological Security on the Mongolian Plateau, Inner Mongolia Normal University, Hohhot 010022, China
[3] Inner Mongolia Key Laboratory of Remote Sensing and Geographic Information Systems, Inner Mongolia Normal University, Hohhot 010022, China
* Correspondence: tongsq223@imnu.edu.cn

Abstract: Water use efficiency (WUE) reflects the balance between carbon assimilation and water consumption in terrestrial ecosystems. Considering the fragile conditions of global water resources, the evaluation of regional WUE variation characteristics and response mechanisms is critical for promoting sustainable ecological development and water resource utilization. Based on gross primary productivity (GPP) and evapotranspiration (ET) datasets, combined with vegetation and meteorological data, this study examined the spatiotemporal variations, annual variation contribution rate, and driving mechanism of WUE in Inner Mongolia from 2001 to 2020. The main results are as follows: (1) The interannual and spatial variations of GPP, ET, and WUE all exhibited increasing trends, with WUE increasing in approximately 70% of the region and significantly increasing in 22.35% of pixels exhibiting a significant increase. Areas with the most significant increases were located in the Horqin sandy land and Mu Us sandy land. (2) The highest WUE values were observed in the summer season, followed by autumn and winter, and the lowest in spring. (3) Among all vegetation types, the typical steppe ecosystems contributed most to the interannual variability (IAV) of GPP, ET, and WUE, with values of 169.89%, 141.09%, and 193.42%, respectively. While the coniferous forest contributed least or negatively to GPP, ET, and WUE IAV, with values of −36.28%, 28.20%, and −32.86%, respectively. (4) The primary driver of WUE variation was found to be GPP, which contributed 59.36%, mainly in the central and western regions. The remaining 40.64% was attributable to ET, concentrated in the northeast region. (5) Human activities significantly affected WUE, with a contribution (about 53.52%) larger than that of climate change (nearly 46.48%). Increased precipitation improves vegetation WUE and is the most important climate factor influencing WUE variations. These findings will aid the formulation of vegetation protection and water resource management strategies in water-stressed areas.

Keywords: water use efficiency; interannual variability (IAV); relative contribution; sensitivity

Citation: Mei, L.; Tong, S.; Yin, S.; Bao, Y.; Huang, X.; Alateng, T. Variation Characteristics of Ecosystem Water Use Efficiency and Its Response to Human Activity and Climate Change in Inner Mongolia. *Remote Sens.* **2022**, *14*, 5422. https://doi.org/10.3390/rs14215422

Academic Editor: Pradeep Wagle

Received: 15 September 2022
Accepted: 25 October 2022
Published: 28 October 2022

1. Introduction

The carbon dioxide (CO_2) level in the atmosphere has increased exponentially since the industrial revolution [1–3]. The continuous increase of atmospheric CO_2 had a significant effect on the patterns of the carbon–water cycle and the carbon–water balance of exchanges in terrestrial ecosystems, posing serious threats to ecological sustainability and human survival [1]. Water use efficiency (WUE) is a common variable for measuring the interaction of carbon assimilation and water loss in terrestrial ecosystems, it is also an important parameter reflecting the sensitivity of ecosystems to climate change [4–6]. The vegetation WUE consists of two main components: gross primary productivity (GPP) and

evapotranspiration (ET) [6–8]. GPP is the amount of carbon fixed by terrestrial vegetation via photosynthesis and represents the largest carbon flux in the global terrestrial carbon cycle [9–11]. ET is an important water vapor flux that refers to the water used by an ecosystem through transpiration or surface evaporation and influences water and energy distribution between the land surface and the atmosphere [12]. The study of vegetation WUE can not only provide an in-depth understanding of ecosystem change patterns but also explain how ecosystems respond to climate changes and water resources, laying the groundwork for promoting vegetation productivity and ecological construction in water-stressed areas.

Numerous studies have shown that the variability of WUE is related to a variety of factors, including human activities (vegetation greenness) [13–15], climate factors [16,17], CO_2 fertilization and N deposition [18], canopy conductance [19], and drought [6]. In arid ecosystems, WUE variability is mostly influenced by human activity and climate factors [20–22]. For example, Bai et al. [21] found that WUE variations in the arid ecosystems of China were controlled by precipitation. Xu [22] suggested that precipitation promoted vegetation WUE in dryland regions of China. Du et al. [20] pointed out that WUE in northern China presented a dominant increasing trend and WUE variability was primarily controlled by climate factors (precipitation, temperature, and solar radiation), with climate accounting for 84% and human activities accounting for approximately 16%. Nevertheless, Guo et al. [5] found that human activities played a critical role in the increase of WUE in the Beijing–Tianjin Sandstorm Source region, with a relative contribution of 88.2%, followed by precipitation and temperature, which contributed only 11.8%. The impact of climate change and human activity on WUE in water-limited regions remains debatable.

Inner Mongolia is the third largest province and region in China (12.3% of China's land area); it has vast grassland resources and mineral resources, which are important for the ecological environment protection and economic growth of China [23–25]. However, located in arid and semi-arid environments, Inner Mongolia has a fragile ecological environment and uneven distribution of water resources, due to which, it is extremely sensitive to climate change [26–28]. With the country's rapid economic development and increasing level of urbanization, the water resources and terrestrial biodiversity of Inner Mongolia have seen a substantial decline in recent decades [23–25,29–33]. In response, the Chinese government has been implementing many large-scale ecosystem restoration and governance efforts since the 1950s. To use limited water resources sensibly and effectively, a more comprehensive and in-depth study of the WUE characteristics in water-limited areas is necessary. Therefore, this study selected Inner Mongolia as the study area and quantitatively assessed the variation characteristics of WUE and its response mechanism to human activity and climate change by combining climate data (temperature, precipitation, and solar radiation). The specific main objectives are: (1) to explore the spatiotemporal variations and trends of regional GPP, ET, and WUE; (2) to investigate the seasonal variations characteristics of GPP, ET, and WUE; (3) to depict the variations in GPP, ET, and WUE for different vegetation types and their contribution to IAV; (4) to determine the sensitivity and contribution of GPP and ET to WUE IAV; and (5) to evaluate the positive–negative effects of human activity and climate on variations in WUE. The findings are expected to provide a reference basis for future rational planning of vegetation restoration and water resource management.

2. Materials and Methods

2.1. Study Area

Inner Mongolia (Inner Mongolia Autonomous Region) is located on the northern border of China (37°24′–53°23′N, 97°12′–126°04′E) and it represents the third largest province and region in China, with an area of 118.3×10^4 km^2. Inner Mongolia belongs to a temperate continental climate with cold winters and hot summers. It has complex and diverse landforms, with the terrain inclining from southwest to northeast, sequentially covering

the Mu Us sandy land, Otindag sandy land, Horqin sandy land, and Da Hinggan Ling Mountains (Figure 1c). As an important animal husbandry production base in China, Inner Mongolia has rich and diverse vegetation types, with grassland being the most prevalent vegetation type, including meadow steppe, typical steppe, and desert steppe, which account for approximately 46.13% of the total area (Figure 1b).

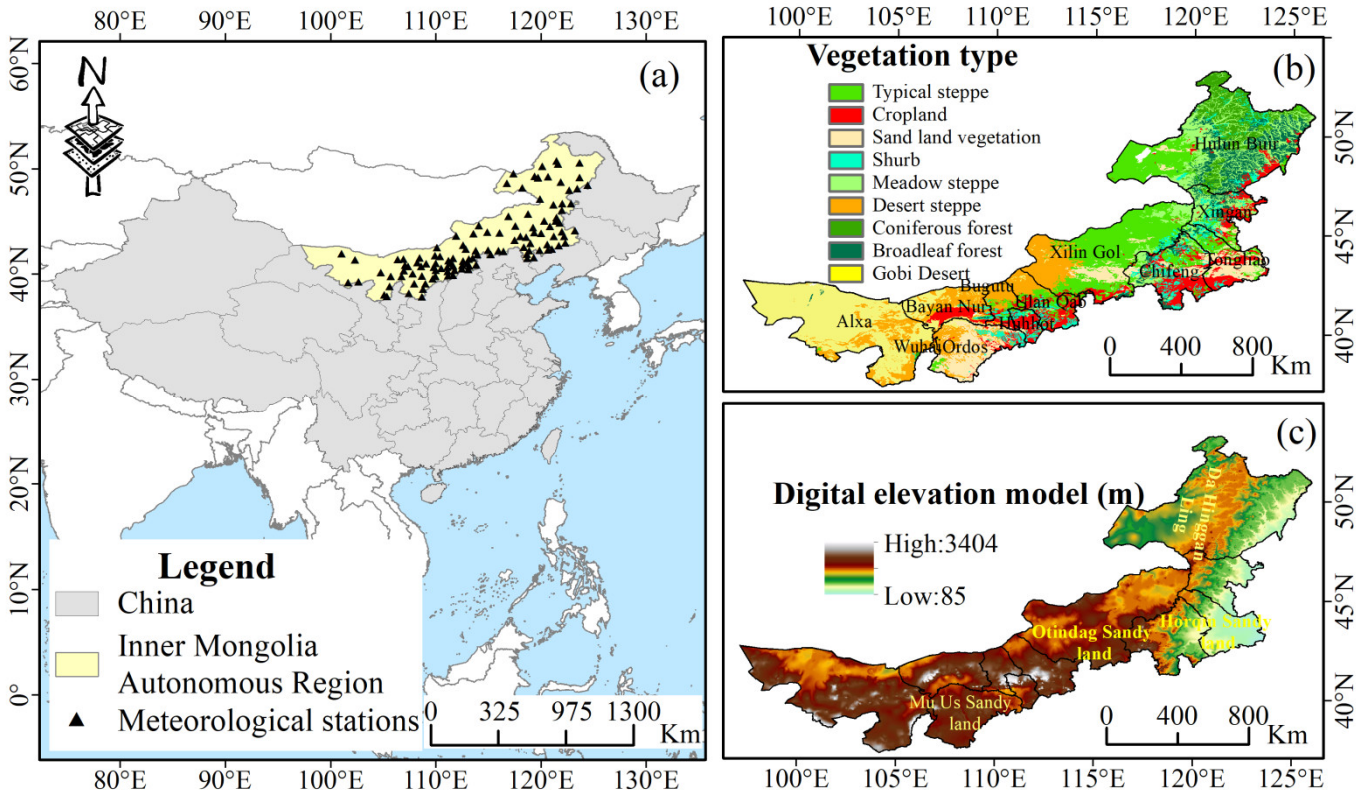

Figure 1. Overview of the study region, (**a**) Geographical location and meteorological stations, (**b**) Vegetation types, and (**c**) Digital elevation model (DEM).

2.2. Data Sources

In this study, the global OCO-2-based solar-induced chlorophyll fluorescence product (GOSIF) GPP and the Global Land Evaporation Amsterdam Model version 3.5a (GLEAM) ET remote sensing products were used to calculate WUE. GOSIF GPP (2001–2020) is a long-term series dataset based on solar-induced chlorophyll fluorescence (http://data.globalecology.unh.edu/, accessed on 15 May 2022), with a spatial resolution of 0.05°and 8-day time step [34]. GLEAM product ET is estimated from observed precipitation, surface soil moisture, and vegetation moisture content as the control conditions by using Priestley-Taylor algorithms and combining multi-source remote sensing data [35,36]. The GLEAM 3.5a datasets (https://www.gleam.eu/, accessed on 15 May 2022) span from 1981 to 2020, with a spatial of 0.25°and a daily time step. ET products were resampled to 0.05° to unify the spatial resolution of the ET and GPP products.

Meteorological datasets include daily temperature, precipitation, and sunshine hours data from the China Meteorological Data Network (http://data.cma.cn/, accessed on 15 May 2022). This network covers meteorological data from 118 stations in Inner Mongolia from 2001 to 2020, as shown in Figure 1a. Using the FAO Penman–Monteith formula, the sunshine hours were used to calculate solar radiation data [37]. These data were interpolated to a spatial resolution of 0.05° × 0.05 using the kriging interpolation method. Vegetation type data were derived from a 1:1000,000 raster map of vegetation type of Inner Mongolia with a spatial resolution of 0.0083°. In this map, the study area is divided into 9

vegetation types. In this study, the Gobi Desert was excluded because its vegetation was relatively sparse and some areas even had no vegetation cover.

Elevation Data (DEM) with a resolution of 90 m and land use/land cover data (2000, 2010, and 2020) with a resolution of 1 km were drawn from the Resource and Environmental Science Data Platform of the Chinese Academy of Sciences (https://www.resdc.cn/, accessed on 15 May 2022). The land use data mainly included 6 primary land use types (Cropland, Forest, Grassland, Water bodies, Built-up land, and Unused land), and 25 secondary land use types. Considering the characteristics of the wide distribution of grasslands in Inner Mongolia, the land cover types were reclassified into 9 categories, namely cropland, forest, high-coverage grassland, medium-coverage grassland, low-coverage grassland, water bodies, built-up land, sandy land, and unused land. The degree of land use dynamics was also calculated for each league or city during the study period. A single dynamic degree reflecting the change of a specific land use type was assessed in the study area through the study period. The specific calculation formula is available in Wang et al. [38].

2.3. Methods

2.3.1. Ecosystem Water Use Efficiency

WUE (gC m^{-2} mm^{-1}) is defined as the amount of carbon uptake per unit of water loss [39–41], whereas GPP (gC m^{-2} yr^{-1}) and ET (mm yr^{-1}) are frequently used to express carbon uptake and water loss at the ecosystem scale [17,42,43]:

$$\mathrm{WUE} = \frac{\mathrm{GPP}}{\mathrm{ET}} \tag{1}$$

2.3.2. Trend Analysis

The Theil–Sen median trend analysis is a non-parametric method for estimating time series trends, and it is immune to outliers [44,45]. The Mann–Kendall (M–K) test is a non-parametric method for assessing the significance of time series trends [46,47]. The two methods are often combined to determine the change trends of vegetation in time series data. The Theil–Sen median trend analysis is expressed as Equation (2):

$$\mathrm{Sen} = \mathrm{Median}\left(\frac{X_j - X_i}{j - i}\right) \tag{2}$$

Sen > 0 denotes an increasing trend in X; Conversely, it denotes a decreasing trend.

The Mann–Kendall test is expressed as Equation (3):

$$S = \sum_{i=1}^{n-1} \sum_{j=i+1}^{n} \mathrm{sgn}(X_j - X_i) \tag{3}$$

where, n is the time series length, $\mathbf{X_i}$ and $\mathbf{X_j}$ are the data values in the time series i and j (j > i), respectively. The $\mathbf{sgn}(\mathbf{x_j} - \mathbf{x_i})$ is calculated as Equation (4):

$$\mathrm{sgn}(X_j - X_i) = \begin{cases} +1, & \text{if } X_j - X_i > 0 \\ 0, & \text{if } X_j - X_i > 0 \\ -1, & \text{if } X_j - X_i > 0 \end{cases} \tag{4}$$

The standard normal test statistic Z is calculated using Equation (5):

$$Z = \begin{cases} \dfrac{S-1}{\sqrt{s(S)}}, S > 0 \\ 0, \quad S = 0 \\ \dfrac{S+1}{\sqrt{s(S)}}, S < 0 \end{cases}, s(S) = \frac{n(n-1)(2n+5)}{18} \tag{5}$$

in which, a positive or negative Z indicates an increase or decrease. $|\mathbf{z}| > \mathbf{1.96}$ indicates a significant increase (or decrease) in the time series at a confidence level of α = 0.05.

2.3.3. Calculating the Contribution of Interannual Variability (IAV)

The contribution of IAV of a grid cell or vegetation type j to regional WUE (GPP or ET) IAV is defined as [48]:

$$f_j = \frac{\sum_t \frac{x_{jt}|X_t|}{X_t}}{\sum_t |X_t|} \quad (6)$$

where, $\mathbf{x_{jt}}$ is the WUE anomaly (departure from a long-term trend) of j vegetation types in year t; $\mathbf{X_t}$ is the regional WUE anomaly, so that $\mathbf{X_t} = \sum_j \mathbf{x_{jt}}$. By this definition, $\mathbf{f_j}$ is the average relative anomaly $\mathbf{x_{jt}}/\mathbf{X_t}$ for regional j weighted with the absolute global anomaly $|\mathbf{X_t}|$.

2.3.4. Multiple Regression Residual Analysis

Residual analysis is the most popular method for investigating the different effects of climate and human activities on vegetation [49,50]. In this study, changes in WUE over the study period were hypothesized to be influenced solely by climate change and human activities. We established multiple regression models between WUE and climatic variables (temperature, precipitation, and solar radiation) for each pixel and evaluated them using F-statistics. WUE during the study period was then predicted using the multiple regression models to represent the influence of only climate change. The difference between the observed WUE (WUE_{obs}) and predicted WUE (WUE_{pv}) was then taken as the response of human activities on WUE, namely residual WUE (WUE_{RV}). The equations for calculating these values are as follows:

$$WUE_{PV} = a \times T + b \times P + c \times R + d \quad (7)$$

$$WUE_{RV} = WUE_{obs} - WUE_{PV} \quad (8)$$

where, P, T, and R represent precipitation, temperature, and solar radiation, respectively; and a, b, and c are regression coefficients of multiple linear regression, respectively. Based on the standards presented in Table 1, the main driving factors of variations in WUE were identified and the positive and negative effects of climate change and human activity on WUE were estimated.

Table 1. Standards for identifying the main drivers of WUE change and methods for calculating contribution rates.

Sen (WUE_{obs})	Driving Factors	Driver Division Standard		The Contribution Rate of Drivers (%)	
		Sen(WUE_{PV})	Sen(WUE_{RV})	Climate Change	Human Activity
>0	PV&RV	>0	>0	$\frac{Sen(WUE_{PV})}{Sen(WUE_{obs})}$	$\frac{Sen(WUE_{RV})}{Sen(WUE_{obs})}$
	PV	>0	<0	100	0
	RV	<0	>0	0	100
<0	PV&RV	<0	<0	$\frac{Sen(WUE_{PV})}{Sen(WUE_{obs})}$	$\frac{Sen(WUE_{RV})}{Sen(WUE_{obs})}$
	PV	<0	>0	100	0
	RV	>0	<0	0	100

2.3.5. Relative Contribution Statistical Method

Multiple regression linear models have been developed between multiple independent and dependent variables to assess the degree to which the various independent variables explained the dependent variable [17,51,52]. This method computes the linear relationship between independent and dependent variables and employs standard regression coefficients to express the sensitivity of the independent variable to the dependent variable [17,52]. The ratio of the absolute value of the regression coefficient of each variable to the sum of the absolute values of all regression coefficients can be used to calculate the relative contribution rate of an independent variable to the dependent variable [51].

3. Results

3.1. Spatial and Temporal Variations in GPP, ET, and WUE

Regarding the interannual variations of GPP, ET, and WUE in Inner Mongolia from 2001 to 2020 (Figure 2), regional GPP showed a significant increasing trend (6.28 gC m^{-2} yr^{-1} a^{-1}, $p < 0.01$), with a mean of 481.51 gC m^{-2} yr^{-1}. The lowest and highest GPP were observed in 2001 (412.26 gC m^{-2} yr^{-1}) and 2018 (561.38 gC m^{-2} yr^{-1}), respectively. ET also showed a significant increasing trend (2.70 mm yr^{-1} a^{-1}, $p < 0.01$), with a mean of 327.77 mm yr^{-1}, but its increasing trend was significantly smaller than that of GPP. The lowest and highest ET were observed in 2008 (290.87 mm yr^{-1}) and 2015 (371.18 mm yr^{-1}), respectively. Under the combined action of GPP and ET, regional WUE also showed a significant increasing trend (0.006 gC m^{-2} yr^{-1} a^{-1}, $p < 0.01$), and annual WUE ranged between 1.16 and 1.60 gC m^{-2} mm^{-1}, with a mean of 1.35 gC m^{-2} mm^{-1}. Its interannual values fluctuated widely from 2001 to 2020, with the lowest and highest values in 2001 (1.16 gC m^{-2} mm^{-1}) and 2018 (1.60 gC m^{-2} mm^{-1}), respectively.

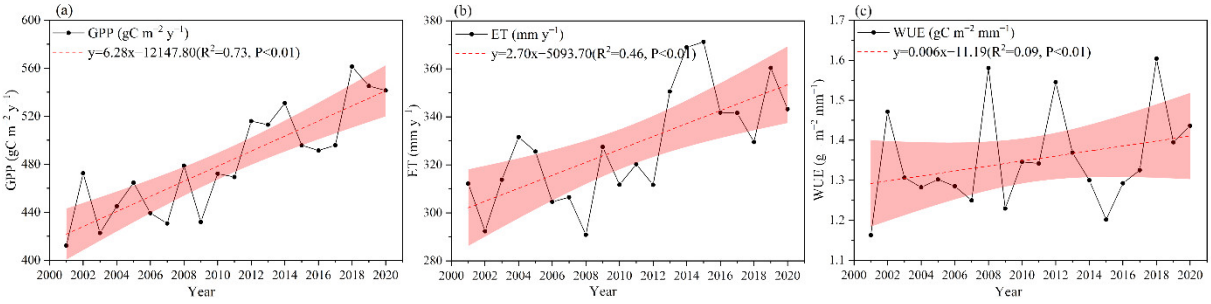

Figure 2. Interannual variations of (**a**) GPP, (**b**) ET, and (**c**) WUE in Inner Mongolia from 2001 to 2020 (The red shades highlight the 95% confidence interval. The black lines are time series of regional annual GPP, ET, and WUE, while the red dashed lines represent the trend).

As shown in Figure 3, WUE and GPP exhibited similar spatial patterns, the higher values in the northeast and lower values in the southwest. In contrast, ET exhibited a spatial pattern of decreasing from east to west and south to north. From the spatial distribution of their trends (Figure 3), GPP, ET, and WUE all exhibited an increasing trend. Regarding GPP, approximately 96.39% of the pixels showed an increasing trend, of which, areas with significant increase accounted for 48.89% of all pixels, mainly distributed in the eastern regions and Mu Us sandy land in the southwest. Regarding ET, approximately 87.97% of the pixels showed an increasing trend, and areas with significant increases accounted for 39.91% of the total pixels and appeared in the central and eastern parts of the study area. Nevertheless, 12.03% of the area showed a slight decrease, scattered in the northeast and western parts. The WUE statistics show that the increase and decrease trends accounted for 70% and 30%, of which, areas with significant increase and decrease accounted for approximately 22.35% and 2.63% of all pixels. Areas with significant increases were mainly located in the Horqin sandy land in the southeast and the Mu Us sandy land in the southwest, whereas areas with significant and slight decreases were

concentrated in the central part of Xilin Gol league and the Da Hinggan Ling Mountains in the northeast.

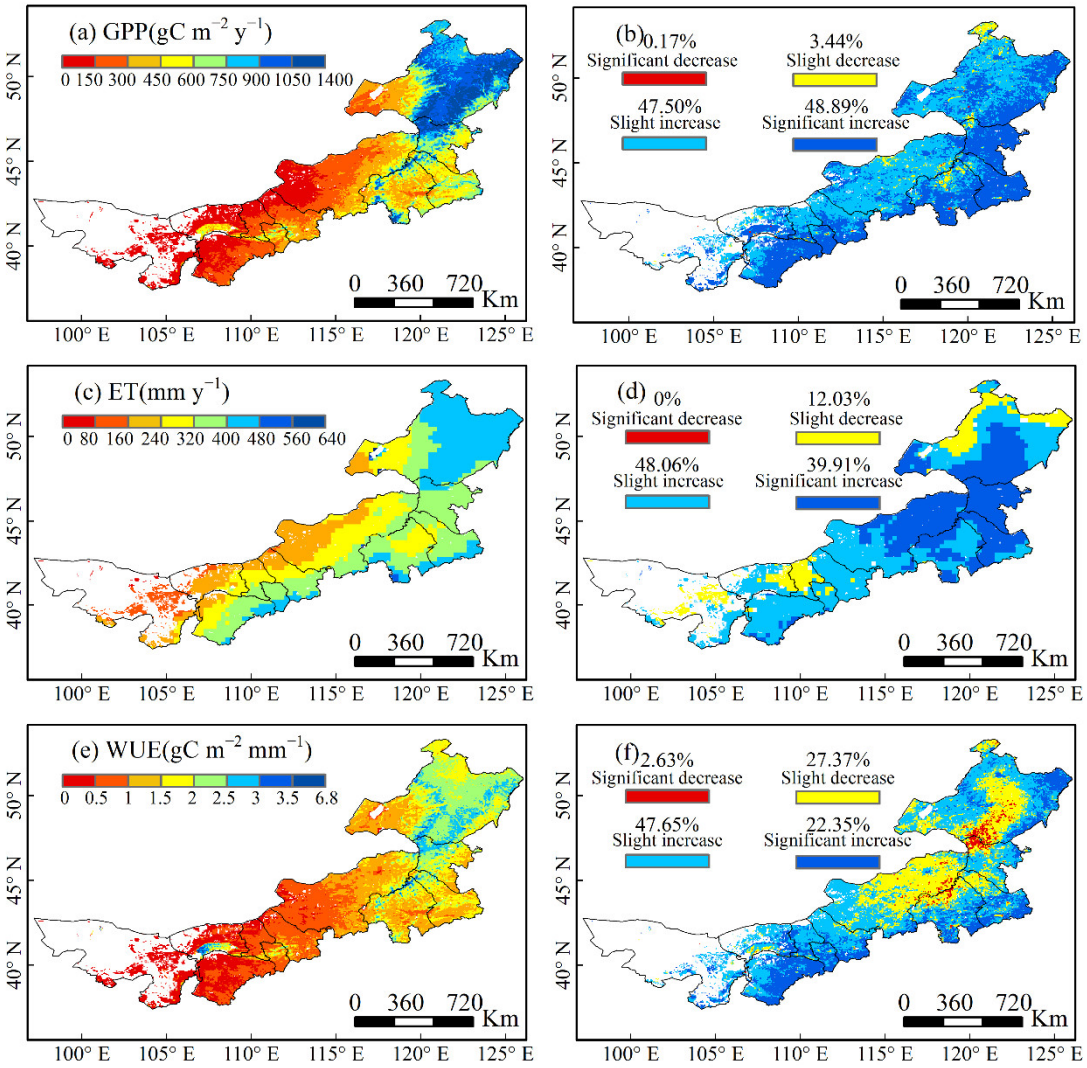

Figure 3. Spatial differences of annual average (**a**) GPP, (**c**) ET, (**e**) WUE, and (**b**,**d**,**f**) their trends (significance levels of 0.05) in Inner Mongolia from 2001 to 2020.

3.2. Seasonal Characteristics of GPP, ET, and WUE

WUE exhibited a generally consistent spatial pattern across the four seasons, with higher values in the northeast and lower values in the southwest (Figure S1). The seasonal WUE values in Inner Mongolia exhibited the overall characteristics of summer > autumn > winter > spring (Figure 4). Among the four seasons, the highest mean value (1.77 gC m^{-2} mm^{-1}) was observed in summer (June–August), with minimum and maximum values of 0.02 and 6.89 gC m^{-2} mm^{-1}, respectively. The mean WUE values in autumn (September–November) and winter (December–February) were 1.36 gC m^{-2} mm^{-1} and 0.78 gC m^{-2} mm^{-1}, respectively. More specifically, 50% of WUE values in autumn were primarily concentrated between 0.89 and 1.71 gC m^{-2} mm^{-1}, while 50% of WUE values in winter were primarily concentrated between 0.16 and 1.18 gC m^{-2} mm^{-1}. However, the lowest mean WUE value was observed in spring (March-May) at 0.40 gC m^{-2} mm^{-1}, with minimum and maximum values of 0 to 2.24 gC m^{-2} mm^{-1}, respectively. For GPP, the highest mean value was observed in summer, with a value of 353.82 gC m^{-2} yr^{-1}, the 50% of GPP values in summer were primarily concentrated between 131.39 and 562.15 gC m^{-2} yr^{-1}. Whereas, the

lowest mean GPP was observed in winter (20.09 gC m^{-2} yr^{-1}), and 50% of GPP values in winter were primarily concentrated between 11.60 and 25.65 gC m^{-2} yr^{-1}. The seasonal GPP values showed the characteristics of summer > autumn > spring > winter. The mean ET was the highest in summer (176.28 mm yr^{-1}), the 50% of ET values in summer were primarily concentrated between 142.44 and 213.74 mm yr^{-1}, respectively. Followed by spring and autumn, with mean values of 81.89 mm yr^{-1} and 62.11 mm yr^{-1}, respectively. For spring and autumn, 50% of ET values in spring were primarily concentrated between 61.29 and 105.86 mm yr^{-1}, while 50% of ET values in autumn were primarily concentrated between 50.13 and 73.49 mm yr^{-1}. The lowest mean ET was observed in winter at 20.84 mm yr^{-1}, with minimum and maximum values of 0 and 44.88 mm yr^{-1}, respectively.

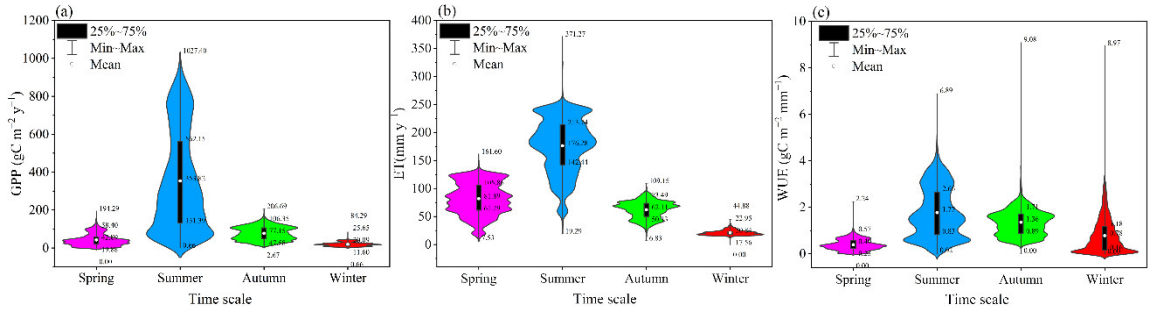

Figure 4. Mean values of (**a**) GPP, (**b**) ET, and (**c**)WUE in various seasons in Inner Mongolia.

3.3. Contribution of Each Vegetation Type to GPP, ET, and WUE IAV

The primary vegetation types in Inner Mongolia are coniferous forests (6.23%), broadleaf forests (7.75%), meadow steppe (12.77%), typical steppe (23.36%), desert steppe (17.97%), shrubs (6.85%), cropland (13.76%), and sand land vegetation (11.31%). The annual average values of GPP, ET, and WUE for different vegetation types are presented in Figure 5. The relatively highest GPP values were found in broadleaf forests, coniferous forests, and meadow steppe in the study area, with values exceeding 800 gC m^{-2} yr^{-1}. Among them, broadleaf forests showed the highest value, with a mean of 938.36 gC m^{-2} yr^{-1}, followed by coniferous forests, meadow steppe, shrubs, cropland, typical steppe, and sand land vegetation. On the contrary, the desert steppe showed the lowest GPP (94.42 gC m^{-2} yr^{-1}). Regarding ET, coniferous forests showed the highest value at 439.74 mm yr^{-1}, followed by broadleaf forests, meadow steppe, shrubs, cropland, sand land vegetation, and typical steppe, with their average values exceeding 290 mm yr^{-1}, while desert steppe showed the lowest value at 204.26 mm yr^{-1}. Broadleaf forests showed the highest WUE value, with an average of 2.26 gC m^{-2} mm^{-1}, while desert steppe showed the lowest WUE value at 0.46 gC m^{-2} mm^{-1}. The mean values of WUE for different vegetation types followed the order: broadleaf forest > coniferous forest > meadow steppe > shrub > cropland > typical steppe > sand land vegetation > desert steppe.

Figure 5 depicts the contribution of each vegetation type to GPP, ET, and WUE IAV. The contribution of each vegetation type to GPP, ET, and WUE IAV showed some variability. We discovered that typical steppe contributed the most (169.89%) to GPP IAV from 2001 to 2020, followed by cropland ecosystem (164.18%), and they are mostly found in the southeast and western rivers regions. The area of the shrub only accounts for 6.85% of the total area, but they make a great contribution to GPP IAV in arid and semi-arid zones, with a value of 143.69%. The broadleaf forest and sand land vegetation contributed 75.35% and 71.57% to GPP IAV, respectively. The desert steppe ecosystems cover far more area than shrubs and sand land vegetation, but they contributed only 31.51%. Among all vegetation types, only coniferous forest ecosystems contribute negatively to GPP IAV, with a value of −36.28%. The typical steppe contributed the most (141.09%) to ET IAV and was primarily distributed in the western Hulun Buir and Xilin Gol regions. The desert steppe

ecosystems were the second largest contribution to ET IAV (129.70%), followed by cropland (117.87%), shrubs (113.44%), and sand land vegetation (107.94%). By contrast, the meadow steppe, broadleaf forest, and coniferous forest ecosystems contributed the least to ET IAV, with a value of 48.70%, 37.15%, and 28.20%, respectively. More importantly, we found that typical steppe accounts for the largest fraction (193.42%) of the WUE IAV over this period, followed by cropland ecosystems contributed 106.85%. The desert steppe, shrubs, sand land vegetation, meadow steppe, and broadleaf forest ecosystems contributed to WUE IAV with 102.25%, 92.99%, 74.95%, 72.42%, and 27.27%, respectively. In contrast, we found that coniferous forest ecosystems account for the lowest fraction of the WUE IAV at −32.86%. In addtion, the WUE exhibits significant fluctuation at each vegetation type, with typical steppe anomalies being the greatest compared to other vegetation types. While desert steppe anomalies are more volatile for ET, coniferous forest anomalies are more prominent for GPP (Figure 6).

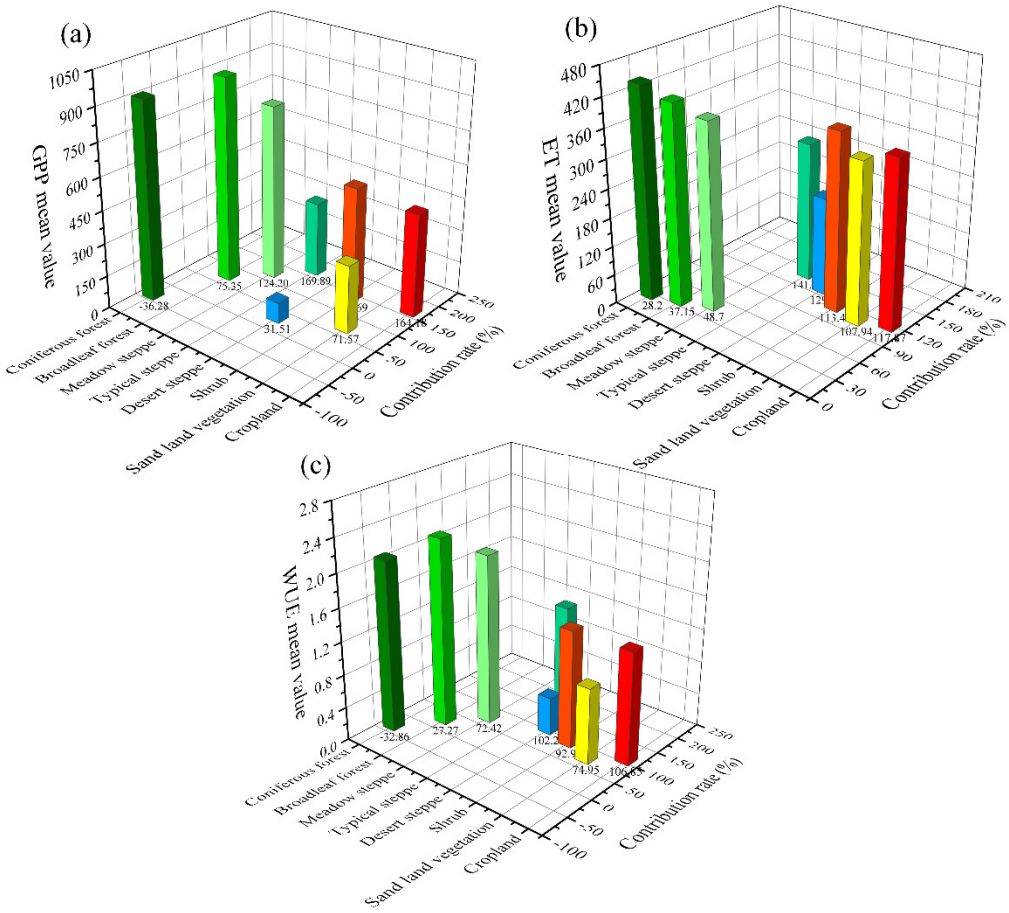

Figure 5. The mean values of each vegetation type and their contribution to (**a**) GPP, (**b**) ET, and (**c**) WUE IAV in Inner Mongolia from 2001 to 2020.

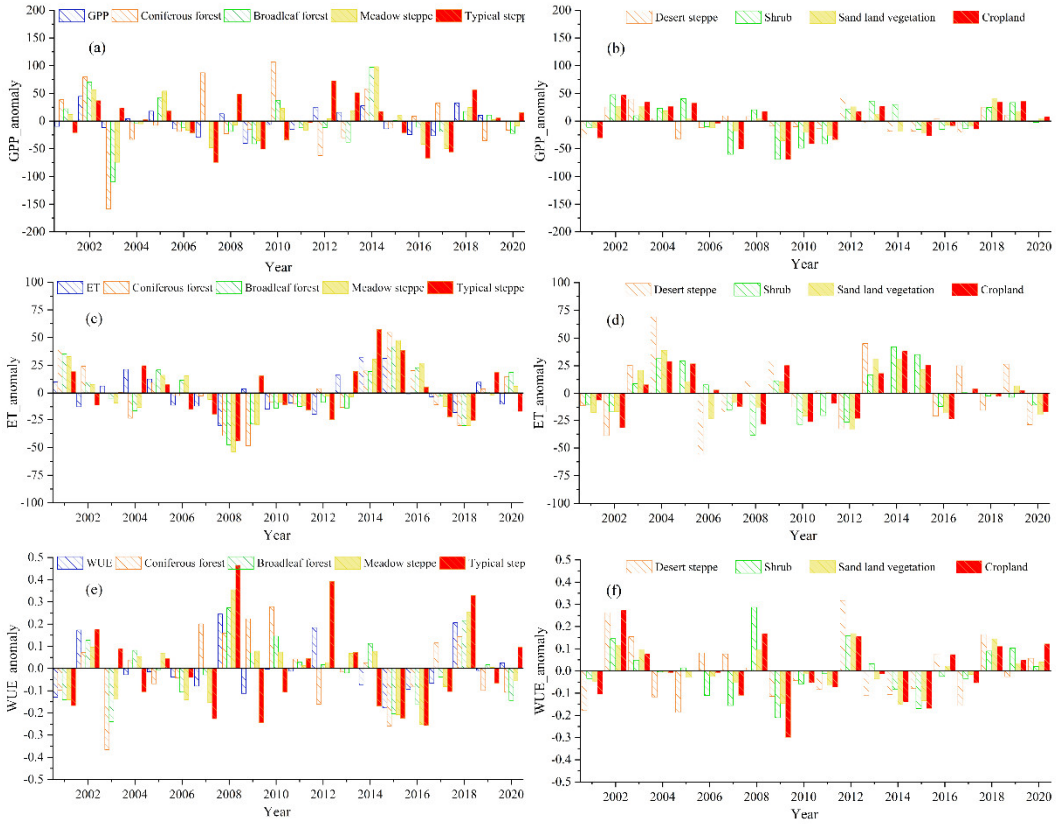

Figure 6. The anomaly of GPP, ET, and WUE for different vegetation types from 2001 to 2020; (**a**,**b**) GPP, (**c**,**d**) ET, and (**e**,**f**) WUE.

3.4. Contributions and Sensitivity of GPP and ET to WUE

Variations in WUE are mainly attributed to changes in GPP and ET. Figure 7 shows the spatial patterns of the sensitivity coefficients of GPP and ET on WUE variations, with each pixel significant at the 0.05 significance level in F-statistics. A positive (negative) sensitivity coefficient shows that WUE increases (decreases) as GPP (ET) increases. WUE showed a sensitivity coefficient of 0.866 for GPP, with higher sensitivity in the eastern and southwestern regions. The sensitivity of WUE to ET was −0.606, with high sensitivity in the Da Hinggan Ling Mountains and low sensitivity in the western region. As shown in Figure 8c, the change in WUE in Inner Mongolia from 2001 to 2020 is mainly driven by GPP. The contribution of GPP to WUE was 59.36%, accounting for 83.82% of all pixels, widely distributed in most of the central and western parts of Inner Mongolia. The contribution of ET to WUE was 40.64%, accounting for 16.18% of the total pixels, mainly distributed in the Da Hinggan Ling Mountains in the northeast, the northern part of the Horqin sandy land, and the northern part of the Mu Us sandy land (Figure 8a,b). Figure 8 shows the spatial patterns of the relative contributions of GPP and ET to WUE variations, it exhibited opposite spatial pattern characteristics. Areas with a high contribution of GPP (>60%) were widely distributed in the central and western regions, accounting for 49.47% of the total pixels, whereas areas with a low contribution of GPP (<40%) were scattered in the north of the Mu Us sandy land and the south foot of the Da Hinggan Ling Mountains, accounting for 3.06% of the total pixels. Areas with a high contribution of ET (>60%) accounted for 3.06% of the total pixels, while areas with a low contribution of ET (<40%) accounted for 49.47% of the total area.

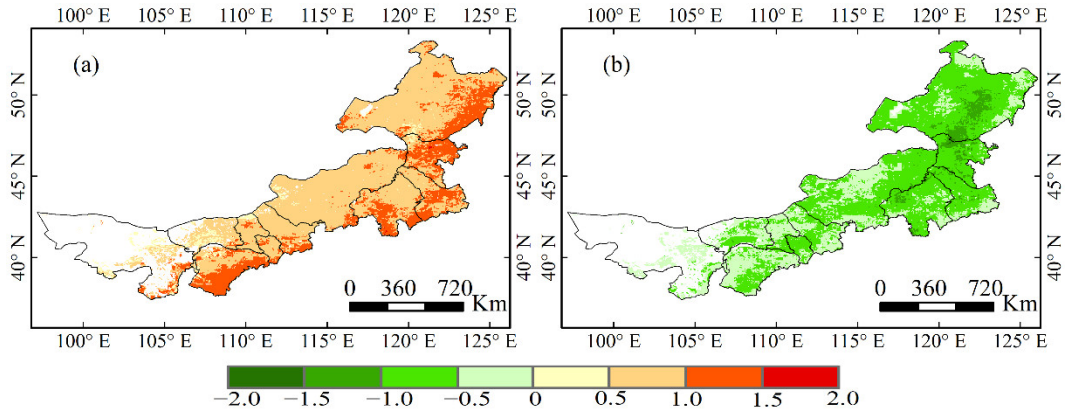

Figure 7. Spatial distribution of sensitivity coefficients of (**a**) GPP and (**b**) ET to WUE in Inner Mongolia.

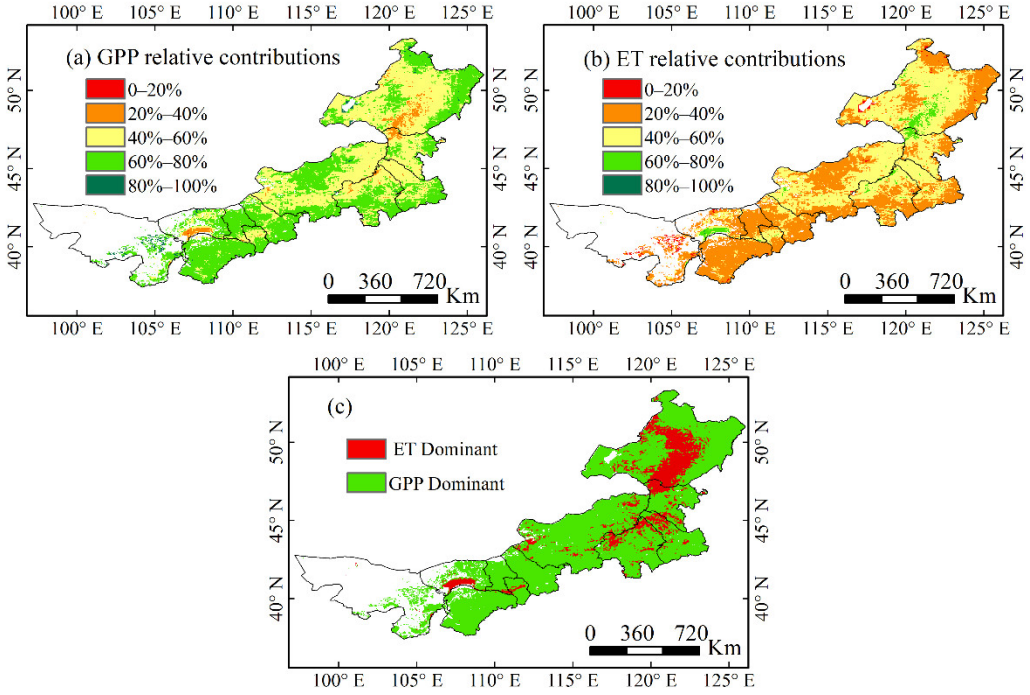

Figure 8. Spatial pattern of relative contributions of (**a**) GPP and (**b**) ET to WUE in Inner Mongolia from 2001 to 2020; (**c**) Spatial distributions of dominant controlling factors (i.e., GPP or ET).

3.5. Drivers of WUE Variability

Figure 9 shows the negative and positive contributions of human activity and climate change to WUE in Inner Mongolia from 2001 to 2020. The result shows that human activities are the main driving factor of WUE changes in Inner Mongolia from 2001 to 2020, with human activities and climate contributing to 53.52% and 46.46%, respectively. Human activity exhibited positive effects on WUE in approximately 70.34% of the pixels, dispersed in central Xilin Gol, Hohhot, Bugutu, eastern Bayan Nur, eastern Ordos, and eastern and western Hulun Buir. Nevertheless, human activities showed minor negative effects in approximately 29.66% of the pixels, mainly focused on the Da Hinggan Ling Mountains, Horqin sandy land, Otindag sandy land, and western Mu Us sandy land. Among them, areas with a negative contribution of less than 75% (2.45%) were scattered in the south foot of the Da Hinggan Ling Mountains. Areas with positive and negative contributions of climate change to WUE accounted for 68.20% and 31.80% of the total pixels, respectively. Areas with positive contributions are widely spread in the eastern and

western foot of the Da Hinggan Ling Mountains, the Horqin sandy land, the Otindag sandy land, and the western regions. Areas with negative contribution were located in central Xilin Gol, northern Chifeng, northern Tongliao, and the Da Hinggan Ling Mountains. In particular, areas with negative contributions exceeding 75% accounted for 2.34% of the entire study area, mainly concentrated in the Da Hinggan Ling Mountains.

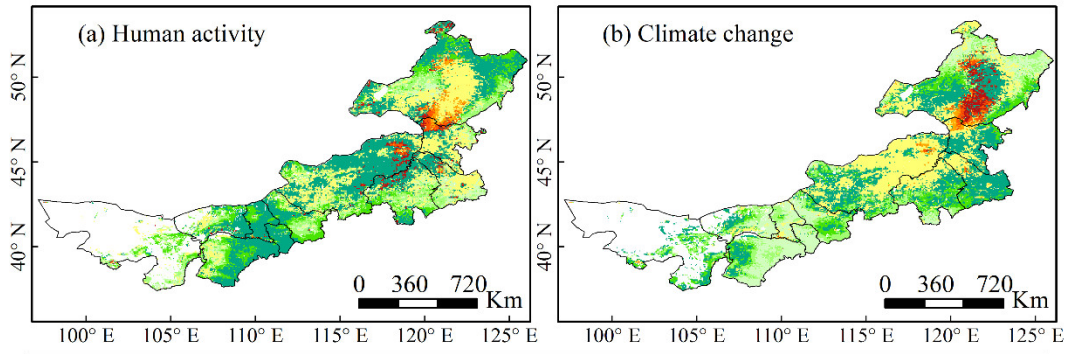

Contribution rate(%)	Pixel percentage (%)							
	−100 ~ −75	−75 ~ −50	−50 ~ −25	−25 ~ 0	0 ~ 25	25 ~ 50	50 ~75	75 ~ 100
Human activity	2.45	1.63	1.62	23.96	8.12	11.64	12.34	38.24
Climate change	2.34	1.62	1.63	25.78	14.91	12.34	11.65	29.3

Figure 9. Spatial distribution of positive and negative contributions of human activity and climate change on variations in WUE from 2001 to 2020.

Figure 10 shows the spatial pattern of sensitivity coefficients between WUE and climate factors in Inner Mongolia from 2001 to 2020. The results show that WUE is more sensitive to precipitation than other climatic variables. The sensitivity coefficient of WUE to precipitation was 0.345 ± 0.325, with high sensitivity in the western region and low sensitivity in the Da Hinggan Ling Mountains. With positive sensitivity coefficient in most areas except northeast regions, with a value of 0.447, accounted for 85.88% of the areas, indicating that WUE increases with increasing precipitation. 14.12% of regions showed a negatively sensitive (−0.276, Figure 10a) between WUE and precipitation, and it is primarily observed in the Da Hinggan Ling Mountains. According to Figure 10b, when precipitation is less than 400 mm, the WUE of Inner Mongolia increases with an increase of precipitation. However, when precipitation exceeds 400 mm, the sensitivity of the WUE to precipitation decreases. The temperature was the second most important climate factor influencing WUE and it mainly exhibited a negative sensitivity, with a value of −0.025 ± 0.217. Spatially, WUE was negatively sensitive to temperature in approximately 52.76% of regions (−0.189, Figure 10c), these negative sensitivity regions existed in the central and eastern parts of Inner Mongolia, indicating that the increase of temperature would decrease WUE. Furthermore, the high negative sensitivity coefficients areas located in the Otindag sandy land. A total of 47.24% of regions showed a positive sensitivity (0.159, Figure 10c) between WUE and temperature, which was mainly distributed in the northeast, southeast, and southwest part of the region. In addition, the sensitivity coefficient is predominantly positive when the temperature > 6°C (Figure 10d), indicating that temperatures above 6°C are advantageous for the exchange of water and carbon in vegetation, and it is predominantly negative when the temperature< 6°C, indicating that temperatures below 6°C are unfavorable for the exchange of water and carbon. The mostly positive sensitivity of WUE to solar radiation, with a value of 0.019 ± 0.231. More than 53.99% of regions showed a positive sensitivity between WUE and solar radiation (0.194, Figure 10e), which is mainly distributed in the northeast, southeast, and southwest part of the region. Areas

with a negative sensitivity between WUE and solar radiation accounted for 46.01% of total pixels (−0.186, Figure 10e), with the majority of these pixels located in the central and eastern parts of Inner Mongolia. The high negative sensitivity coefficient was found in the Otindag sandy land, indicating that WUE decreased as solar radiation increased.

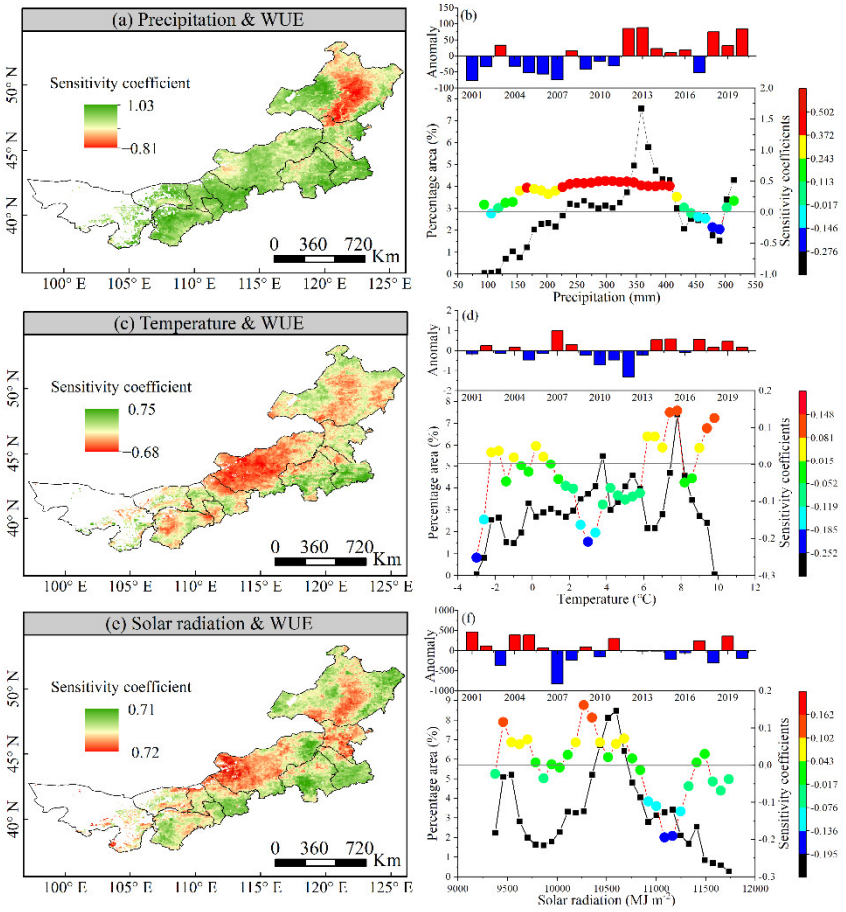

Figure 10. Sensitivity coefficient and their gradient change between WUE and climate factors in Inner Mongolia from 2001 to 2020. (**a**,**b**) Precipitation, (**c**,**d**) Temperature, and (**e**,**f**) Solar radiation.

The sensitivity coefficients of various vegetation types toward precipitation were ranked from largest to smallest: sand land vegetation, cropland, desert steppe, typical steppe, shrub, meadow steppe, coniferous forest, and broadleaf forest, and all of them were positive except for coniferous forest, indicating that the vegetation WUE increased as precipitation increased. The sensitivity of desert steppe to temperature was highest, at a value of −0.107 ± 0.242. The sensitivity coefficients of broadleaf forest, meadow steppe, typical steppe, and desert steppe are all negative values, while coniferous forest, shrub and sand land vegetation, and cropland are all positive values. In addition, all vegetation types were positively sensitive to solar radiation except for coniferous forests and desert steppe. Of these, the desert steppe, cropland, and shrub ecosystems were more sensitive to solar radiation, with values of −0.134 ± 0.233, 0.116 ± 0.214, and 0.114 ± 0.212, respectively (Table 2).

Table 2. Sensitivity of WUE to climate change for different vegetation types in Inner Mongolia.

Vegetation Types	Precipitation	Temperature	Solar Radiation
Coniferous forest	−0.121 ± 0.290	0.009 ± 0.174	−0.023 ± 0.207
Broadleaf forest	0.046 ± 0.370	−0.035 ± 0.151	0.029 ± 0.232
Meadow steppe	0.197 ± 0.379	−0.005 ± 0.171	0.034 ± 0.231
Typical steppe	0.439 ± 0.192	−0.106 ± 0.223	0.004 ± 0.209
Desert steppe	0.450 ± 0.222	−0.107 ± 0.242	−0.134 ± 0.233
Shrub	0.398 ± 0.262	0.058 ± 0.178	0.114 ± 0.212
Sand land vegetation	0.515 ± 0.180	0.025 ± 0.245	0.071 ± 0.205
Cropland	0.497 ± 0.226	0.075 ± 0.192	0.116 ± 0.214
Entire region	0.345 ± 0.325	−0.025 ± 0.217	0.019 ± 0.231

4. Discussion

4.1. Evaluation of GPP, ET, and WUE

Changes in WUE in ecosystems have been explored using various methods at various spatial scales, including field control experiments, eddy covariance, isotope observation techniques, process-based models, and remote sensing products [13,17,53]. In this study, the long-term series datasets of GOSIF GPP and the GLEAM ET products were used. Many studies found that GOSIF GPP products have good performance in monitoring carbon sinks at regional and global scales [34,54]. Meanwhile, numerous studies have confirmed that GLEAM ET is highly applicable to various ecosystems, particularly grassland ecosystems in arid and semi-arid regions [36,55–57]. Therefore, the estimation of WUE in Inner Mongolia using GOSIF GPP and GLEAM ET products has certain reliability.

4.2. Variations of WUE

Our analysis showed that the WUE exhibited a decreasing trend from northeast to southwest, which is consistent with the previous research results [15,58]. The WUE of vegetation in Inner Mongolia showed some seasonal variability. Among the four seasons, the highest WUE was observed in summer, followed by autumn and winter, while the lowest WUE was observed in spring (Figure 6), which is inconsistent with the findings of Sun et al. [59], who discovered that WUE is the highest in summer, followed by autumn, spring, and winter. These findings were most likely attributable to the seasonal differences in GPP and ET. Seasonal GPP values followed the order summer > autumn > spring > winter. Seasonal ET values followed the order summer > spring > autumn > winter. As the temperature rises in spring, snow or ice covering the land surface begins to melt, resulting in a significantly higher ET in spring than in autumn and winter [52]. In the meantime, vegetation would only be in the green-up stage in spring, with lower productivity [60]. Therefore, ET would have a significantly stronger effect than GPP, thus leading to the lowest WUE in spring.

The mean values of GPP, ET, and WUE differed across various ecosystems. Our analysis shows that the broadleaf forest and coniferous forest had higher mean values of GPP, ET, and WUE than other vegetation types, but their contributions to GPP, ET, and WUE IAV were generally lower than those of typical steppe. This may be attributed to physiological properties, area proportion, and survival environment condition of vegetation types. The typical steppe contributes the most to GPP, ET, and WUE IAV in arid and semi-arid regions, which indicates that typical steppe ecosystems play an important role in arid and semi-arid ecosystems. The typical steppe in the study area is vast (23.36%), with relatively dense vegetation that allows for greater photosynthesis and efficient water exchange [58,61], which has resulted in the highest contribution to GPP, ET, and WUE IAV. Cropland was the second most important contributor to WUE IAV. The rational use of irrigation and fertilization techniques, as well as the advancement of tillage techniques and crop types, all contribute to a significant increase of greening (GPP), which aids in the

improvement of WUE on cropland [62,63]. By contrast, the typical steppe ecosystem is more efficient than the forest at enhancing the use of water by vegetated ecosystems in arid and semi-arid zones.

In addition, WUE variations in Inner Mongolia were found to be mainly controlled by GPP (accounting for 83.82% of all pixels) and spread in the central and western regions; this finding agrees with that of Bai et al. [21] and Xue et al. [61]. However, Yang et al. [64] and Liu et al. [7] noted that GPP dominated WUE variations in humid regions, while ET dominated WUE variations in arid regions. This discrepancy could be attributed to the differences in analysis methods.

4.3. Response Mechanism of WUE to Human Activities and Climate Change

This study found that human activities are the primary drivers of WUE changes in Inner Mongolia, and their positive effects are stronger than their negative effects, which is consistent with previous findings [5,15]. Human activities induce an increase of WUE by increasing vegetation greenness through altered land cover [5]. The Chinese government has been implementing several large-scale ecological restoration projects since 2000, including the Grain for Green Project (since 1999), the Three Norths Shelter Forest Program (since 1978), and Grassland Ecological Protection Subsidy and Reward Policies (since 2010), all with the goal of restoring degraded ecosystem services by increasing vegetation greenness [32,65,66]. Driven by ecological restoration policies, positive changes have occurred in the forms of land cover. Figure 11 shows the Sankey diagram of land use transformations in Inner Mongolia from 2000 to 2020, the most dramatic transfer of land use mainly occurred in high-coverage grassland, medium-coverage grassland, and cropland, followed by forest, low-coverage grassland, and unused land. In particular, high-coverage grassland was largely converted into forest, medium-coverage grassland into high-coverage grassland, and cropland into high-coverage grassland. Furthermore, the transitions from forest to high-coverage grassland, low-coverage grassland to high-coverage grassland, and unused land to medium-coverage and high-coverage grassland were the most extensive. In general, high-coverage grassland and forest areas have increased in Inner Mongolia, and sandy land has decreased. Although the area of low-coverage grassland has slightly expanded, it is still much smaller than the increase of the area of high-coverage grassland and forest (Table S1). Therefore, the positive effects of human activities exceed the negative effects. Nevertheless, human activities have also negatively affected WUE changes in the Da Hinggan Ling Mountains in the northeast, the Horqin sandy land, and the western part of the Mu Us sandy land. The degree of land use dynamics for individual land use types confirmed that urban development and built-up land expansion are relatively serious in Hulun Buir, Xingan, Tongliao, Chifeng, and Xilin Gol (Figures 12 and S2), which has greatly reduced the green area of the land surface, leading to decreases in WUE [67]. Therefore, environmental protection and rational land use planning should be strengthened in these areas.

The influence of climate factors on WUE is caused by changes in GPP and ET [15,68]. Precipitation was found to be the dominant climate factor regulating WUE variability in Inner Mongolia. The sensitivity between WUE and precipitation was mostly positive, indicating that the increase of precipitation promotes the increase of vegetation WUE, which agrees with the previous findings [21,69]. Located in arid and semi-arid regions, vegetation growth in Inner Mongolia is primarily limited by insufficient water supply, and precipitation is an important source of water for vegetation growth [21]. An increase of precipitation would increase GPP beyond the increase of ET, thus resulting in an increase of WUE [16]. Good consistency was found in the sensitivity of WUE with solar radiation and temperature (Figure 10b,c). Negative sensitivity coefficients were observed in the Xilin Gol and the Da Hinggan Ling Mountains. A decline of WUE in these regions may be attributed to higher temperatures and increased solar radiation, leading to an increase of ET greater than of GPP [59,70]. Furthermore, the decline of WUE in Xilin Gol could be attributed to the negative effects of climate change, while the decline of WUE in the Da

Hinggan Ling Mountains could be attributed to the common inhibition effects of human activity and climate change.

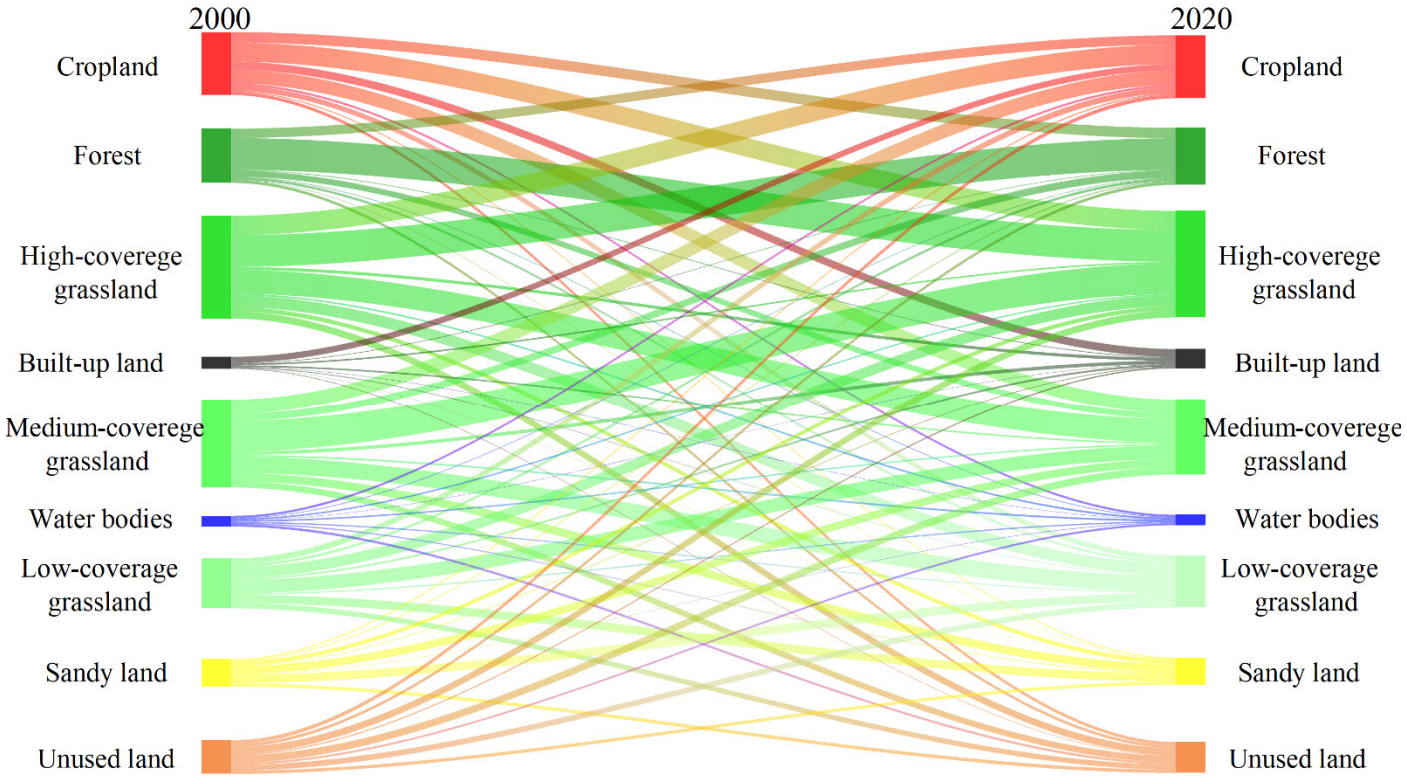

Figure 11. Sankey maps of land use transformations in Inner Mongolia from 2000 to 2020.

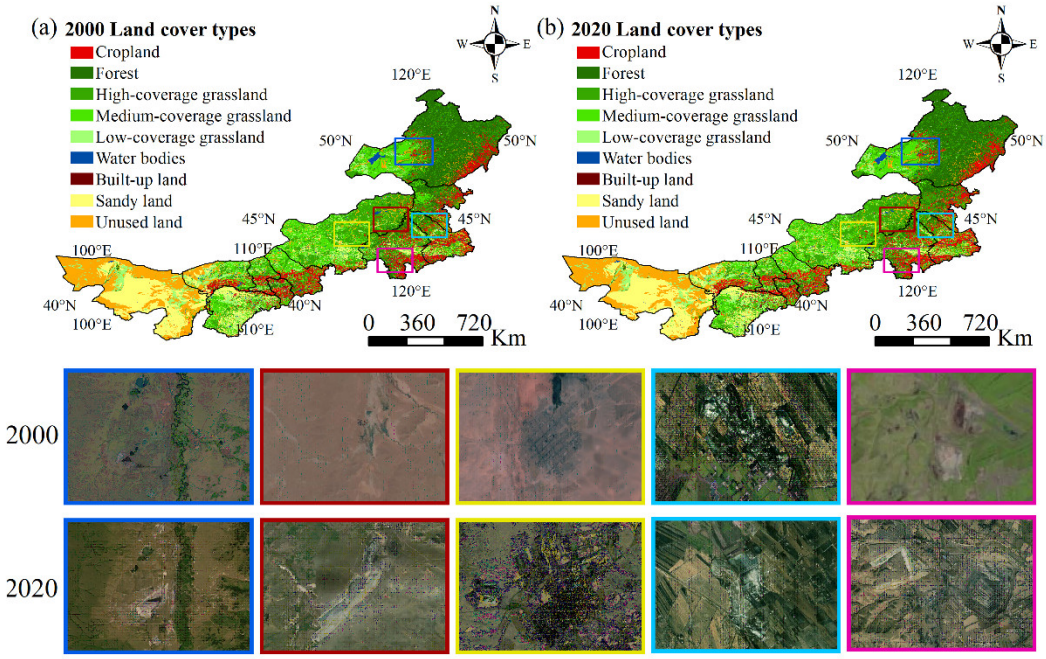

Figure 12. Land use spatial change maps for each league or city in Inner Mongolia from 2000 to 2020.

5. Conclusions

WUE is a crucial indicator of the relationship between terrestrial carbon and water cycles, as well as an effective variable reflecting the response of productivity to water availability. This study adopted remote sensing data and meteorological data to examine variation characteristics of WUE and its response mechanism to human activity and climate change. The main findings can be summarized as follows:

(1) The interannual change of GPP, ET, and WUE all showed significant increasing trends, with GPP showing a significantly larger increase than ET and WUE. Spatially, GPP, ET, and WUE showed an increasing trend. WUE showed increasing and decreasing trends in approximately 70% (22.35%) and 30% (2.63%) of the study area, respectively. Areas with significant increases were mainly distributed in the Horqin sandy land and the Mu Us sandy land, while areas with significant and slight decreases were concentrated in the central part of the Xilin Gol league and the Da Hinggan Ling Mountains in the northeast.

(2) The seasonal WUE values followed the order summer (1.77 gC m^{-2} mm^{-1}) > autumn (1.36 gC m^{-2} mm^{-1}) > winter (0.78 gC m^{-2} mm^{-1}) > spring (0.40 gC m^{-2} mm^{-1}). This phenomenon may be related to seasonal differences in GPP and ET.

(3) The mean values of GPP, ET, and WUE were higher in the broadleaf forest, coniferous forest, meadow steppe, shrubs, and cropland than in other vegetation types, whereas desert steppe ecosystems had the lowest. However, we discovered that typical steppe contributed the most to GPP, ET, and WUE IAV. While the coniferous forest contributed the least or negatively to GPP, ET, and WUE IAV. This phenomenon may be associated with the physiological structure, area distribution, and survival condition of vegetation types.

(4) The sensitivity analysis of WUE to GPP and ET revealed that WUE was more sensitive to GPP than ET. The increase of WUE was mainly driven by GPP. Its contribution was 59.36%, accounting for 83.82% of total pixels, which covered most of the central and western regions and the eastern and western parts of Hulun Buir. The contribution of ET was 40.64%, accounting for 16.18% of the total pixels, which were scattered in the Da Hinggan Ling Mountains, the northern part of the Horqin sandy land, and the northern part of the Mu Us Sandy land.

(5) Human activities and climate change were found to be the two main forces driving the variability of WUE, with contributions of 53.52% and 46.48%, respectively. Human activities were the primary cause of WUE changes and their positive effects were significantly stronger than their negative effects. Among climate factors, precipitation was the primary climate factor affecting WUE changes in Inner Mongolia, followed by temperature and solar radiation.

This study sheds light on the distribution characteristics of carbon and hydrology, as well as the response of carbon–water coupling to climate change and human activity in arid and semi-arid regions. It offers guidance on ecological environmental management and water resource utilization in water-limited regions.

Supplementary Materials: The following supporting information can be downloaded at: https://www.mdpi.com/article/10.3390/rs14215422/s1. Figure S1: Spatial pattern of annual average WUE in Inner Mongolia from 2001 to 2020. (a) Spring, (b) Summer, (c) Autumn, and (d)Winter. Figure S2: Degrees of land use dynamics for each league or city in Inner Mongolia from 2000 to 2020. Table S1: Land use transfer matrix in 2000–2020 (km^2).

Author Contributions: Conceptualization, Formal analysis, Writing—original draft, L.M.; Methodology, Writing—reviewing & editing, S.T.; Investigation, Validation, Writing—review & editing, S.Y.; Project administration, Funding acquisition, Y.B.; Visualization, Software, X.H.; Resources, Data curation, T.A. All authors have read and agreed to the published version of the manuscript.

Funding: This study was supported by the International (Regional) Cooperation and Exchange Programs of National Natural Science Foundation of China (41961144019), National Natural Science

Foundation of China (42061070, and 41861056), Fundamental Research Funds for the Inner Mongolia Normal University (2022JBBJ013), Science and Technology Planning Project of Inner Mongolia Autonomous Region (2021GG0183), and Program for Young Talents of Science and Technology in Universities of Inner Mongolia Autonomous Region (NJYT22030). We appreciate all the data developers and their managers, which provide enough data sources for conducting this work.

Institutional Review Board Statement: Not applicable.

Informed Consent Statement: Not applicable.

Data Availability Statement: Not applicable.

Acknowledgments: The authors would like to thank the Editors and the anonymous reviewers for their crucial comments, which improved the quality of this paper.

Conflicts of Interest: The authors declare no conflict of interest.

References

1. Rahman, M.; Islam, M.; Gebrekirstos, A.; Bräuning, A. Disentangling the effects of atmospheric CO_2 and climate on intrinsic water-use efficiency in South Asian tropical moist forest trees. *Tree Physiol.* **2020**, *40*, 904–916.
2. Naser, H.M.; Nagata, O.; Sultana, S.; Hatano, R. Carbon Sequestration and Contribution of CO_2, CH_4, and N_2O Fluxes to Global Warming Potential from Paddy-Fallow Fields on Mineral Soil Beneath Peat in Central Hokkaido, Japan. *Agriculture* **2019**, *10*, 6.
3. IPCC 2021: *Climate Change 2021: The Physical Science Basis. Contribution of Working Group I to the Sixth Assessment Report of the Intergovernmental Panel on Climate Change*; Cambridge University Press, Cambridge, UK; New York, NY, USA, 2021.
4. Guo, F.; Jin, J.; Yong, B.; Wang, Y.; Jiang, H. Responses of water use efficiency to phenology in typical subtropical forest ecosystems—A case study in Zhejiang Province. *Sci. China Earth Sci.* **2020**, *63*, 145–156.
5. Guo, L.; Shan, N.; Zhang, Y.; Sun, F.; Liu, W.; Shi, Z.; Zhang, Q. Separating the effects of climate change and human activity on water use efficiency over the Beijing-Tianjin Sand Source Region of China. *Sci. Total Environ.* **2019**, *690*, 584–595.
6. Zhao, J.; Xu, T.; Xiao, J.; Liu, S.; Mao, K.; Song, L.; Yao, Y.; He, X.; Feng, H. Responses of Water Use Efficiency to Drought in Southwest China. *Remote Sens.* **2020**, *12*, 199.
7. Liu, X.; Feng, X.; Fu, B. Changes in global terrestrial ecosystem water use efficiency are closely related to soil moisture. *Sci. Total Environ.* **2019**, *698*, 134165.
8. Zhang, Q.; Chen, W. Ecosystem water use efficiency in the three-north region of china based on long-term satellite data. *Sustainability* **2021**, *13*, 7977.
9. Ma, J.; Zha, T.; Jia, X.; Tian, Y.; Bourque, C.P.-A.; Liu, P.; Bai, Y.; Wu, Y.; Ren, C.; Yu, H.; et al. Energy and water vapor exchange over a young plantation in northern China. *Agric. For. Meteorol.* **2018**, *263*, 334–345.
10. Chen, S.; Huang, Y.; Wang, G. Detecting drought-induced GPP spatiotemporal variabilities with sun-induced chlorophyll fluorescence during the 2009/2010 droughts in China. *Ecol. Indic.* **2020**, *121*, 107092.
11. Pei, Y.; Dong, J.; Zhang, Y.; Yang, J.; Zhang, Y.; Jiang, C.; Xiao, X. Performance of four state-of-the-art GPP products (VPM, MOD17, BESS, and PML) for grasslands in drought years. *Ecol. Inform.* **2020**, *56*, 101052.
12. Ma, N.; Zhang, Y. Increasing Tibetan Plateau terrestrial evapotranspiration primarily driven by precipitation. *Agric. For. Meteorol.* **2022**, *317*, 108887.
13. Li, Y.; Shi, H.; Zhou, L.; Eamus, D.; Huete, A.; Li, L.; Cleverly, J.; Hu, Z.; Harahap, M.; Yu, Q.; et al. Disentangling climate and LAI effects on seasonal variability in water use efficiency across terrestrial ecosystems in China. *J. Geophys. Res. Biogeosci.* **2018**, *123*, 2429–2443.
14. Ma, J.; Jia, X.; Zha, T.; Bourque, C.P.-A.; Tian, Y.; Bai, Y.; Liu, P.; Yang, R.; Li, C.; Li, C.; et al. Ecosystem water use efficiency in a young plantation in Northern China and its relationship to drought. *Agric. For. Meteorol.* **2019**, *275*, 1–10.
15. Li, G.; Chen, W.; Li, R.; Zhang, X.; Liu, J. Assessing the spatiotemporal dynamics of ecosystem water use efficiency across China and the response to natural and human activities. *Ecol. Indic.* **2021**, *126*, 107680.
16. Liu, Y.; Xiao, J.; Ju, W.; Zhou, Y.; Wang, S.; Wu, X. Water use efficiency of China's terrestrial ecosystems and responses to drought. *Sci. Rep.* **2015**, *5*, 13799.
17. Sun, S.; Song, Z.; Wu, X.; Wang, T.; Wu, Y.; Du, W.; Che, T.; Huang, C.; Zhang, X.; Ping, B.; et al. Spatio-temporal variations in water use efficiency and its drivers in China over the last three decades. *Ecol. Indic.* **2018**, *94*, 292–304.
18. El Masri, B.; Schwalm, C.; Huntzinger, D.N.; Mao, J.; Shi, X.; Peng, C.; Fisher, J.B.; Jain, A.K.; Tian, H.; Poulter, B.; et al. Carbon and water use efficiencies: A comparative analysis of ten terrestrial ecosystem models under changing climate. *Sci. Rep.* **2019**, *9*, 14680.
19. Zhao, J.; Feng, H.; Xu, T.; Xiao, J.; Guerrieri, R.; Liu, S.; Wu, X.; He, X.; He, X. Physiological and environmental control on ecosystem water use efficiency in response to drought across the northern hemisphere. *Sci. Total Environ.* **2021**, *758*, 143599.
20. Du, X.; Zhao, X.; Zhou, T.; Jiang, B.; Xu, P.; Wu, D.; Tang, B. Effects of Climate Factors and Human Activities on the Ecosystem Water Use Efficiency throughout Northern China. *Remote Sens.* **2019**, *11*, 2766.
21. Bai, Y.; Zha, T.; Bourque, C.P.-A.; Jia, X.; Ma, J.; Liu, P.; Yang, R.; Li, C.; Du, T.; Wu, Y. Variation in ecosystem water use efficiency along a southwest-to-northeast aridity gradient in China. *Ecol. Indic.* **2020**, *110*, 105932.

22. Xu, Q. Spatiotemporal variation of water use efficiency and its influencing factors in arid and semi-arid areas of China. *Geogr. Sci. Res.* **2021**, *10*, 126–136.
23. Shang, C.; Wu, T.; Huang, G.; Wu, J. Weak sustainability is not sustainable: Socioeconomic and environmental assessment of Inner Mongolia for the past three decades. *Resour. Conserv. Recycl.* **2019**, *141*, 243–252.
24. Ma, Q.; Wu, J.; He, C.; Fang, X. The speed, scale, and environmental and economic impacts of surface coal mining in the Mongolian Plateau. *Resour. Conserv. Recycl.* **2021**, *173*, 105730.
25. Guo, D.; Song, X.; Hu, R.; Cai, S.; Hao, Y. Grassland type-dependent spatiotemporal characteristics of productivity in Inner Mongolia and its response to climate factors. *Sci. Total Environ.* **2021**, *775*, 145644.
26. Gao, T.; Yang, X.; Jin, Y.; Ma, H.; Li, J.; Yu, H.; Yu, Q.; Zheng, X.; Xu, B. Spatio-Temporal Variation in Vegetation Biomass and Its Relationships with Climate Factors in the Xilingol Grasslands, Northern China. *PLoS ONE* **2013**, *8*, e83824.
27. Su, R.; Yu, T.; Dayananda, B.; Bu, R.; Su, J.; Fan, Q. Impact of climate change on primary production of Inner Mongolian grasslands. *Glob. Ecol. Conserv.* **2020**, *22*, e00928.
28. Quan, Q.; Liang, W.; Yan, D.; Lei, J. Influences of joint action of natural and social factors on atmospheric process of hydrological cycle in Inner Mongolia, China. *Urban Clim.* **2022**, *41*, 101043.
29. Li, S.; Verburg, P.H.; Lv, S.; Wu, J.; Li, X. Spatial analysis of the driving factors of grassland degradation under conditions of climate change and intensive use in Inner Mongolia, China. *Reg. Environ. Chang.* **2012**, *12*, 461–474.
30. Jin, Y.; Yang, X.; Qiu, J.; Li, J.; Gao, T.; Wu, Q.; Zhao, F.; Ma, H.; Yu, H.; Xu, B. Remote sensing-based biomass estimation and its spatio-temporal variations in temperate grassland, Northern China. *Remote Sens.* **2014**, *6*, 1496–1513.
31. Dai, G.; Ulgiati, S.; Zhang, Y.; Yu, B.; Kang, M.; Jin, Y.; Dong, X. The false promises of coal exploitation: How mining affects herdsmen well-being in the grassland ecosystems of Inner Mongolia. *Energy Policy* **2014**, *67*, 146–153.
32. Zhang, Q.; Buyantuev, A.; Fang, X.; Han, P.; Li, A.; Li, F.Y.; Liang, C.; Liu, Q.; Ma, Q.; Niu, J.; et al. Ecology and sustainability of the Inner Mongolian Grassland: Looking back and moving forward. *Landsc. Ecol.* **2020**, *35*, 2413–2432.
33. Wang, S.; Li, R.; Wu, Y.; Zhao, S. Vegetation dynamics and their response to hydrothermal conditions in Inner Mongolia, China. *Glob. Ecol. Conserv.* **2022**, *34*, e02034.
34. Li, X.; Xiao, J. Mapping photosynthesis solely from solar-induced chlorophyll fluorescence: A global, fine-resolution dataset of gross primary production derived from OCO2. *Remote Sens.* **2019**, *11*, 2563.
35. Miralles, D.G.; Holmes, T.; De, J.; Gash, J.H.; Meesters, A.; Dolman, A.J. Global land-surface evaporation estimated from satellite-based observations. *Hydrol. Earth Syst. Sci. Discuss.* **2011**, *7*, 453–469.
36. Miralles, D.G.; Jiménez, C.; Jung, M.; Michel, D.; Fernández-Prieto, D. The wacmos-et project-part 2: Evaluation of global terrestrial evaporation data sets. *Hydrol. Earth Syst. Sci.* **2016**, *20*, 823–842.
37. ElNesr, M.N.; Alazba, A.A. Simple statistical equivalents of the Penman-Monteith formula's parameters in the absence of non-basic climatic factors. *Arab. J. Geosci.* **2010**, *5*, 757–767.
38. Wang, Q.; Guan, Q.; Lin, J.; Luo, H.; Tan, Z.; Ma, Y. Simulating land use/land cover change in an arid region with the coupling models. *Ecol. Indic.* **2021**, *122*, 107231.
39. Yang, B.; Pallardy, S.G.; Meyers, T.P.; Gu, L.; Hanson, P.J.; Wullschleger, S.; Heuer, M.; Hosman, K.P.; Riggs, J.S.; Sluss, D.W. Environmental controls on water use efficiency during severe drought in an Ozark Forest in Missouri, USA. *Glob. Chang. Biol.* **2010**, *16*, 2252–2271.
40. Tang, X.; Ma, M.; Ding, Z.; Xu, X.; Yao, L.; Huang, X.; Gu, Q.; Song, L. Remotely monitoring ecosystem water use efficiency of grassland and cropland in China's arid and semi-arid regions with MODIS data. *Remote Sens.* **2017**, *9*, 616.
41. Yuan, F.; Liu, J.; Zuo, Y.; Guo, Z.; Xu, X. Rising vegetation activity dominates growing water use efficiency in the Asian permafrost region from 1900 to 2100. *Sci. Total Environ.* **2020**, *736*, 139587.
42. Xu, H.; Zhang, Z.; Xiao, J.; Chen, J.; Zhu, M.; Cao, W.; Chen, Z. Environmental and canopy stomatal control on ecosystem water use efficiency in a riparian poplar plantation. *Agric. For. Meteorol.* **2020**, *287*, 107953.
43. Nie, C.; Huang, Y.; Zhang, S.; Yang, Y.; Zhou, S.; Lin, C.; Wang, G. Effects of soil water content on forest ecosystem water use efficiency through changes in transpiration/evapotranspiration ratio. *Agric. For. Meteorol.* **2021**, *308*, 108605.
44. Sen, P.K. Estimates of the Regression Coefficient Based on Kendall's Tau. *J. Am. Stat. Assoc.* **1968**, *63*, 1379–1389.
45. Theil, H. A rank-invariant method of linear and polynomial regression analysis. *Indag. Math.* **1950**, *12*, 173.
46. Kendall, M.G. Rank correlation methods. *Griffin* **1948**, *59*, 575–577.
47. Mann, H.B. Nonparametric tests against trend. *Econom. J. Econom. Soc.* **1945**, *13*, 245–259.
48. Ahlström, A.; Raupach, M.R.; Schurgers, G.; Smith, B.; Arneth, A.; Jung, M.; Reichstein, M.; Canadell, J.G.; Friedlingstein, P.; Jain, A.K.; et al. The dominant role of semi-arid ecosystems in the trend and variability of the land CO_2 sink. *Science* **2015**, *348*, 895–899.
49. Wang, N.; Du, Y.; Liang, F.; Wang, H.; Yi, J. The spatiotemporal response of China's vegetation greenness to human socio-economic activities. *J. Environ. Manag.* **2022**, *305*, 114304.
50. Zhou, Z.; Jin, J.; Yong, B.; Yu, L. Quantifying the influences of climate change and human activities on the grassland in the Southwest Transboundary Basin, China. *J. Environ. Manag.* **2022**, *319*, 115612.
51. Fu, J.; Gong, Y.; Zheng, W.; Zou, J.; Zhang, M.; Zhang, Z.; Qin, J.; Liu, J.; Quan, B. Spatial-temporal variations of terrestrial evapotranspiration across China from 2000 to 2019. *Sci. Total Environ.* **2022**, *825*, 153951.
52. Sun, S.; Song, Z.; Chen, X.; Wang, T.; Zhang, Y.; Zhang, D.; Zhang, H.; Hao, Q.; Chen, B. Multimodel-based analyses of evapotranspiration and its controls in China over the last three decades. *Ecohydrology* **2020**, *13*, e2195.

53. Huang, L.; He, B.; Han, L.; Liu, J.; Wang, H.; Chen, Z. A global examination of the response of ecosystem water-use efficiency to drought based on MODIS data. *Sci. Total Environ.* **2017**, *601*, 1097–1107.
54. Qiu, R.; Han, G.; Ma, X.; Xu, H.; Shi, T.; Zhang, M. A Comparison of OCO-2 SIF, MODIS GPP, and GOSIF Data from Gross Primary Production (GPP) Estimation and Seasonal Cycles in North America. *Remote Sens.* **2020**, *12*, 258.
55. Yang, X.; Yong, B.; Ren, L.; Zhang, Y.; Long, D. Multi-scale validation of GLEAM evapotranspiration products over China via ChinaFLUX ET measurements. *Int. J. Remote Sens.* **2017**, *38*, 5688–5709.
56. Bai, P.; Liu, X. Intercomparison and evaluation of three global high-resolution evapotranspiration products across China. *J. Hydrol.* **2018**, *566*, 743–755.
57. Li, S.; Wang, G.; Sun, S.; Hagan, D.F.T.; Chen, T.; Dolman, H.; Liu, Y. Long-term changes in evapotranspiration over China and attribution to climatic drivers during 1980-2010. *J. Hydrol.* **2021**, *595*, 126037.
58. Kim, D.; Baik, J.; Umair, M.; Choi, M. Water use efficiency in terrestrial ecosystem over East Asia: Effects of climate regimes and land cover types. *Sci. Total Environ.* **2021**, *773*, 145519.
59. Sun, H.; Bai, Y.; Lu, M.; Wang, J.; Tuo, Y.; Yan, D.; Zhang, W. Drivers of the water use efficiency changes in China during 1982-2015. *Sci. Total Environ.* **2021**, *799*, 149145.
60. Bao, G.; Chen, J.; Chopping, M.; Bao, Y.; Bayarsaikhan, S.; Dorjsuren, A.; Tuya, A.; Jirigala, B.; Qin, Z. Dynamics of net primary productivity on the Mongolian Plateau: Joint regulations of phenology and drought. *Int. J. Appl. Earth Obs. Geoinf.* **2019**, *81*, 85–97.
61. Xue, Y.; Liang, H.; Zhang, B.; He, C. Vegetation restoration dominated the variation of water use efficiency in China. *J. Hydrol.* **2022**, *612*, 128257.
62. Ambika, A.K.; Mishra, V. Substantial decline in atmospheric aridity due to irrigation in India. *Environ. Res. Lett.* **2020**, *15*, 124060.
63. Zou, J.; Ding, J.; Welp, M.; Huang, S.; Liu, B. Using MODIS data to analyse the ecosystem water use efficiency spatial-temporal variations across Central Asia from 2000 to 2014. *Environ. Res.* **2020**, *182*, 108985.
64. Yang, Y.; Guan, H.; Batelaan, O.; McVicar, T.R.; Long, D.; Piao, S.; Liang, W.; Liu, B.; Jin, Z.; Simmons, C.T. Contrasting responses of water use efficiency to drought across global terrestrial ecosystems. *Sci. Rep.* **2016**, *6*, 23284.
65. Feng, X.; Fu, B.; Piao, S.; Wang, S.; Ciais, P.; Zeng, Z.; Lü, Y.; Zeng, Y.; Li, Y.; Jiang, X.; et al. Revegetation in China's Loess Plateau is approaching sustainable water resource limits. *Nat. Clim. Chang.* **2016**, *6*, 1019–1022.
66. Liu, Y.; Xiao, J.; Ju, W.; Xu, K.; Zhou, Y.; Zhao, Y. Recent trends in vegetation greenness in China significantly altered annual evapotranspiration and water yield. *Environ. Res. Lett.* **2016**, *11*, 094010.
67. Ouyang, X.; Wang, J.; Chen, X.; Zhao, X.; Ye, H.; Watson, A.E.; Wang, S. Applying a projection pursuit model for evaluation of ecological quality in Jiangxi Province, China. *Ecol. Indic.* **2021**, *133*, 108414.
68. Yang, L.; Feng, Q.; Wen, X.; Barzegar, R.; Adamowski, J.F.; Zhu, M.; Yin, Z. Contributions of climate, elevated atmospheric CO_2 concentration, and land surface changes to variation in water use efficiency in Northwest China. *Catena* **2022**, *213*, 106220.
69. Xu, H.; Wang, X.; Zhao, C.; Zhang, X. Responses of ecosystem water use efficiency to meteorological drought under different biomes and drought magnitudes in northern China. *Agric. For. Meteorol.* **2019**, *278*, 107660.
70. Liu, Z.; Liu, Y.; Li, Y. Anthropogenic contributions dominate trends of vegetation cover change over the farming-pastoral ecotone of northern China. *Ecol. Indic.* **2018**, *95*, 370–378.

J. Geogr. Sci. 2023, 33(1): 169-194
DOI: https://doi.org/10.1007/s11442-023-2078-x

Spatiotemporal variations of water use efficiency and its driving factors in Inner Mongolia from 2001 to 2020

MEI Li[1], *TONG Siqin[1,3], YIN Shan[1,2], BAO Yuhai[1,2], HUANG Xiaojun[1,2], ALATENG Tuya[1], WANG Yongfang[1], GUO Enliang[1], YUAN Zhihui[1], NASHUN Dalai[1], GAO Suriguga[1], LIU Xinyi[1], YE Zhigang[1]

1. College of Geographical Science, Inner Mongolia Normal University, Hohhot 010022, China;
2. Inner Mongolia Key Laboratory of Remote Sensing and Geographic Information Systems, Inner Mongolia Normal University, Hohhot 010022, China;
3. Inner Mongolia Key Laboratory of Disaster and Ecological Security on the Mongolian Plateau, Inner Mongolia Normal University, Hohhot 010022, China

Abstract: Water use efficiency (WUE) is an important variable to explore coupled relationships in carbon and water cycles. In this study, we first compared the spatial variations of annual gross primary productivity (GPP) and evapotranspiration (ET) using four GPP and ET products. Second, we selected the products closest to the flux towers data to estimate WUE. Finally, we quantitatively analyzed the impact of climate change and soil water content on WUE. The results showed that: (1) Four GPP and ET products provided good performance, with GOSIF-GPP and FLDAS-ET exhibiting a higher correlation and the smallest errors with the flux tower data. (2) The spatial pattern of WUE is consistent with that of GPP and ET, gradually decreasing from the northeast to the southwest. Higher WUE values appeared in the northeast forest ecosystem, and lower WUE values occurred in the western Gobi Desert, with a value of 0.28 gC m^{-2} mm^{-1}. The GPP and ET products showed an increasing trend, while WUE showed a decreasing trend (55.15%) from 2001 to 2020. (3) The spatial relationship between WUE and driving factors reveal the variations in WUE of Inner Mongolia are mainly affected by soil moisture between 0 and 10 cm (SM0–10cm), vapor pressure deficit (VPD), and precipitation, respectively. (4) In arid regions, VPD and precipitation exhibit a major influence on WUE. An increase in VPD and precipitation has a negative and positive effect on WUE, with threshold values of approximately 0.36 kPa and 426 mm, respectively. (5) In humid regions, SM0–10cm, VPD, SM10–40cm, and SM40–100cm exert a significant impact on WUE, especially SM0–10cm, and weakens with increasing soil depths, these differences may be related to physiological structure and living characteristics of vegetation types in different climate regimes. Our results emphasize the importance of VPD and soil moisture

Received: 2021-12-08 **Accepted:** 2022-08-25
Foundation: National Natural Science Foundation of China, No.42061070, No.61631011; Science and Technology Fundamental Resources Survey Special Sub-project, No.2017FY101301-4; Fundamental Research Funds for the Inner Mongolia Normal University, No.2022JBBJ013
Author: Mei Li (1992–), PhD Candidate, E-mail: meili0125@163.com
***Corresponding author:** Tong Siqin (1991–), Associate Professor, E-mail: tongsq223@imnu.edu.cn

in regional variability in WUE.

Keywords: gross primary productivity (GPP); evapotranspiration (ET); water use efficiency (WUE); climate change; soil water content

1 Introduction

Water use efficiency (WUE) is defined as the ratio of ecosystem gross primary productivity (GPP) and evapotranspiration (ET), it reflects the coupling of carbon and water cycles in terrestrial ecosystems (Huang *et al*., 2017; Li *et al*., 2018c; Yang *et al*., 2020; Zhao *et al*., 2020). As an effective indicator for assessing ecological sustainable development, WUE associates carbon and water exchange processes between terrestrial ecosystems and the atmosphere, as well as quantifying how much water an ecosystem uses relative to carbon assimilation (Zhu *et al*., 2015; Du *et al*., 2019; Guo *et al*., 2019a; 2019b; Xu *et al*., 2020; Zhao *et al*., 2021), it is crucial to global ecosystem functions, ecosystem services, and ecosystem feedbacks to climate change (Niu *et al*., 2011; Li *et al*., 2018c; Liu *et al*., 2019; Xu *et al*., 2020). Therefore, a better insight into the variations and regulating mechanisms of WUE would help to achieve regional sustainable development and water resource utilization.

Currently, there are several methods available to estimate WUE, namely eddy covariance (EC), process-oriented ecosystem models (Huang *et al*., 2016; Yang *et al*., 2016), and satellite-based remote sensing (Zhang *et al*., 2015; Zou *et al*., 2020). Thereinto EC is the standard estimation method with the highest accuracy, but it is limited to the smaller regional scales (Brummer *et al*., 2012). Models methods depend on the input data and considered parameters and can effectively provide long-term dynamics of WUE over larger regional scales. There are large uncertainties in the model inputs and parameters (Zou *et al*., 2020). Recently, many studies have employed GPP and ET remote sensing products to estimate WUE (Du *et al*., 2019; Zou *et al*., 2020). Satellite remote sensing provides a variety of ET and GPP products with different temporal and spatial characteristics, such as the Moderate-Resolution Imaging Spectroradiometer (MODIS) (Running *et al*., 2004), the Breathing Earth System Simulator (BESS) (Ryu *et al*., 2011; Jiang and Ryu, 2016), and the Global Land Surface Satellite (GLASS) products (Yuan *et al*., 2010). However, these products show great variation due to their different model algorithms, input parameters, and sensors (Li *et al*., 2021b). Therefore, it is necessary to evaluate the accuracy of GPP and ET products before estimating WUE.

Previous studies have reported that ecosystem WUE may be affected by biotic and abiotic factors such as leaf area index (LAI), precipitation, vapor pressure deficit (VPD), solar radiation, and temperature (Sun *et al*., 2018; Guo *et al*., 2019a; Wu *et al*., 2019; Wang *et al*., 2020; Zhao *et al*., 2021). The influence of environmental factors on WUE differs under varying temporal and spatial scales with climate conditions (Song *et al*., 2017; Du *et al*., 2019). In arid and semi-arid regions, Sun *et al*. (2018) and Bai *et al*. (2020) noted that the variability of WUE was influenced by precipitation. Xu *et al*. (2021) found that WUE in arid and semi-arid regions of China was positively correlated with precipitation and temperature, while Liu *et al*. (2019) found that variations in WUE are mostly affected by soil moisture in most regions. Zhang *et al*. (2022) reported that groundwater depth plays an important role in spatial variations of WUE in arid and semi-arid regions. Given the above studies, it is still

disputed as to what are the major factors forcing variations in WUE under the background of climate change.

The arid, semi-arid, and sub-humid regions of China form an ecological fragile belt, while Inner Mongolia, located in northern China, is a typical inland arid and semi-arid region (Mu *et al*., 2013; Luo *et al*., 2021). Grassland is one of the widely distributed ecosystems in Inner Mongolia, which play a pivotal role in the global carbon-water cycle and climate systems (Yu *et al*., 2020; Guo *et al*., 2021). However, recently the grassland environment has experienced serious damage, such as vegetation degradation, land desertification, and shrinking lakes (John *et al*., 2013; Tao *et al*., 2015; Huang *et al*., 2021), which seriously threaten ecosystem function and socioeconomic development. WUE is a vital property of ecosystem function and an important basis for promoting the sustainable development of regional ecosystems (Du *et al*., 2019; Guo *et al*., 2019a; Liu *et al*., 2019). However, few studies have focused on WUE variability and its driving mechanisms in fragile ecosystems. Therefore, in this work, we take Inner Mongolia as the study region and quantitatively assess the effects of driving factors (climatic change and soil water content) on WUE variations. Specifically, our objectives are: (1) to compare the spatiotemporal patterns of four GPP and ET products, and select products that have good consistency with the flux towers observations data to estimate WUE, (2) to analyze the spatiotemporal variations and trends in WUE, (3) to discuss the impact of climatic factors and soil water content to variations in WUE, and (4) to determine the threshold of the key factors that control changes in WUE.

2 Materials and methods

2.1 Study area

Inner Mongolia (37°24'–53°23'N, 97°12'–126°04'E) is located along the northern border of China. Its landscape consists mainly of high plains, and the terrain slopes downward from west to east, with an average altitude of above 1000 m (Figure 1a). Inner Mongolia is an important portion of the Eurasian grasslands (Dai *et al*., 2016; Li *et al*., 2018a). Grassland is the major vegetation type of Inner Mongolia, with the different types varying from east to west as forest (11.27% of the total area), meadow steppe (10.31%), typical steppe (18.85%), desert steppe (14.50%), and the Gobi Desert (18.92%), as presented in Figure 1b. Vegetation type data were obtained from a 1:1,000,000 scale vegetation map of Inner Mongolia and rasterized to a spatial resolution of 0.083°. Inner Mongolia has a temperate continental climate, with an annual average temperature ranging between –3.15 and 9.8℃ and annual precipitation between 50 and 550 mm based on meteorological stations from 2001 to 2020. We used the humidity region definition from China's eco-geographical region map of the Institute of Geographic Sciences and Natural Resources Research. According to the annual aridity index (AI), the study area can be divided into humid (AI<1), sub-humid (1<AI<1.49), semi-arid (1.5<AI<4), and arid zones (AI≥4) from east to west. In this study, humid regions include humid and sub-humid zones with an annual aridity index of less than 1.49, while arid regions refer to arid and semi-arid zones with an annual aridity index greater than 1.5 (Figure 1b).

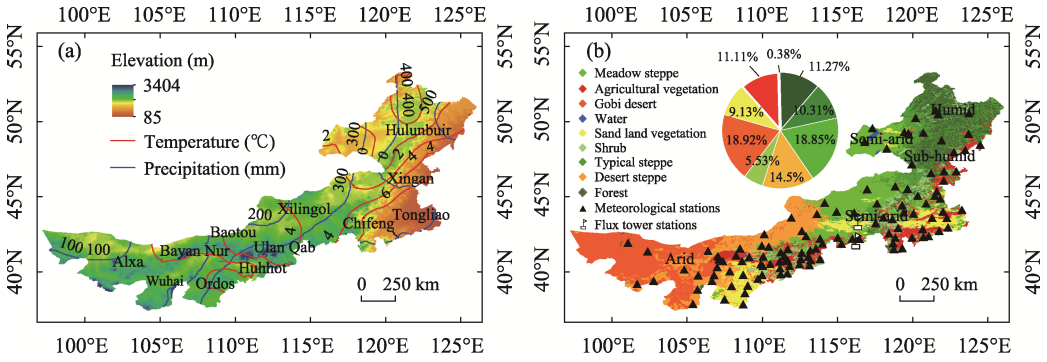

Figure 1 Spatial distributions of annual average temperature and annual precipitation (a), and different vegetation types, flux tower observation stations, meteorological stations, and ecological climatic zones (b) of Inner Mongolia

2.2 Data sources

2.2.1 GPP products

In this study, we employed four GPP products: the global OCO-2-based solar-induced chlorophyll fluorescence product (GOSIF), Global Land Surface Satellite (GLASS), Breathing Earth System Simulator (BESS), and the Moderate Resolution Imaging Spectroradiometer (MODIS) products (Table 1). These four GPP products have been widely used for evaluating carbon sinks and monitoring the vegetation productivity of regional and even global terrestrial ecosystems.

(1) GOSIF-GPP

Li and Xiao (2019) based on linear relationships between SIF and GPP to generate a new global GPP product, that is "GOSIF-GPP" (http://data.globalecology.unh.edu/). This product provides 8-daily GPP values with a 0.05° spatial resolution from 2001 to 2020. This product is widely used for the evaluation of vegetation productivity (Li and Xiao, 2019a; 2019b).

(2) GLASS-GPP

The GPP data are produced from the GLASS product generation system, which employs an improved algorithm for the light use efficiency model (EC-LUE), with a spatial resolution of 0.05° and a temporal resolution of 8 days from 1982 to 2018. This data was produced by National Earth System Science Data Center, National Science & Technology Infrastructure of China (http://www.geodata.cn) (Yuan *et al*., 2010).

(3) BESS-GPP

The BESS GPP dataset was generated from a complex process-based model and driven by multiple modules, which are coupled atmospheric and canopy radiative transfers, canopy photosynthesis, transpiration, and energy balance (Ryu *et al*., 2011; Jiang and Ryu, 2016). The BESS data was obtained from the Environmental Ecology Lab of Seoul National University (http://environment.snu.ac.kr/data/), with a spatial resolution of 0.05° and temporal resolutions of daily from 2000 to 2017.

(4) MODIS-GPP

The MODIS GPP products (MOD17A2H) adopted a light use efficiency model algorithm using MODIS vegetation indices as input surface vegetation information, with an 8-day

composite and a 500 m resolution from 2001 to 2020 (Running *et al*., 2004). This product is provided by the National Aeronautics and Space Administration (NASA) (https://ladsweb.modaps.eosdis.nasa.gov/). The MODIS product was resampled to a 0.05º spatial resolution using the nearest neighbor methods.

Table 1 Major information on four GPP products is used herein

GPP Products	Spatial and temporal resolution	Units	Year	Data source	References
GOSIF	0.05°, 8 days	gC $m^{-2}d^{-1}$	2000–2020	http://data.globalecology.unh.edu/	Li and Xiao, 2019a; 2019b
BESS	0.05°, daily	gC $m^{-2}d^{-1}$	2000–2017	http://environment.snu.ac.kr/data	Ryu *et al*., 2011; Jiang and Ryu, 2016
GLASS	0.05°, 8 days	gC $m^{-2}d^{-1}$	1982–2018	http://glass.umd.edu	Yuan *et al*., 2010
MOD17A2	500 m, 8 days	kgC $m^{-2}8d^{-1}$	2001–2020	https://ladsweb.modaps.eosdis.nasa.gov/	Running *et al*., 2004

2.2.2 ET products

In this study, we employed four long-time series gridded ET products, namely the Global Land Evaporation Amsterdam Model version 3.5a (GLEAM 3.5a), Famine Early Warning Systems Network (FEWS NET) Land Data Assimilation System (FLDAS), Global Land Data Assimilation System (GLDAS), and the Moderate Resolution Imaging Spectroradiometer (MODIS) products (Table 2).

(1) GLEAM-ET

The GLEAM remote sensing product is derived from modified Priestley-Taylor algorithms that separately estimate the different components of ET (i.e., soil evaporation, transpiration, and interception loss). In addition, GLEAM provides surface and root-zone soil moisture, potential evaporation, and evaporative stress conditions (Miralles *et al*., 2011; Martens *et al*., 2017). This set of algorithms produces two datasets (GLEAM 3.5a and 3.5b), while in this study, the evaporation estimates from the GLEAM 3.5a datasets were used (https://www.gleam.eu/), which spans from 1981 to 2020 and has a spatial resolution of 0.25° and a temporal resolution of daily.

(2) FLDAS-ET

The FLDAS products (https://daac.gsfc.nasa.gov/) are based on multiple meteorological inputs or use existing land surface models, generated ensembles of soil moisture, ET, and other variables (McNally *et al*., 2017). The monthly ET datasets cover the period 1982–2020 with a spatial resolution of 0.1°.

(3) GLDAS-ET

The ET data provided by GLDAS is generated by integrating satellite products and ground observational data using advanced land surface modeling and data assimilation techniques (Rodell *et al*., 2004). Currently, GLDAS has three versions, i.e., GLDAS-2.0, GLDAS-2.1, and GLDAS-2.2. GLDAS-2.0 is forced entirely with the Princeton meteorological input data. GLDAS-2.1 product with a 3-hour temporal resolution is forced by a combination of model and observational data. GLDAS-2.2 product use data assimilation (DA). We selected the GLDAS-2.2 product with a 0.25° spatial resolution and daily temporal coverage for the period from 2003–2020, and the GLDAS-2.0 data to cover the period from 2001 to 2003 (https://daac.gsfc.nasa.gov/).

(4) MODIS-ET

The MODIS ET (MOD16A2) products for the period 2001–2020 were downloaded from NASA (https://ladsweb.modaps.eosdis.nasa.gov/), and are estimated based on the Penman-Monteith model, which uses meteorological reanalysis data and vegetation property dynamics retrieved from MODIS as input variables (Mu *et al*., 2007; Mu *et al*., 2011). This is an 8-day cumulative MODIS ET dataset with a 1 km spatial resolution. To make them comparable, the four ET products were resampled to a 0.05° spatial resolution, and their units were uniformly converted into mm/d.

Table 2 Major information of the four ET products used herein

ET Products	Spatial and temporal resolution	Units	Year	Data source	References
GLEAM3.5a	0.25°, daily	mm d^{-1}	1981–2020	https://www.gleam.eu/	Miralles *et al*., 2011; Martens *et al*., 2017
FLDAS	0.1°, monthly	kg $m^{-2}s^{-1}$	1982–2020	https://daac.gsfc.nasa.gov/	McNally *et al*., 2017
GLDAS2.0 GLDAS2.2	0.25°, daily	kg $m^{-2}s^{-1}$	2000–2003 2004–2020	https://daac.gsfc.nasa.gov/	Rodell *et al*., 2004
MOD16A2	1 km, 8-daily	kg $m^{-2}8d^{-1}$	2001–2020	https://ladsweb.modaps.eosdis.nasa.gov/	Mu *et al*., 2007; 2011

2.2.3 Flux tower observations data

We compiled three flux towers observations data in Inner Mongolia obtained from FLUXNET2015 (http://fluxnet.fluxdata.org/) and ChinaFlux (http://www.chinaflux.org/), respectively, namely Duolun grassland (D01), Duolun Degraded Meadow, and Inner Mongolia sites (Figure 1c and Table S1). Grasslands are these site major vegetation types. The flux towers continuously recorded measurements of net ecosystem exchange (NEE), ecosystem respiration (ER), latent heat flux (LE), and GPP over different time scales. The observed GPP is named GPP_NT_VUT_MEAN (GPP=ER-NEE) in the dataset (Wu *et al*., 2019; Xu *et al*., 2020; Yang *et al*., 2020). However, the observed ET was usually reflected with latent heat flux (Wang *et al*., 2018). To obtain daily observed ET (mm d^{-1}), need to be converted from the daily EC latent heat flux (LE, W m^{-2}) from the two flux tower sites using the following equation (Li *et al*., 2018b; Ma *et al*., 2018):

$$ET = \frac{LE}{\lambda} \tag{1}$$

where λ is the latent heat of vaporization of water (2.45 MJ kg^{-1}).

2.2.4 Climate data

Climatic factors are important variables that affect the photosynthesis and transpiration of plants (Zhao *et al*., 2021). To explore the impact of climate change on the WUE, the precipitation, vapor pressure deficit (VPD), temperature, and wind speed data were used in this study. The monthly wind speed was extracted from the FLDAS products. The daily precipitation, temperature, and VPD come from 118 meteorological stations distributed across Inner Mongolia and were provided by the China Meteorological Data Network (http://data.cma.cn) for the period 2001–2020. Climate data were interpolated to a 0.05°×0.05° spatial resolution by the kriging methods.

2.2.5 Soil water content data

As a critical source of water for maintaining physiological activity, the dynamics of soil moisture can influence vegetation features such as phenology, productivity, and ET (Luo *et al*., 2021; Cleverly *et al*., 2016). Therefore, the most recently developed FLDAS soil moisture products for four different layers, namely 0–10 cm (SM0–10cm), 10–40 cm (SM10–40cm), 40–100 cm (SM40–100cm), and 100–200 cm (SM100–200cm), and terrestrial water storage (TWS) were chosen in this study. The TWS for the period 2001–2020 was derived from the GLDAS (https://daac.gsfc.nasa.gov/). To avoid spatial resolution mismatch, all gridded products were resampled to a spatial resolution of 0.05°.

A set of nine variables, including climate factors, and soil water content, were selected as the drivers of the changes in WUE for the period 2001–2020 (Table 3).

Table 3 Variables as the drivers of the changes in WUE for Inner Mongolia

Variable class	Variable name and unit	Spatial and temporal resolution	Data source
Climate factors	Precipitation (mm)	0.05°, daily	China Meteorological Data Network (http://data.cma.cn)
	Temperature (℃)	0.05°, daily	China Meteorological Data Network (http://data.cma.cn)
	Vapor pressure deficit (kPa)	0.05°, daily	China Meteorological Data Network (http://data.cma.cn)
	Wind speed (m/s)	0.1°, monthly	FLDAS products (https://daac.gsfc.nasa.gov/)
Soil water content	Soil moisture 0–10 cm (m^3 m^{-3})	0.1°, monthly	FLDAS products (https://daac.gsfc.nasa.gov/)
	Soil moisture 10–40 cm (m^3 m^{-3})	0.1°, monthly	FLDAS products (https://daac.gsfc.nasa.gov/)
	Soil moisture 40–100 cm (m^3 m^{-3})	0.1°, monthly	FLDAS products (https://daac.gsfc.nasa.gov/)
	Soil moisture 100–200 cm (m^3 m^{-3})	0.1°, monthly	FLDAS products (https://daac.gsfc.nasa.gov/)
	Terrestrial water storage (mm)	0.25°, daily	GLDAS product (https://daac.gsfc.nasa.gov/)

2.3 Methods

2.3.1 Ecosystem water use efficiency

WUE (gC m^{-2} mm^{-1}) was defined as the ratio of GPP (gC m^{-2} yr^{-1}) to ET (mm yr^{-1}) at the ecosystem scale (Huang *et al*., 2016; Ma *et al*., 2019; Yang *et al*., 2020; Li *et al*., 2021a; Tao *et al*., 2022):

$$WUE = \frac{GPP}{ET} \tag{2}$$

when *WUE* is greater than 1, the water loss is less than the carbon assimilation, while for *WUE* is less than 1, the water loss is greater than the carbon assimilation.

2.3.2 Vapor pressure deficit

VPD is an important atmospheric constraint for affects the water and carbon fluxes (Novick *et al*., 2016), it refers to the difference between the water vapor pressure in a saturated state and the actual vapor pressure in the air at a certain temperature. It is widely used to measure atmospheric drought extent (Yuan *et al*., 2019). In this study, the VPD (kPa) was calculated from the relative air humidity and temperature provided by 118 meteorological stations us-

ing the following:

$$VPD = 0.611 \times e^{\frac{17.27 \times T_a}{T_a + 237.3}} \times \left(1 - \frac{RH}{100}\right) \tag{3}$$

where T_a is the temperature (T_a, ℃) and RH is relative humidity (RH, %).

2.3.3 GPP and ET products validation

The reliability and accuracy of four GPP and ET gridded products were validated using flux tower observations data. Four metrics, namely the Pearson correlation coefficient (R, Equation 4), the root mean square error (RMSE, Equation 5), mean absolute error (MAE, Equation 6), and mean bias (Bias, Equation 7), are used to evaluate the agreement between the gridded products values and flux tower observed values at the site scales. The equations are as follows:

$$R = \frac{\sum_{i=1}^{n}\left(x_i - \overline{X}\right)\left(y_i - \overline{y}\right)}{\sqrt{\sum_{i=1}^{n}\left(x_i - \overline{x}\right)^2 \sum_{i=1}^{n}\left(y_i - \overline{y}\right)^2}} \tag{4}$$

$$RMSE = \sqrt{\frac{\sum_{i=1}^{n}\left(x_i - y_i\right)^2}{n}} \tag{5}$$

$$MAE = \sum_{i=1}^{n}\left|x_i - y_i\right| \tag{6}$$

$$Bias = \frac{1}{n}\sum_{i=1}^{n}\left(x_i - y_i\right) \tag{7}$$

where x_i represents the flux tower observed GPP and ET, y_i represents the values of GPP and ET from the considered products; $\overline{x}$ and $\overline{y}$ represents the corresponding average values of the observed data and products (GPP or ET), and n is the number of samples.

2.3.4 Partial correlation analysis

In this study, partial correlation analysis was employed to measure the relative importance of GPP or ET to variations in WUE. By controlling for the effects of other variables, we determine the degree of the relationship between two variables as follows:

$$R_{XY,Z} = \frac{R_{XY} - R_{XZ}R_{YZ}}{\sqrt{\left(1 - R_{XZ}^2\right)\left(1 - R_{YZ}^2\right)}} \tag{8}$$

where $R_{XY,Z}$ is the partial correlation coefficient between X and Y after removing the effects from Z. R_{XY}, R_{XZ}, and R_{YZ} are the correlation coefficients between X and Y, X and Z, and Y and Z, respectively. If the ratio of the partial correlation coefficient between WUE and GPP to that between WUE and ET is greater than 1, then GPP plays a prominent role. By contrast, if the value is less than 1, it indicates that WUE is mainly driven by ET (Zhao *et al*., 2021).

2.3.5 Maximum correlation analysis method

To diagnose the key dominant factors of variations in WUE using the maximum correlation coefficient method. The driving factors corresponding to the maximum correlation coeffi-

cients (R_{max}) can be regarded as the key dominant factors of changes in WUE. The general equation is as follows:

$$R_i = corr\left(WUE, df_i\right) \tag{9}$$

$$R_{max} = Max\left(R_i\right) \tag{10}$$

where R_i is the correlation coefficient between the driving factors and *WUE*, with the driving factors including temperature, precipitation, wind speed, VPD, TWS, SM0–10cm, SM10–40cm, SM40–100cm, and SM100–200cm; and R_{max} is the maximum value of R_i.

3 Results

3.1 Spatial distribution in annual GPP and ET over Inner Mongolia

Figures 2 and 3 display the spatial distribution of the four GPP and ET products over Inner Mongolia for the periods 2001–2017 and 2001–2020, respectively. We found that spatial variation of annual average GPP showed good consistency with ET. The highest and lowest GPP values from four gridded products were found in the northeast forest and western Gobi Desert. The annual GPP of the forest areas in the northeast is greater than 750 gC m^{-2} yr^{-1}, while the annual vegetation productivity of the Gobi Desert in the southwest is less than 150 gC m^{-2} yr^{-1} (Figure 2). The annual average GPP of the four products was estimated to be

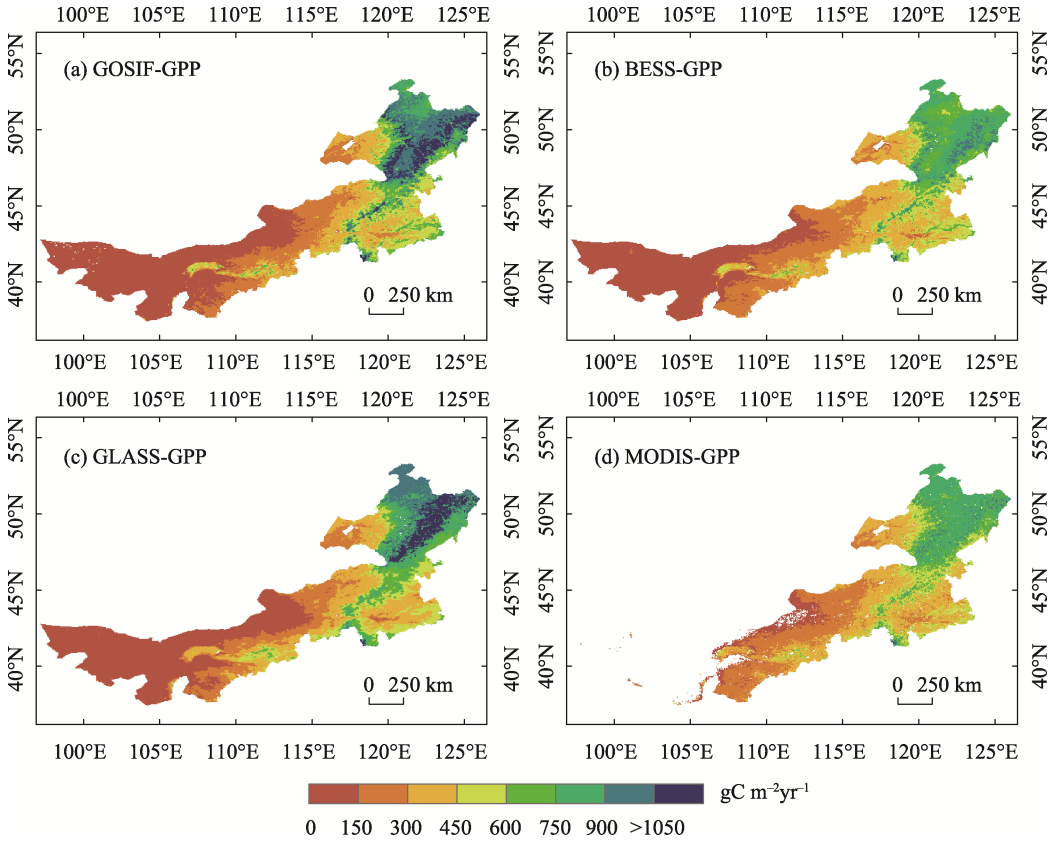

Figure 2 Spatial distributions of annual average GPP over Inner Mongolia during 2001–2017 (a. GOSIF, b. BESS, c. GLASS, d. MODIS products)

between 449.50 and 500.25 gC m^{-2} yr^{-1} from 2001 to 2017 (MODIS–GPP boundary as standard). The GPP values quantified by GOSIF and GLASS products are exhibited higher than those quantified by BESS and MODIS products. The four ET products also show a similar spatial distribution pattern (Figure 3), gradually decreasing from the east to west and from south to north, and exhibited latitude and longitude geographical zonality. However, it can be observed that there are obvious differences in the absolute values of the four ET products. The annual ET derived from four products are all highest in the northeast forest (greater than 480 mm yr^{-1}) and lowest in the southwest Gobi Desert (less than 60 mm yr^{-1}). Besides, the annual average ET was found to be 336.29 mm yr^{-1}, 316.41 mm yr^{-1}, 322.60 mm yr^{-1}, and 248.26 mm yr^{-1} for the GLEAM, GLDAS, FLDAS, and MODIS products, respectively (MODIS–ET boundary as standard). The ET values from the GLEAM, GLDAS, and FLDAS products are generally greater than those for the MODIS product.

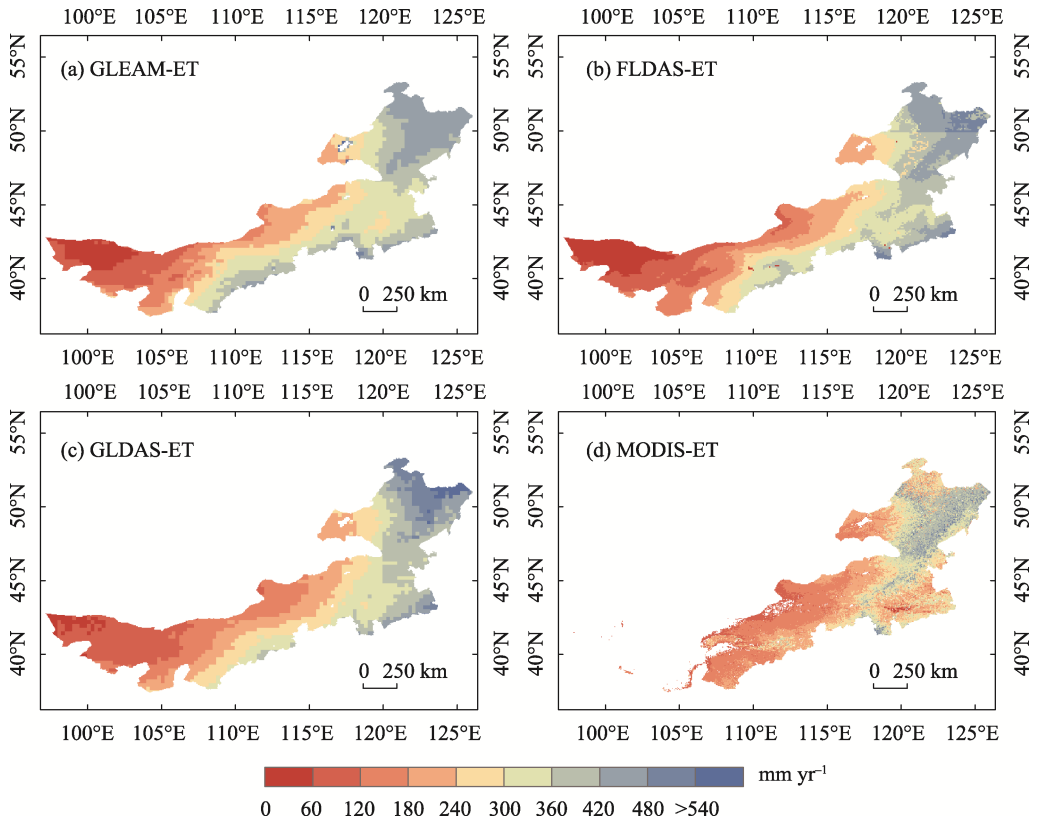

Figure 3 Spatial distributions of annual average ET over Inner Mongolia during 2001–2020 (a. GLEAM, b. FLDAS, c. GLDAS, d. MODIS products)

3.2 Spatiotemporal trends in annual GPP and ET over Inner Mongolia

Spatial distribution of trends in GPP from 2001 to 2017 over Inner Mongolia, as presented in Figure 4. The four GPP products all showed an increasing trend, with the areas corresponding to such a trend for the GOSIF, BESS, MODIS, and GLASS products accounting for 85.23%, 90.27%, 95.33%, and 67.32% of the total area, respectively. Increasing trends are mainly distributed in Mu Us sandy land and eastern Inner Mongolia. However, there are de-

creasing trends in the north of Chifeng, the east of Xilingol, the central Hulunbuir, and the northwest of Alxa. In terms of the spatial distribution of trends in ET during the period 2001–2020 (Figure 5), the four ET products show obvious differences and similarities. Increasing trends were derived for the ET of the GLEAM, FLDAS, and MODIS products, accounting for 82.96%, 98.01%, and 92.09% of the total area, respectively. And it is mainly located in vast areas of study regions, whereas there is an opposite trend in the GLDAS products, accounting for 58.87% of the total area, mainly distributed in central Inner Mongolia.

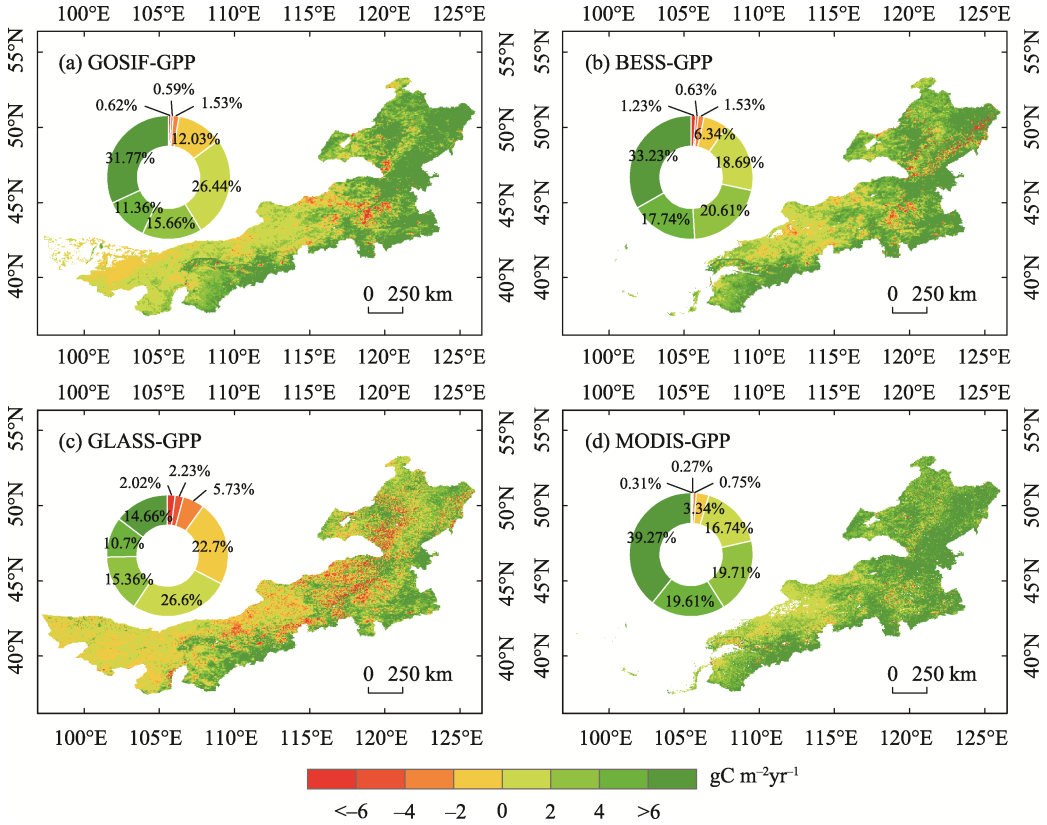

Figure 4 Spatial distributions of trends in annual GPP over Inner Mongolia during 2001–2017 (a. GOSIF, b. BESS, c. GLASS, d. MODIS products)

The performance and accuracy of the four GPP and ET products based on observation data at the three flux tower sites were verified (Figures 6 and 7). As shown in Figures 6a–6f, the four GPP products all showed a high correlation with the flux tower GPP. The GOSIF has the best correlations (R^2=0.611) compared with the MODIS (R^2=0.584), GLASS (R^2=0.518), and BESS (R^2=0.492) products, as well as the smallest errors. Interestingly, although the GLASS correlation coefficient was greater than that for BESS, the RMSE, MAE, and Bias of the GLASS products were greater than those of the BESS product. Furthermore, we found that all of these four gridded products overestimate GPP, with an average Bias of less than zero, especially the GLASS product with a Bias value of –0.48.

The ET correlation analysis revealed that the FLDAS has a high correlation with the

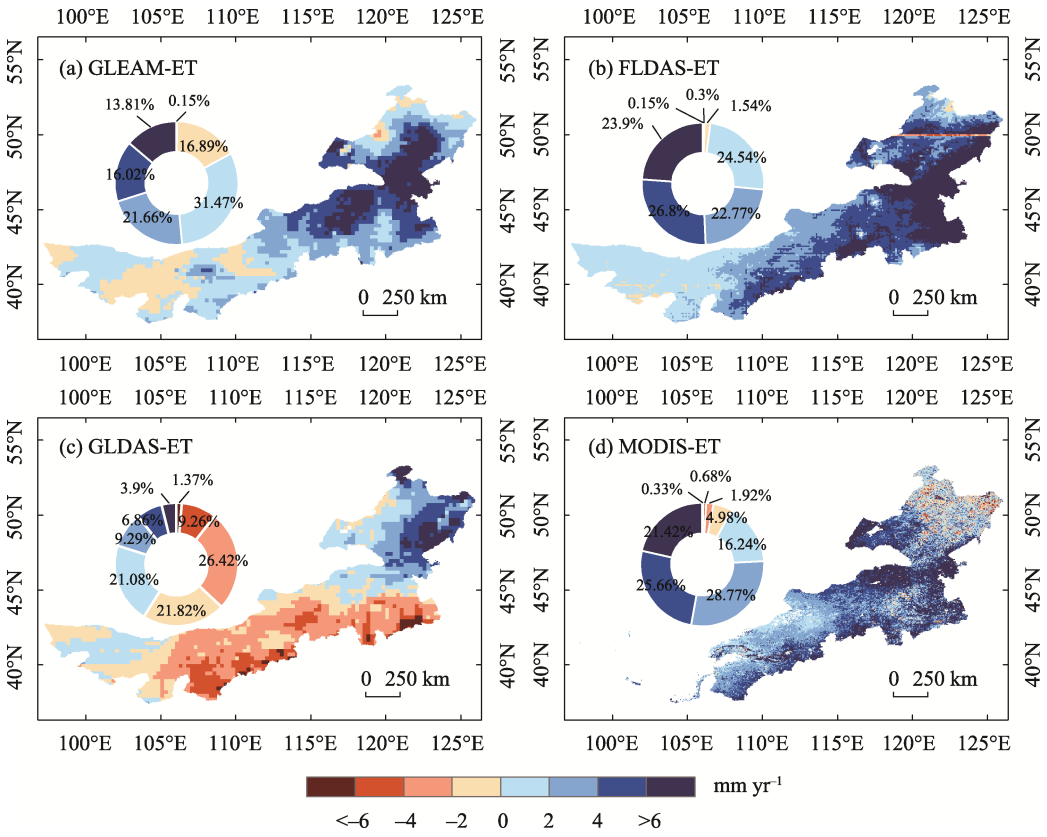

Figure 5 Spatial distributions of trends in annual ET over Inner Mongolia during 2001–2020 (a. GLEAM, b. FLDAS, c. GLDAS, d. MODIS products)

observed ET (R^2=0.871) compared to GLEAM, GLDAS, and MODIS products. The MODIS exhibited a relatively weak correlation and higher errors with observed ET, with an R^2 value of 0.753, RMSE, MAE, and Bias values of 16.05, 11.77, and 8.14, respectively (Figures 7a–7f). In addition, GLDAS, MODIS, and FLDAS underestimated the observed ET on a monthly scale with Bias values of 1.23, 8.15, and 0.04, respectively. Whereas GLEAM overestimates ET, with a Bias value of –3.77. Overall, the GOSIF and FLDAS products agreed well with flux tower data than other products, along with the smallest errors. Therefore, the GOSIF and FLDAS products were selected to characterize variations in GPP and ET, and utilize them to estimate WUE.

3.3 Spatiotemporal variations and trends in WUE and drivers

From the spatial pattern of WUE in Inner Mongolia from 2001 to 2020 (Figure 8), it can be seen that the spatial regime of WUE matches well with that of variations in GPP and ET, all showing gradually decreasing values from northeast to the southwest. The annual average WUE in Inner Mongolia during this period was 1.23 gC m^{-2} mm^{-1}, ranging from approximately 0.002 to 4.65 gC m^{-2} mm^{-1}. The high WUE values were mainly in the forest biome across northeast Inner Mongolia, with the average values of 2.19 gC m^{-2} mm^{-1}, followed by meadow steppe (2.05 gC m^{-2} mm^{-1}), cropland (1.44 gC m^{-2} mm^{-1}), shrubs (1.39 gC m^{-2} mm^{-1}), typical steppe (1.22 gC m^{-2} mm^{-1}), sand land vegetation (0.96 gC m^{-2} mm^{-1}), and

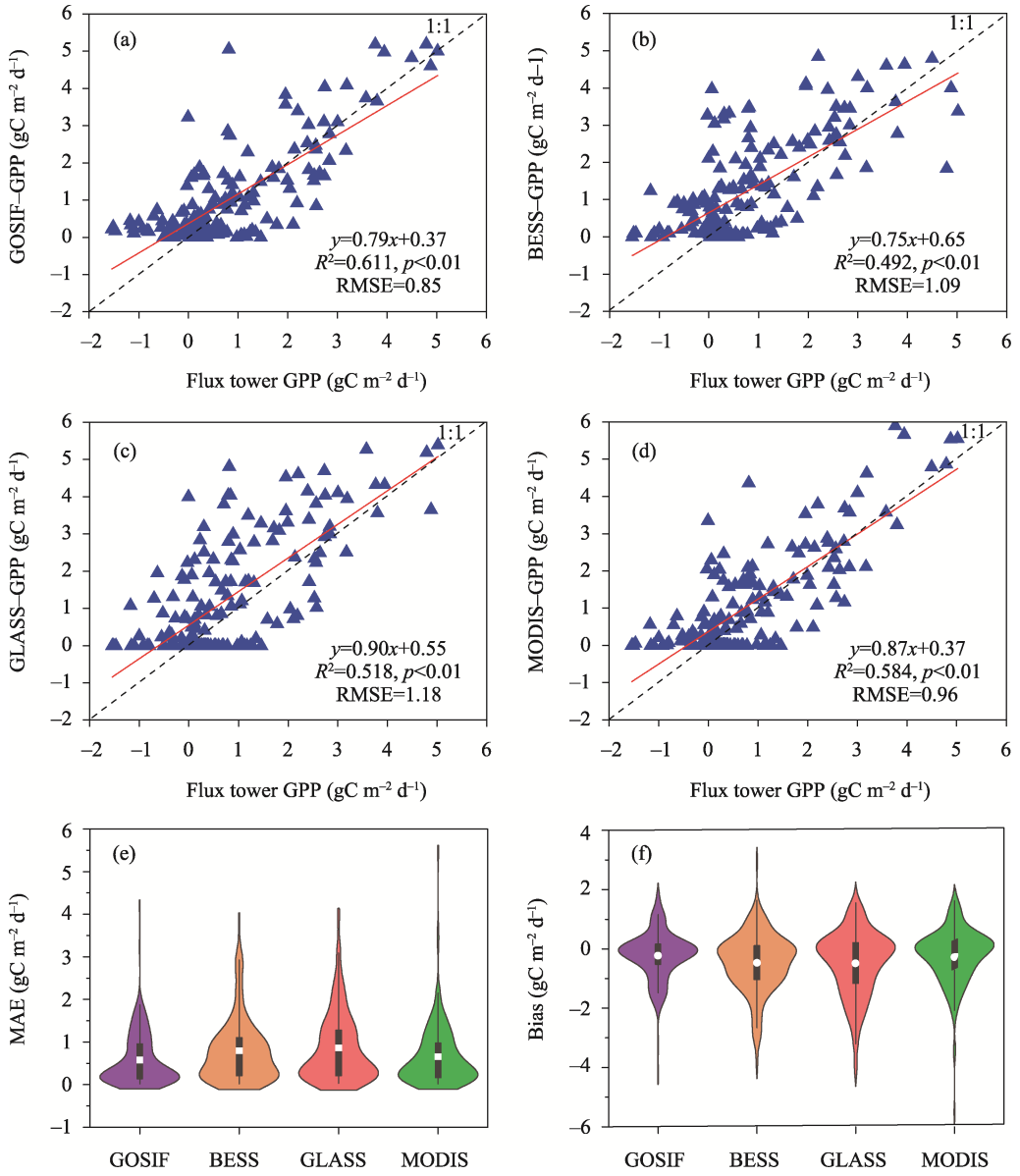

Figure 6 Correlation comparisons of the four GPP products over an 8-daily time scale from 2007 to 2010 (a. GOSIF, b. BESS, c. GLASS, d. MODIS products, e. MAE frequency, f. bias between the four gridded datasets and flux tower GPP)

desert steppe (0.54 gC m^{-2} mm^{-1}), with the lowest WUE values occurred in the western Gobi Desert ecosystem, with a value of 0.28 gC m^{-2} mm^{-1} (Figure 8c). From 2001 to 2020, the WUE in Inner Mongolia showed a non–significant decreasing trend with a rate of –0.0016 gC m^{-2} mm^{-1} a^{-1}, accounting for 55.15% of the entire region (Figures 8a and 8b). The decreasing WUE was mainly distributed in the north of Xingan, north of Chifeng, central Hulunbuir, east of Xilingol, and northwest of Alxa. In contrast, the WUE in the Ordos, Ulan Qab, Bayan Nur, Baotou, Hohhot, and eastern Alxa regions showed an increasing trend, accounting for 44.85% of Inner Mongolia.

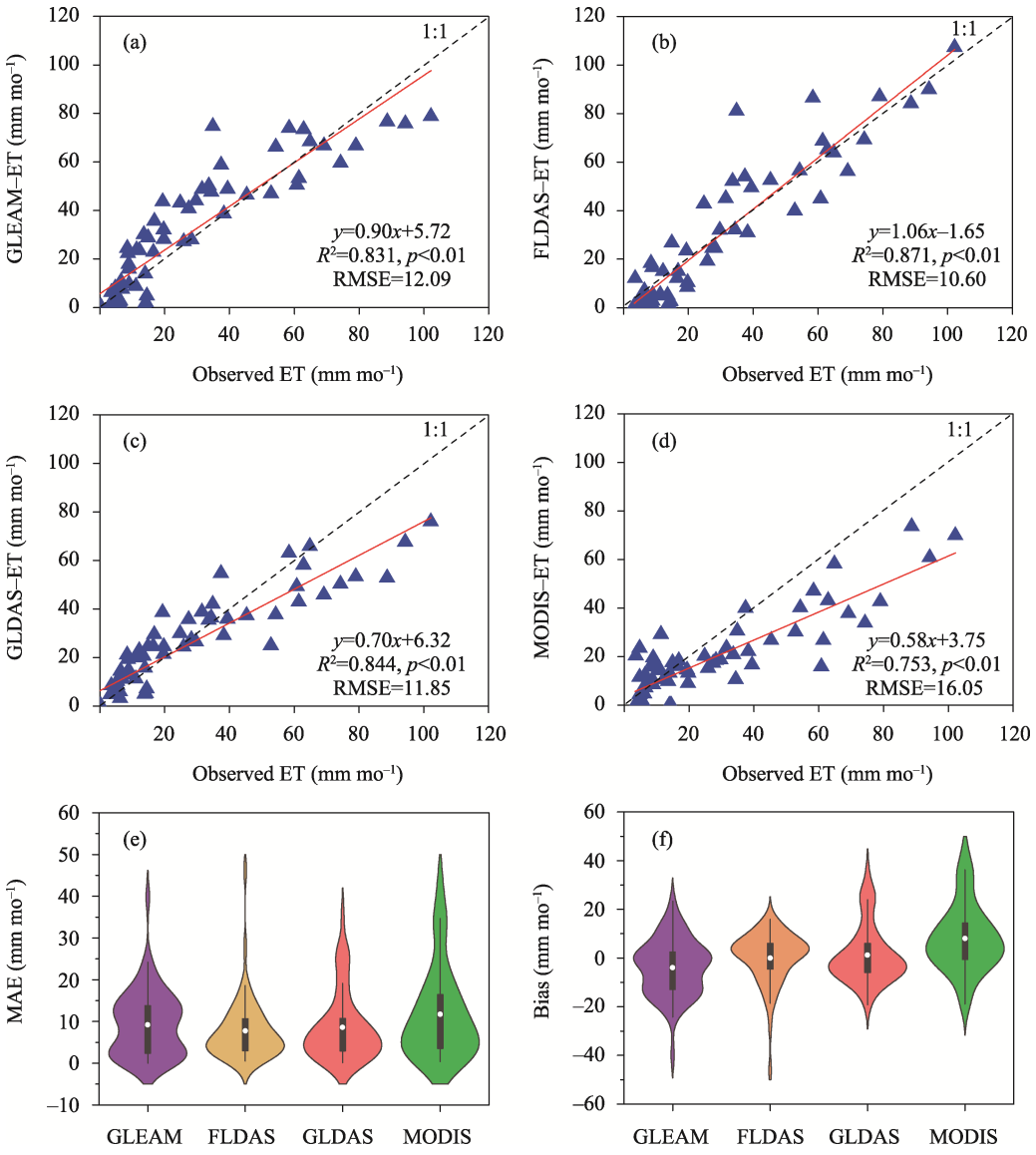

Figure 7 Correlation comparisons of the four ET products over a monthly time scale from 2004 to 2008 (a. GLEAM, b. FLDAS, c. GLDAS, d. MODIS products, e. MAE frequency, f. bias between the four gridded datasets and observed ET)

From 2001 to 2020, the VPD and wind speed of Inner Mongolia showed decreased by –0.002 m s^{-1} a^{-1} and –0.002 kPa a^{-1}, respectively. Whereas other driving factors such as soil moisture in different layers, precipitation, TWS, and temperature all showed increasing trends, which implied that characterize the warming and wetting in Inner Mongolia. Among these drivers, the interannual variations in soil moisture of four different layers were well consistent with precipitation, and there are all significantly increasing trends (Figure 9).

3.4 Relationship between the WUE and driving factors

We found that 59.44% of the WUE pixels (significant in 14.85% of pixels) were positively

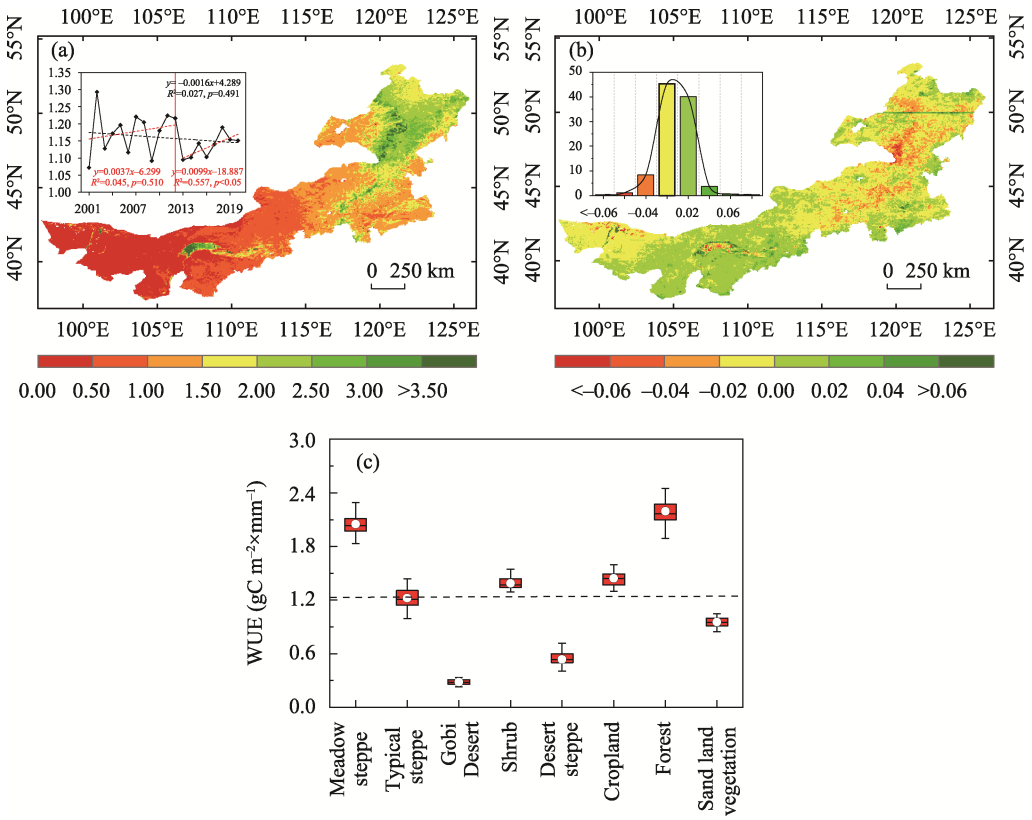

Figure 8 Distribution of annual average WUE (a), trends (b), and different vegetation types (c) of Inner Mongolia from 2001 to 2020. The black dotted line represents the average WUE value for Inner Mongolia.

correlated with precipitation, and are mainly found in central and western Inner Mongolia, this indicates that in these regions increased precipitation leads to increased WUE. Whereas WUE negatively correlated with precipitation in 40.56% of the pixels, with 14.77% of them being statistically significant. This area was mainly distributed in the northeast part of Inner Mongolia (Figure 10). A negative correlation between WUE and VPD was observed in central and western Inner Mongolia accounting for 61.89% of the pixels (significant in 17.85% of pixels), which suggests that these regional WUE values declined with intensified atmospheric drought. By contrast, a positive correlation between WUE and VPD was found mainly in the northeast part of Inner Mongolia, accounting for 38.11% of pixels (significant in 10.13% of pixels, Figure 10). In addition, the WUE was positively correlated with SM of different layers and TWS over central and western Inner Mongolia. However, the WUE was negatively correlated with TWS, SM0–10cm, SM10–40cm, SM40–100cm, and SM100–200cm over the eastern Inner Mongolia, accounting for 55.48% (14.16%), 56.41% (23.45%), 59.52% (20.70%), 59.08% (17.44%), and 55.03% (9.20%) of the pixels, respectively (Figure 10). This implied that WUE tends to decrease with increasing SM and TWS under relatively wet conditions. Additionally, 52.92% (significant in 1.79%) of wind speed and 55.53% (significant in 5.02%) of temperature pixels were negatively correlated with WUE and were mainly located in the central and western parts of Inner Mongolia, illustrating that the increase in wind speed and temperature had a clear negative effect on WUE.

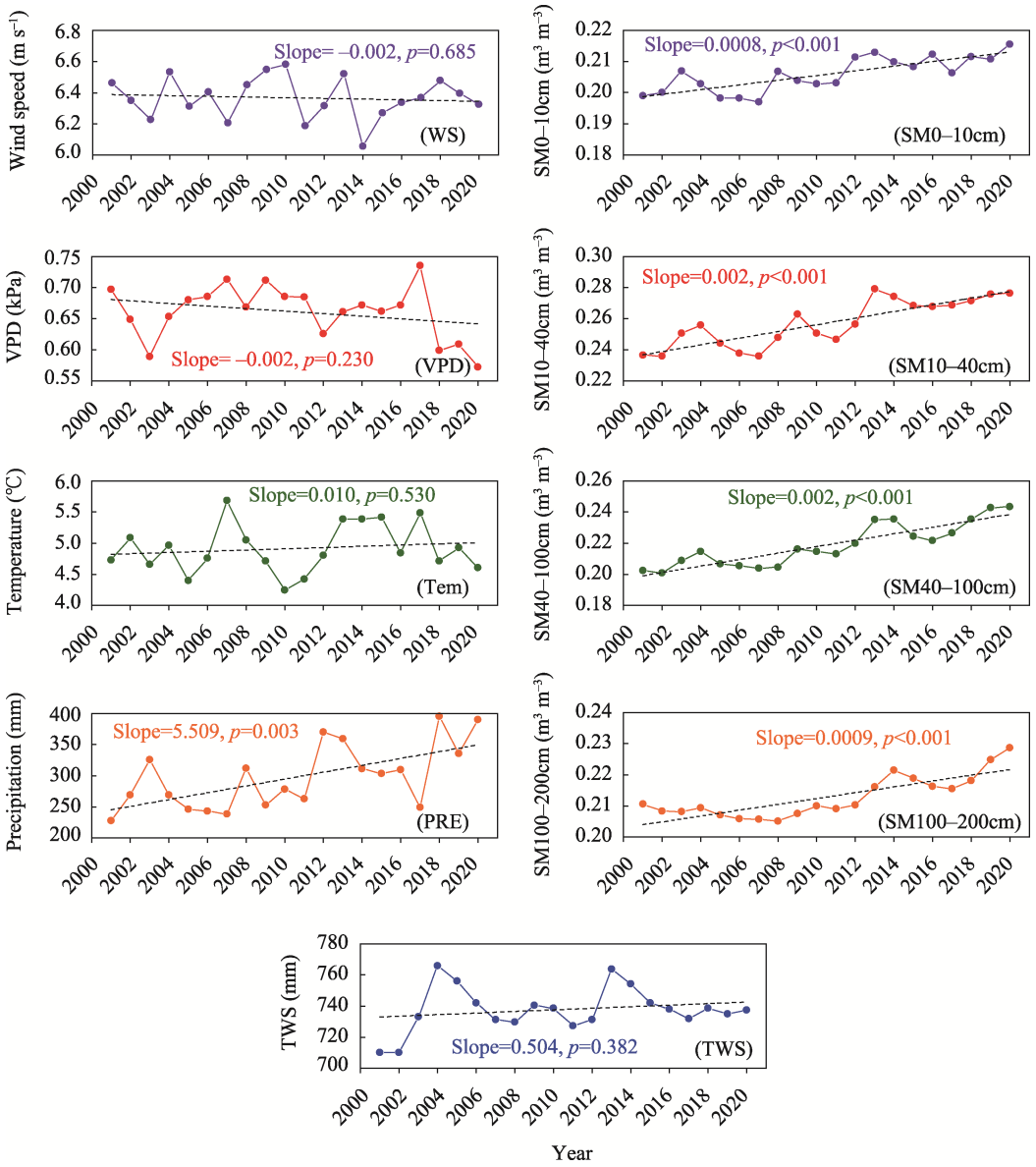

Figure 9 Long-term changes of different driving factors in Inner Mongolia from 2001 to 2020. The black dotted line represents the trend line.

The spatial pattern of the maximum correlation coefficients (R_{max}) between WUE and driving factors can reflect the sensitivity of WUE to the variability of driving factors (Figures 11 and 12). The results illustrate that WUE over Inner Mongolia is most sensitive to SM0–10cm, VPD, and precipitation, with the areas showing significant R_{max} accounting for 12.71% (negative), 11.54% (negative), and 7.02% (positive) of Inner Mongolia, respectively (Figure 12a). In humid regions, WUE is closely related to SM0–10cm, VPD, SM10–40cm, and SM40–100cm. The regional WUE is negatively correlated with SM (0–10 cm, 10–40 cm, and 40–100 cm), while positively correlated with VPD, of which the areas with significant R_{max} accounted for 41.24%, 15.81%, 9.74%, and 7.71% of the humid regions, respectively. In particular, the SM0–10cm shows a strong negative response to WUE and is weakened

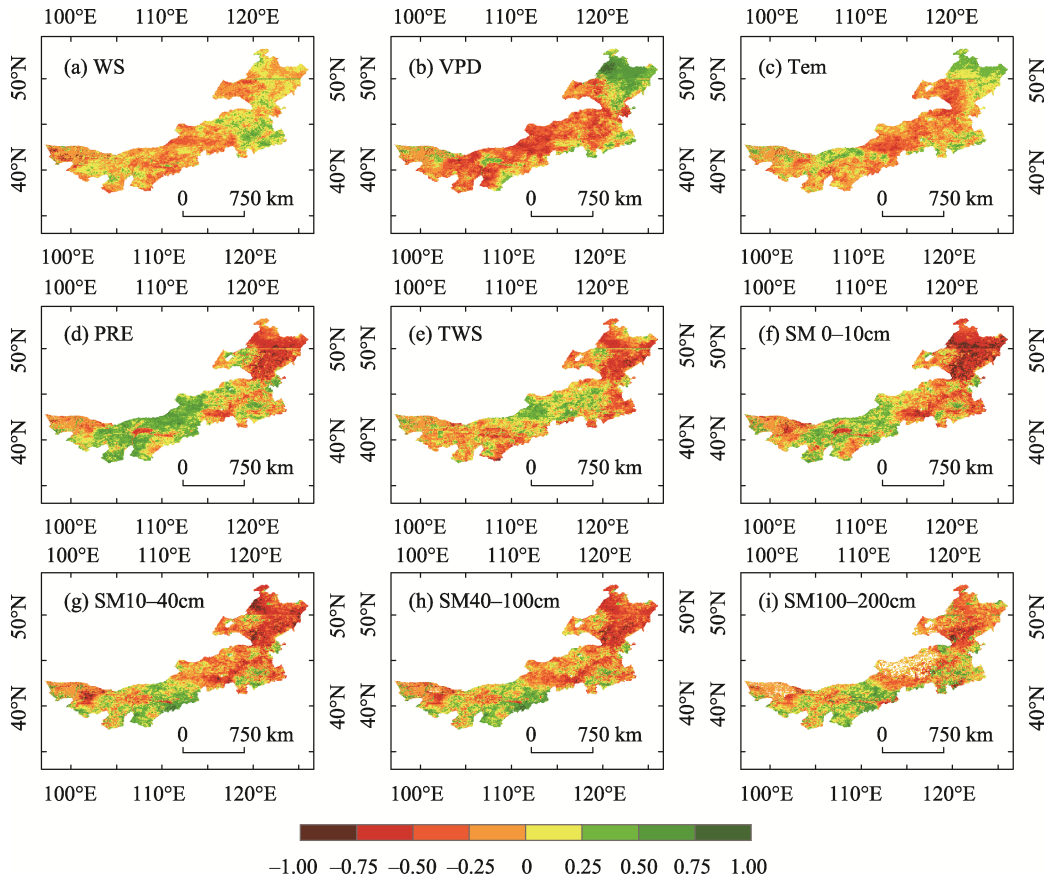

Figure 10 Spatial patterns of the correlations between WUE and driving factors in Inner Mongolia from 2001 to 2020 (a. Wind speed (WS), b. Vapor pressure deficit (VPD), c. Temperature (Tem), d. Precipitation (PRE), e. Terrestrial water storage (TWS), f. Soil moisture 0–10 cm (SM0–10cm), g. Soil moisture 10–40 cm (SM10–40cm), h. Soil moisture 40–100 cm (SM40–100cm), i. Soil moisture 100–200 cm (SM100–200cm))

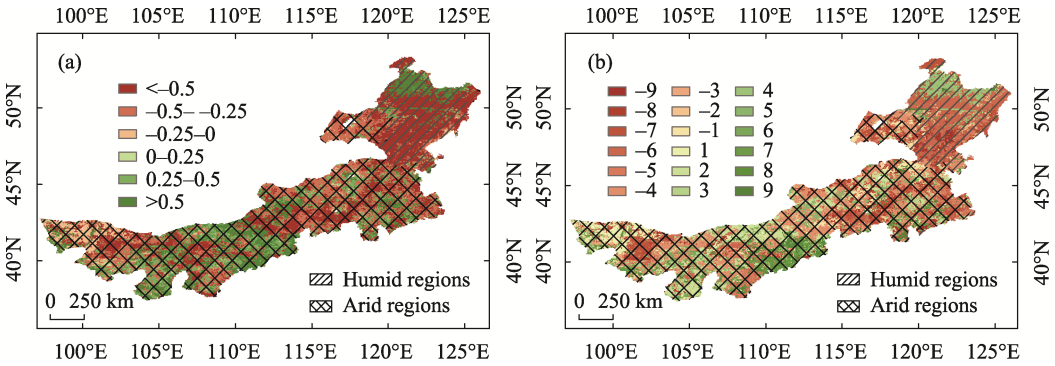

Figure 11 Spatial distributions of maximum correlation coefficients between WUE and driving factors in Inner Mongolia from 2001 to 2020 (a. Maximum correlation coefficients (R_{max}), b. Corresponding driving factors (1, 2, 3, …, 9 represent the correlations of WUE with temperature (Tem), precipitation (PRE), wind speed (WS), vapor pressure deficit (VPD), terrestrial water storage (TWS), soil moisture 0–10 cm (SM0–10cm), soil moisture 10–40 cm (SM10–40cm), soil moisture 40–100 cm (SM40–100cm), and soil moisture 100–200 cm (SM100–200 cm), respectively. A negative value denotes a negative maximum correlation, while a positive value indicates a positive maximum correlation in (b).)

with increasing soil depths (Figures 11 and 12b). In arid regions, the WUE is primarily sensitive to changes in VPD and precipitation more than the other factors. The WUE is negatively correlated with VPD, while positively correlated with precipitation, of which the regions with significant R_{max} accounted for 13.55% and 8.94% of arid regions, respectively (Figures 11 and 12c). This result reveals that the increase in VPD and precipitation had a negative and positive effect on vegetation WUE under arid conditions. Therefore, when atmospheric drought occurs in arid regions, it has a significant influence on local water resources and productivity.

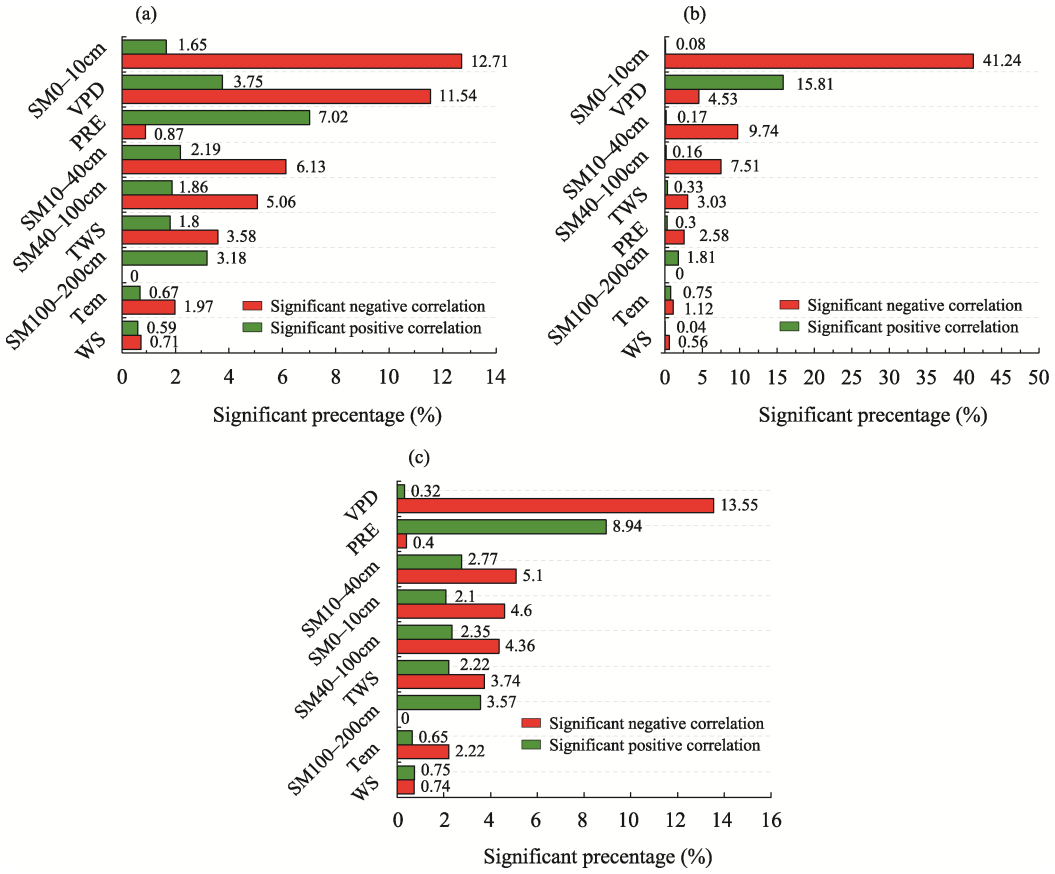

Figure 12 The significance statistics (p<0.05) for the maximum correlation coefficients between WUE and driving factors (a. Entire Inner Mongolia, b. Humid regions, c. Arid regions)

3.5 Determining the threshold of water carbon coupling for vital driving factors

To further explore the specific effects of the key dominating factors (SM0–10cm, VPD, precipitation, SM10–40cm, and SM40–100cm) regulating WUE, the coupling of WUE with the changes in these factors were analyzed. The results show that the relationships between WUE and the key driving factors are non-linear (Figure 13). The WUE along with variations in VPD exhibited an "increase-decrease-increase" model. When VPD was less than 0.36 kPa, WUE and VPD are positively correlated and WUE increased with the increasing VPD. When VPD reached approximately 0.36 kPa, the WUE was at the highest value. When the

WUE was greater than 0.36 kPa, WUE and VPD show a significant negative correlation and WUE decreased with the increasing VPD (Slope=–1.231, R^2=0.496, p<0.01), while VPD great than 1.1 kPa, the WUE once more showed an increasing trend. For precipitation, when the precipitation in Inner Mongolia was less than 426 mm, there is a significant positive correlation between WUE and precipitation (R^2=0.917, p<0.01), the WUE increased with precipitation, where for every 100 mm increase in annual precipitation, WUE increased by 0.5 gC m^{-2} mm^{-1}. When the precipitation was 426 mm, the WUE reached its peak and

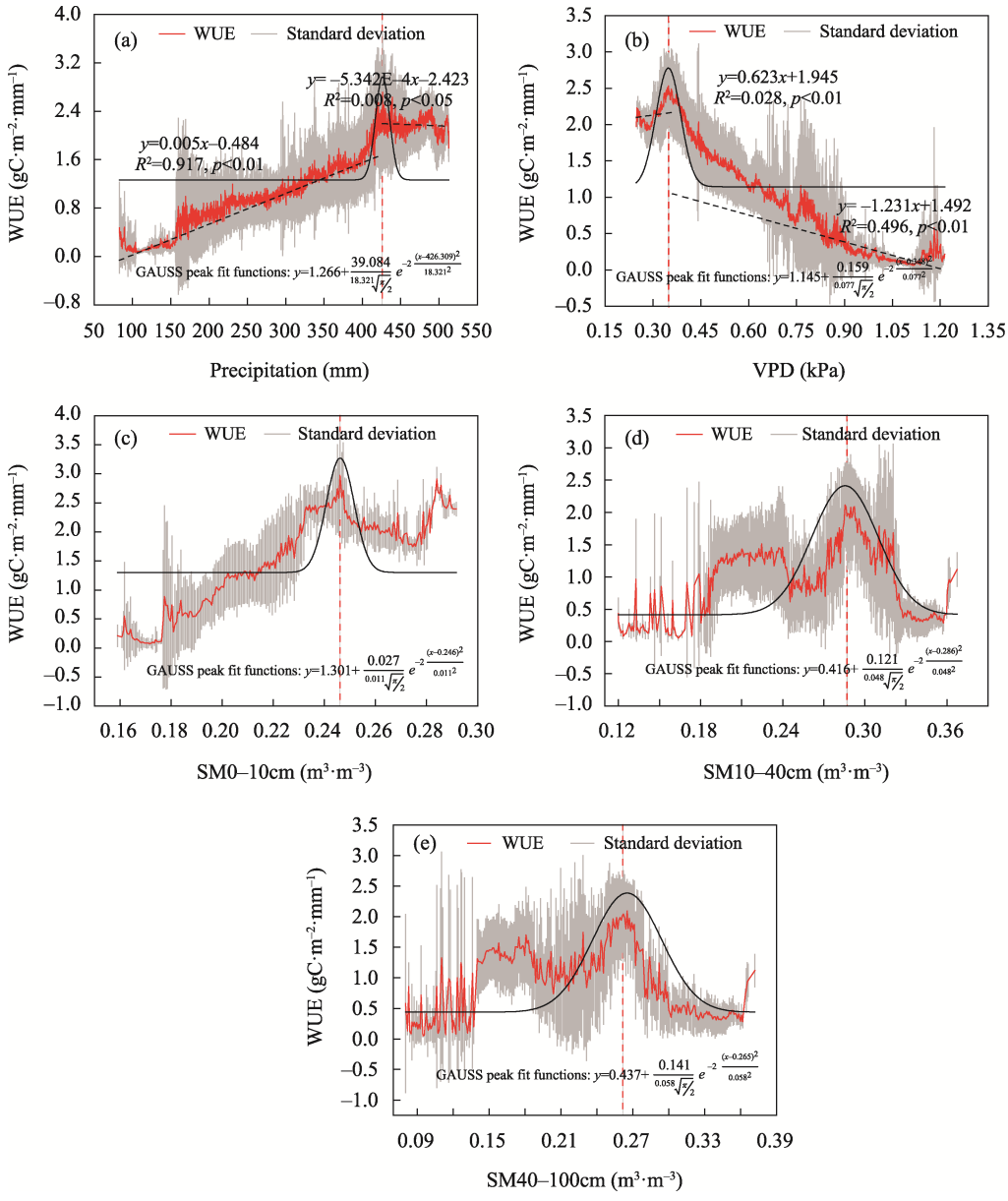

Figure 13 Relationships between WUE and the key dominant factors for Inner Mongolia (a. Precipitation (PRE), b. Vapor pressure deficit (VPD), c. Soil moisture 0–10 cm (SM0–10cm), d. Soil moisture 10–40 cm (SM10–40cm), e. Soil moisture 40–100 cm (SM40–100cm))

showed stationary behavior, but precipitation was higher than the 426 mm critical value, WUE decreased with increasing precipitation, decreased by 0.05 gC m^{-2} mm^{-1} for every 100 mm increase (R^2=0.008, p<0.05). The soil moisture was the most important factor for WUE in humid regions. When the soil moisture at a depth of 0–10 cm roughly reached 0.25 m^3 m^{-3}, the regional WUE has the highest peak value. Moreover, we observed that the SM0–10cm and precipitation exhibited relatively consistent variation patterns, this illustrates that precipitation may be made greater contributions to SM0–10cm variations than depth soil moisture (SM10–40cm and SM40–100cm). In addition, we found that depth soil moisture (SM10–40cm and SM40–100cm) variations are relatively complex and exhibited two–peak distributions. When the soil moisture at a depth of 10–40 cm and 40–100 cm was separately reached 0.28 m^3 m^{-3} and 0.26 m^3 m^{-3}, the water use efficiency of vegetation reached the maximum value, which indicates that when the soil moisture within this layer arrived at this critical value, it was beneficial to the ecosystem carbon and water exchange.

4 Discussion

4.1 Evaluation of the griddle GPP and ET datasets

The performance of the WUE depends on the accuracy of both the GPP and ET estimates. Thus, it is necessary to evaluate the reliability and accuracy before using these products (Zhang *et al*., 2015). Our results show that all gridded products have a good performance. For GPP, the four GPP products generally overestimated GPP at the flux tower sites, of which the overestimation by the GLASS product was the most prominent, with a bias of –0.48. For ET, the GLDAS, MODIS, and FLDAS products underestimated the ET at the flux tower sites, which is in agreement with previous studies for MODIS (Hu *et al*., 2015; Yang *et al*., 2021), while GLEAM overestimated the ET at the flux tower sites (Figure 7f). This underestimation or overestimation of GPP and ET may be related to relatively few flux tower observation sites in the study areas and a mismatch between the extraction range of product data and the observation range of flux towers. Our results also revealed that the GLDAS product showed greater uncertainty compared with GLEAM, MODIS, and FLDAS (Figure 5), which may be related to the differences in the employed model algorithms, parameters, and forcing data used to generate the different products. Yao *et al*. (2018) and Li *et al*. (2021a) suggested that the ET products quality is affected by the differences in model algorithm and parameterize, as well as the used forcing data. Miralles *et al*. (2016) found that the GLEAM product has relatively better performance in most vegetation types and climate regimes around the world. To further verify the effectiveness of the WUE, the WUE calculated by the GOSIF-GPP and FLDAS-ET was compared with the WUE calculated by the GOSIF-GPP and GLEAM-ET, the result shows that the spatial distribution of both WUEs has a good consistency (Figure S1).

4.2 Spatial heterogeneity and trends of WUE in Inner Mongolia

Our results show that the WUE in Inner Mongolia decreases from the northeast to the southwest, which result is consistent with Li *et al*. (2021a). The higher WUE values were found in the high coverage and within humid climatic zones. Lower WUE values were found

in the low coverage and within arid and semi-arid climate zones. The WUE of the forest biome is higher than that of meadow steppe, cropland, shrub, typical steppe, and desert steppe, which is consistent with previous research results (Bai *et al*., 2020; Zhao *et al*., 2020; Li *et al*., 2021a). This may be related to physiological characteristics, physiological structure, and living conditions of different vegetation types. Forest had a high carbon sequestration capacity (Xiao *et al*., 2013). Meanwhile, the canopy closure of the forest causes small variations in the air temperature, ground temperature, and wind speed that did not enhance the ET (Li *et al*., 2021a). For these reasons, the WUE of the forest is the highest. In addition, we also found that the regional GPP and ET all showed a significant increasing trend, increasing change rate of 5.22 gC m^{-2} yr^{-1} a^{-1} and 4.18 mm yr^{-1} a^{-1}, respectively (Figure S2). But the regional WUE showed a non–significant decreasing trend with a value of –0.0016 gC m^{-2} mm^{-1} a^{-1} (P=0.491), this decreased WUE may be caused by the synergistic effect of GPP and ET. The regional decreasing trend mainly occurs in the northwest of Alxa, eastern Xilingol, northern Xingan, northern Chifeng, and central Hulunbuir (Figures 8 and S1). This may be related to human activities (e.g., land cover changes) and shifts in species composition or abundance (Liu *et al*., 2012; Du *et al*., 2019). For example, WUE declines in the Xilingol region were caused by large-scale open-cut coal mining which results in reduce land surface cover and therefore accelerates ecosystem evapotranspiration processes (Rong *et al*., 2019). Hence, we suggest should be strengthening the prevention and protection of vegetation in these regions, to prevent the occurred vegetation degradation.

4.3 The driving factors of spatial heterogeneity of WUE in Inner Mongolia

The partial correlation analysis showed that the WUE in the arid and humid region was mostly controlled by ET than GPP (Figure S3). This result is in contrast to prior studies that WUE variability in humid regions was controlled by GPP (Yang *et al*., 2016; Liu *et al*., 2019). Our results indicate that precipitation is one of the dominant factors in controlling WUE in arid regions (Figure 10), which is consistent with previous studies (Wagle and Kakani, 2012; Bai *et al*., 2020). We found that an increase in precipitation has a positive response to WUE in arid regions. This may be caused by an increase in precipitation alleviates water stress and thus improves plant productivity, precipitation maybe was also be consumed by soil evaporation and lead to an increase in ET. However, the increased GPP was higher than ET, result to increase in WUE (Niu *et al*., 2011; Liu *et al*., 2015; Guo *et al*., 2019b). Meanwhile, Zhang *et al*. (2016) found that changes in GPP are also closely linked to changes in precipitation-induced ET. Increased precipitation in humid regions negatively contributed to WUE. Increased precipitation in humid regions can enhance canopy interception and soil evaporation (Liu *et al*., 2015). Meanwhile, increased precipitation usually being accompanied by a reduction in temperature and solar radiation, which can restrict vegetation growth and photosynthesis (Mao *et al*., 2012; Liu *et al*., 2015), which leads to an increase in ET greater than carbon uptakes to negatively effect on WUE. In addition, we found that the precipitation threshold of about 426 mm, while Liu *et al*. (2015) found a threshold value of around 500 mm in China areas.

Our results indicate that the VPD is an important determinant for controlling the dynamic changes of WUE, especially in water-limited areas (such as arid regions) where WUE is

more sensitive to VPD (that is atmospheric drought) than to soil moisture and precipitation (Figure 12c). It was found that the WUE was negatively correlated with VPD, indicates that the aggravation of atmospheric drought reduces WUE, which may be due to higher VPD leading to dramatic increases in ET, including both soil evaporation and vegetation transpiration (Liu *et al*., 2015; Wu *et al*., 2019; Li *et al*., 2021b). On the other hand, high VPD may cause some stomatal to close and inhibit photosynthetic rates (Novick *et al*., 2016; Ding *et al*., 2018; Wu *et al*., 2019; Li *et al*., 2021b; Zhao *et al*., 2021), these effects together may lead to the negative response of VPD to variations in WUE. However, in humid regions, the VPD is positively correlated with WUE, which demonstrates that higher VPD leads to increased WUE. This may be due to the fact that higher VPD can induce stomatal closure to reduce water loss through transpiration, resulting in decreased ET faster than GPP (Liu *et al*., 2019). There is another possibility that the higher VPD stimulates plant water use strategy and maintain keeps stomata openness of plants to increase GPP (Chen *et al*., 2021), these reasons may be leads to positive effects of VPD on WUE (Frank *et al*., 2015; Li *et al*., 2018c). In addition, our results found a VPD threshold of about 0.36 kPa in Inner Mongolia. However, the VPD in the southwest to northeast aridity gradient over China is a threshold of about 0.8 kPa (Bai *et al*., 2020). These differences may be caused by the intensity of drought in different regions.

Additionally, we also found that WUE variability in arid regions is regulated by the precipitation and VPD, whereas WUE in humid regions is most affected by soil moisture, in particular SM0–10cm. This difference may be related to the root characteristics and water use strategies of different vegetation types. The arid areas are mostly grassland, and herbaceous plants have relatively shallow root systems, which limits the obtaining of water from groundwater sources, and thus they are more sensitive to precipitation (Liu *et al*., 2012; Bai *et al*., 2019). In humid areas, the vegetation types are mostly forest, cropland, and shrubs, and these have deeper root systems, with their water supplied by soil moisture from the capillary fringe, root zone, and groundwater (Liu *et al*., 2012). Previous studies have shown that excessive soil water content can cause root zone hypoxia and results in the down-regulation of stomatal conductance and photosynthesis (Li *et al*., 2018c). Excessive soil water input can also promote a significant increase in abiotic water consumption (Liu *et al*., 2019), which leads to an increase in ET greater than carbon uptakes to negatively affect WUE. In short, the response of WUE to various factors was different among different vegetation types and climate zones.

4.4 Uncertainties and future studies

We validated the accuracy of four GPP and ET products using measurement data from three flux tower sites. Although all gridded products have a good performance, there are still some uncertainties in this study. First, the spatial resolutions of the multi-source remote sensing products were not exactly the same, using different resolution products could lead to uncertainties in the expected results. Second, uncertainties would arise from a mismatch between the extraction range of the product data and the observation range of flux towers. Third, there is relatively little flux tower observation data in the study area, which leads to large uncertainties in the accuracy of the evaluation products. In this study, we only discussed the

effect of both climate change and soil water content on the variability of WUE. However, the WUE of ecosystems is affected by many other factors including Leaf area index (LAI) (Huang *et al*., 2010), drought (Ma *et al*., 2019), CO_2 fertilization (Wu *et al*., 2019; Liu *et al*., 2020), stomatal conductance (Xu *et al*., 2020), and land cover change (Li *et al*., 2021a). Therefore, it is necessary to further explore other factors affecting the WUE. Our study also points out that VPD and soil moisture acts as important environmental factors for understanding carbon-water coupling in Inner Mongolia. Therefore, in the future, to furthermore consider VPD and soil moisture in predicting and simulating terrestrial ecosystem responses to future climate change.

5 Conclusions

Ecosystem WUE is a vital indicator to explore the interactions between carbon and water cycles in terrestrial ecosystems, and accurate estimates of ecosystem WUE can contribute to quantifying the carbon-water exchange of ecosystem function under climate change. The result shows that the spatial pattern of four GPP and ET products gradually decreases from the northeast to the southwest. Meanwhile, an increasing trend for all GPP and ET products over the study area except for the ET estimated from GLDAS products. Using flux tower observations data validated four GPP and ET products found that GOSIF and FLDAS have a good performance and therefore utilize them to estimate WUE. The spatially WUE showed decreasing trends accounting for 55.15% of the entire region, where distributed in the north of Xingan, north of Chifeng, central Hulunbuir, east of Xilingol, and northwest of Alxa. In addition, the results revealed that the SM0–10cm, VPD, and precipitation play an important role in regulating variations in WUE over Inner Mongolia. In arid regions, the WUE is mostly controlled by VPD and precipitation. An increase in VPD and precipitation has negative and positive effects on WUE. In humid regions, variations in WUE are closely associated with SM0–10cm, VPD, SM10–40cm, and SM40–100cm, in which SM0–10cm has the most negative influence on WUE and is weakened with soil depth. These findings improve our understanding of arid and semi-arid region WUE variability and its driving mechanisms and provide vital insight into predicting the feedback from ecosystems to climate change.

References

Bai J, Shi H, Yu Q *et al*., 2019. Satellite-observed vegetation stability in response to changes in climate and total water storage in central Asia. *The Science of the Total Environment*, 659: 862–871.

Bai Y J, Zha T S, Bourque C P-A *et al*., 2020. Variation in ecosystem water use efficiency along a southwest-to-northeast aridity gradient in China. *Ecological Indicators*, 110: 105932.

Brümmer C, Black T A, Jassal R S *et al*., 2012. How climate and vegetation type influence evapotranspiration and water use efficiency in Canadian forest, peatland and grassland ecosystems. *Agricultural and Forest Meteorology*, 153: 14–30.

Chen N, Song C C, Xu X F *et al*., 2021. Divergent impacts of atmospheric water demand on gross primary productivity in three typical ecosystems in china. *Agricultural and Forest Meteorology*, 307: 108527.

Cleverly J, Eamus D, Restrepo Coupe N *et al*., 2016. Soil moisture controls on phenology and productivity in a semi-arid critical zone. *Science of The Total Environment*, 568: 1227–1237.

Dai E F, Huang Y, Wu Z *et al*., 2016. Analysis of spatio-temporal features of a carbon source/sink and its rela-

tionship to climatic factors in the Inner Mongolia grassland ecosystem. *Journal of Geographical Sciences*, 26(3): 297–312.

Ding J Z, Yang T, Zhao Y T *et al*., 2018. Increasingly important role of atmospheric aridity on Tibetan alpine grasslands. *Geophysical Research Letters*, 45(6): 2852–2859.

Du X Z, Zhao X, Zhou T *et al*., 2019. Effects of climate factors and human activities on the ecosystem water use efficiency throughout northern China. *Remote Sensing*, 11(23): 2766.

Frank D C, Poulter B, Saurer M *et al*., 2015. Water-use efficiency and transpiration across European forests during the Anthropocene. *Nature Climate Change*, 5(6): 579–583.

Guo L M, Shan N, Zhang Y G *et al*., 2019a. Separating the effects of climate change and human activity on water use efficiency over the Beijing-Tianjin sand source region of China. *Science of The Total Environment*, 690: 584–595.

Guo L M, Sun F B, Liu W B *et al*., 2019b. Response of ecosystem water use efficiency to drought over China during 1982–2015: Spatiotemporal variability and resilience. *Forests*, 10(7): 598.

Guo D, Song X N, Hu R H *et al*., 2021. Grassland type-dependent spatiotemporal characteristics of productivity in Inner Mongolia and its response to climate factors. *Science of The Total Environment*, 775: 145644.

Hu G C, Jia L, Menenti M, 2015. Comparison of MOD16 and LSA-SAF MSG evapotranspiration products over Europe for 2011. *Remote Sensing of Environment*, 156: 510–526.

Huang L, He B, Han L *et al*., 2017. A global examination of the response of ecosystem water-use efficiency to drought based on MODIS data. *Science of the Total Environment*, 601: 1097–1107.

Huang L, Ning J, Zhu P *et al*., 2021. The conservation patterns of grassland ecosystem in response to the forage-livestock balance in North China. *Journal of Geographical Sciences*, 31(4): 518–534.

Huang M T, Piao S L, Zeng Z Z *et al*., 2016. Seasonal responses of terrestrial ecosystem water-use efficiency to climate change. *Global Change Biology*, 22(6): 2165–2177.

Huang X, Hao Y, Wang Y *et al*., 2010. Partitioning of evapotranspiration and its relation to carbon dioxide fluxes in Inner Mongolia steppe. *Journal of Arid Environments*, 74(12): 1616–1623.

Jiang C Y, Ryu Y, 2016. Multi-scale evaluation of global gross primary productivity and evapotranspiration products derived from breathing earth system simulator (BESS). *Remote Sensing of Environment*, 186: 528–547.

John R, Chen J Q, Ouyang Z T *et al*., 2013. Vegetation response to extreme climate events on the Mongolian plateau from 2000 to 2010. *Environmental Research Letters*, 8(3): 035033.

Li G C, Chen W, Li R R *et al*., 2021a. Assessing the spatiotemporal dynamics of ecosystem water use efficiency across China and the response to natural and human activities. *Ecological Indicators*, 126: 107680.

Li N, Na R S, Zhang J Q *et al*., 2018a. Vegetation dynamics and diverse responses to extreme climate events in different vegetation types of Inner Mongolia. *Atmosphere*, 9(10): 394.

Li S J, Wang G J, Sun S L *et al*., 2018b. Assessment of multi-source evapotranspiration products over China using eddy covariance observations. *Remote Sensing*, 10(11): 1692.

Li S J, Wang G J, Sun S L *et al*., 2021b. Long-term changes in evapotranspiration over China and attribution to climatic drivers during 1980–2010. *Journal of Hydrology*, 595: 126037.

Li X, Xiao J F, 2019a. A global, 0.05-degree product of solar-induced chlorophyll fluorescence derived from OCO-2, MODIS, and reanalysis data. *Remote Sensing*, 11(5): 517.

Li X, Xiao J F, 2019b. Mapping photosynthesis solely from solar-induced chlorophyll fluorescence: A global, fine-resolution dataset of gross primary production derived from OCO-2. *Remote Sensing*, 11(21): 2563.

Li Y, Shi H, Zhou L *et al*., 2018c. Disentangling climate and LAI effects on seasonal variability in water use efficiency across terrestrial ecosystems in China. *Journal of Geophysical Research*: *Biogeosciences*, 123(8): 2429–2443.

Liu N, Kala J, Liu S R *et al*., 2020. Drought can offset potential water use efficiency of forest ecosystems from rising atmospheric CO_2. *Journal of Environmental Sciences*, 90: 262–274.

Liu R, Pan L P, Jenerette G D *et al*., 2012. High efficiency in water use and carbon gain in a wet year for a desert halophyte community. *Agricultural and Forest Meteorology*, 162: 127–135.

Liu X F, Feng X M, Fu B J, 2019. Changes in global terrestrial ecosystem water use efficiency are closely related to soil moisture. *Science of The Total Environment*, 698: 134165.

Liu Y B, Xiao J F, Ju W M *et al*., 2015. Water use efficiency of China's terrestrial ecosystems and responses to drought. *Scientific Reports*, 5(1): 1–12.

Luo M, Meng F H, Sa C L *et al*., 2021. Response of vegetation phenology to soil moisture dynamics in the Mongolian Plateau. *Catena*, 206: 105505.

Ma J, Xiao X M, Zhang Y *et al*., 2018. Spatial-temporal consistency between gross primary productivity and solar-induced chlorophyll fluorescence of vegetation in China during 2007–2014. *Science of The Total Environment*, 639: 1241–1253.

Ma J Y, Jia X, Zha T S *et al*., 2019. Ecosystem water use efficiency in a young plantation in northern China and its relationship to drought. *Agricultural and Forest Meteorology*, 275: 1–10.

Mao D H, Wang Z M, Luo L *et al*., 2012. Integrating AVHRR and MODIS data to monitor NDVI changes and their relationships with climatic parameters in Northeast China. *International Journal of Applied Earth Observation and Geoinformation*, 18: 528–536.

Martens B, Miralles D G, Lievens H *et al*., 2017. GLEAM v3: Satellite-based land evaporation and root-zone soil moisture. *Geoscientific Model Development*, 10(5): 1903–1925.

McNally A, Arsenault K, Kumar S *et al*., 2017. A land data assimilation system for sub-Saharan Africa food and water security applications. *Scientific Data*, 4(1): 1–19.

Miralles D G, Holmes T R H, De Jeu R A M *et al*., 2011. Global land-surface evaporation estimated from satellite-based observations. *Hydrology and Earth System Sciences*, 15(2): 453–469.

Miralles D G, Jiménez C, Jung M *et al*., 2016. The WACMOS-ET project (Part 2): Evaluation of global terrestrial evaporation datasets. *Hydrology and Earth System Sciences*, 20(2): 823–842.

Mu Q Z, Heinsch F A, Zhao M S *et al*., 2007. Development of a global evapotranspiration algorithm based on MODIS and global meteorology data. *Remote Sensing of Environment*, 111(4): 519–536.

Mu Q Z, Zhao M S, Running S W, 2011. Improvements to a MODIS global terrestrial evapotranspiration algorithm. *Remote Sensing of Environment*, 115(8): 1781–1800.

Mu S J, Yang H F, Li J L *et al*., 2013. Spatio-temporal dynamics of vegetation coverage and its relationship with climate factors in Inner Mongolia, China. *Journal of Geographical Sciences*, 23(2): 231–246.

Niu S L, Xing X R, Zhang Z *et al*., 2011. Water-use efficiency in response to climate change: From leaf to ecosystem in a temperate steppe. *Global Change Biology*, 17(2): 1073–1082.

Novick K A, Ficklin D L, Stoy P C *et al*., 2016. The increasing importance of atmospheric demand for ecosystem water and carbon fluxes. *Nature Climate Change*, 6(11): 1023–1027.

Rodell M, Houser P R, Jambor U *et al*., 2004. The global land data assimilation system. *Bulletin of the American Meteorological Society*, 85(3): 381–394.

Rong A, Bi Q G, Dong Z H, 2019. Change of grassland vegetation and driving factors based on MODIS/NDVI in Xilingol, China. *Resources Science*, 41(7): 1374–1386. (in Chinese)

Running S W, Nemani R R, Heinsch F A *et al*., 2004. A continuous satellite-derived measure of global terrestrial primary production. *Bioscience*, 54(6): 547–560.

Ryu Y, Baldocchi D D, Kobayashi H *et al*., 2011. Integration of MODIS land and atmosphere products with a coupled-process model to estimate gross primary productivity and evapotranspiration from 1 km to global scales. *Global Biogeochemical Cycles*, 25(4): 1–24.

Song Q H, Fei X H, Zhang Y P *et al*., 2017. Water use efficiency in a primary subtropical evergreen forest in Southwest China. *Scientific Reports*, 7(1): 1–10.

Sun S B, Song Z L, Wu X C *et al*., 2018. Spatio-temporal variations in water use efficiency and its drivers in China over the last three decades. *Ecological Indicators*, 94: 292–304.

Tao J, Zhu J T, Zhang Y J *et al*., 2022. Divergent effects of climate change on cropland ecosystem water use efficiency at different elevations in southwestern China. *Journal of Geographical Sciences*, 32(8): 1601–1614.

Tao S L, Fang J Y, Zhao X *et al*., 2015. Rapid loss of lakes on the Mongolian Plateau. *Proceedings of the National*

Academy of Sciences, 112(7): 2281–2286.

Wagle P, Kakani V G, 2012. Growing season variability in evapotranspiration, ecosystem water use efficiency, and energy partitioning in switchgrass. *Ecohydrology*, 7(1): 64–72.

Wang L M, Li M Y, Wang J *et al*., 2020. An analytical reductionist framework to separate the effects of climate change and human activities on variation in water use efficiency. *Science of The Total Environment*, 727: 138306.

Wang M J, Chen Y H, Wu X C *et al*., 2018. Forest-type-dependent water use efficiency trends across the Northern Hemisphere. *Geophysical Research Letters*, 45(16): 8283–8293.

Wu X C, Li X Y, Chen Y H *et al*., 2019. Atmospheric water demand dominates daily variations in water use efficiency in alpine meadows, northeastern Tibetan Plateau. *Journal of Geophysical Research*: *Biogeosciences*, 124(7): 2174–2185.

Xiao J, Sun G, Chen J X *et al*., 2013. Carbon fluxes, evapotranspiration, and water use efficiency of terrestrial ecosystems in China. *Agricultural and Forest Meteorology*, 182: 76–90.

Xu H, Zhang Z Q, Xiao J F *et al*., 2020. Environmental and canopy stomatal control on ecosystem water use efficiency in a riparian poplar plantation. *Agricultural and Forest Meteorology*, 287: 107953.

Xu Q C, 2021. Spatiotemporal variation of water use efficiency and its influencing factors in arid and semi-arid areas of China. *Geographical Science Research*, 10(2): 126–136. (in Chinese)

Yang S S, Zhang J H, Han J Q *et al*., 2021. Evaluating global ecosystem water use efficiency response to drought based on multi-model analysis. *Science of The Total Environment*, 778: 146356.

Yang S S, Zhang J H, Zhang S *et al*., 2020. The potential of remote sensing-based models on global water-use efficiency estimation: An evaluation and intercomparison of an ecosystem model (BESS) and algorithm (MODIS) using site level and upscaled eddy covariance data. *Agricultural and Forest Meteorology*, 287: 107959.

Yang Y T, Guan H D, Batelaan O *et al*., 2016. Contrasting responses of water use efficiency to drought across global terrestrial ecosystems. *Scientific Reports*, 6(1): 1–8.

Yao Y T, Wang X H, Li Y *et al*., 2018. Spatiotemporal pattern of gross primary productivity and its covariation with climate in China over the last thirty years. *Global Change Biology*, 24(1): 184–196.

Yu S, Jiang L, Du W L *et al*., 2020. Estimation and spatio-temporal patterns of carbon emissions from grassland fires in Inner Mongolia, China. *Journal of Geographical Sciences*, 30(4): 572–587.

Yuan W P, Liu S G, Yu G R *et al*., 2010. Global estimates of evapotranspiration and gross primary production based on MODIS and global meteorology data. *Remote Sensing of Environment*, 114(7): 1416–1431.

Yuan W P, Zheng Y, Piao S L *et al*., 2019. Increased atmospheric vapor pressure deficit reduces global vegetation growth. *Science Advances*, 5(8): eaax1396.

Zhang H Y, Zhan C S, Xia J *et al*., 2022. The role of groundwater in the spatio-temporal variations of vegetation water use efficiency in the Ordos Plateau, China. *Journal of Hydrology*, 605: 127332.

Zhang L, Tian J, He H L *et al*., 2015. Evaluation of water use efficiency derived from MODIS products against eddy variance measurements in China. *Remote Sensing*, 7(9): 11183–11201.

Zhang Y, Xiao X M, Guanter L *et al*., 2016. Precipitation and carbon-water coupling jointly control the interannual variability of global land gross primary production. *Scientific Reports*, 6(1): 1–9.

Zhao J X, Feng H Z, Xu T R *et al*., 2021. Physiological and environmental control on ecosystem water use efficiency in response to drought across the northern hemisphere. *Science of the Total Environment*, 758: 143599.

Zhao J X, Xu T R, Xiao J F *et al*., 2020. Responses of water use efficiency to drought in southwest China. *Remote Sensing*, 12(1): 199.

Zhu X J, Yu G R, Wang Q F *et al*., 2015. Spatial variability of water use efficiency in China's terrestrial ecosystems. *Global Planet Change*, 129: 37–44.

Zou J, Ding J L, Welp M *et al*., 2020. Assessing the response of ecosystem water use efficiency to drought during and after drought events across central Asia. *Sensors*, 20(3): 581.

Table S1 Descriptions of the flux tower sites in this study

Site ID	Nation	Site name	Vegetation types	Longitude (°E)	Latitude (°N)	Period
CN-Du2	China	Duolun grassland (D01)	Steppe	116.2836	42.0467	2006–2008
CN-Du3	China	Duolun degraded meadow	Steppe	116.2809	42.0551	2009–2010
	China	Inner Mongolia	Steppe	116.404	43.3255	2004–2005

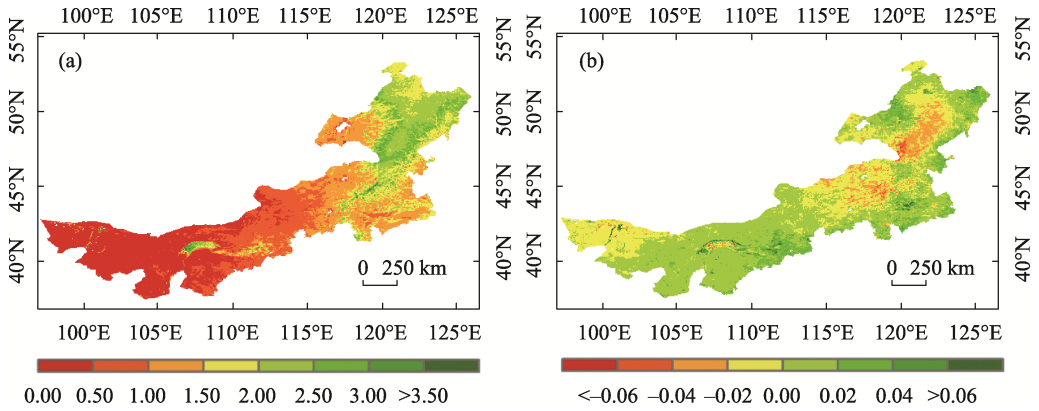

Figure S1 Based on GOSIF-GPP and GLEAM-ET obtained average WUE (a) and trends (b) over Inner Mongolia for the period 2001–2020

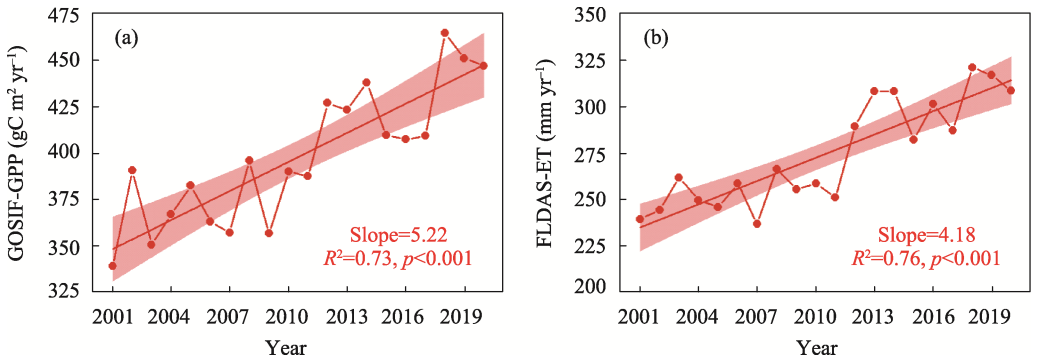

Figure S2 Interannual variations in GOSIF-GPP (a) and FLDAS-ET (b) across Inner Mongolia during 2001–2020

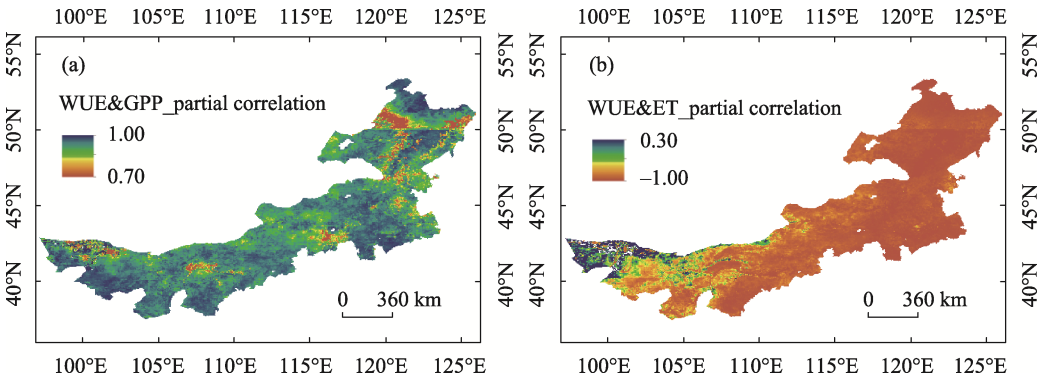

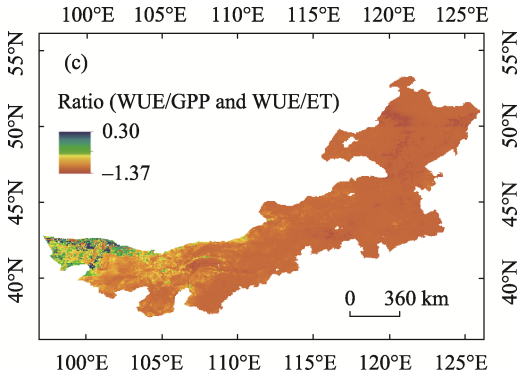

Figure S3 Spatial pattern of the partial correlation coefficient between WUE and GPP (a), WUE and ET (b), and their ratio (c) in Inner Mongolia from 2001 to 2020